Summer 2011

Dynamics and control of mechanical and biomechanical systems

Ye Liu
University of Iowa

DYNAMICS AND CONTROL OF MECHANICAL AND BIOMECHANICAL SYSTEMS

by

Ye Liu

An Abstract

Of a thesis submitted in partial fulfillment of the
requirements for the Doctor of Philosophy
degree in Mechanical Engineering
in the Graduate College of
The University of Iowa

July 2011

Thesis Supervisor: Assistant Professor Salam Rahmatalla

ABSTRACT

With the advances in mechanical and robotic systems in terms of light weights, high speeds, and precision comes a great demand for more effective vibration suppression and control schemes. This work presents a novel algorithm, called Optimal-SNC/Optimal-SNC-PID, for vibration suppression and control of mechanical and robotic systems for better accuracy. The proposed method has been tested and compared with traditional control algorithms on several multi-degree-of-freedom systems and a robotic arm under simulated random vibration signals in the vertical and horizontal directions. The proposed control scheme has the potential to be applied for high precision surgical and fabrication applications.

Transmitted vibrations can affect human performance and comfort and can be a potential risk for injuries. According to the literature, vibration transmitted to seated humans would mostly affect their lumbar and cervical spine regions. Based on the structure of the proposed Optimal-SNC control algorithm, a human head-neck model is developed in this work to resemble the head-neck biodynamic response due to fore-aft whole-body vibration. The proposed model has the potential to be used for investigating head-neck discomfort and injury. It also has the potential to be used for the development of more effective seats in whole-body applications.

Abstract Approved: _____

Thesis Supervisor

_____

Title and Department

_____

Date

DYNAMICS AND CONTROL OF MECHANICAL AND BIOMECHANICAL SYSTEMS

by

Ye Liu

A thesis submitted in partial fulfillment of the
requirements for the Doctor of Philosophy
degree in Mechanical Engineering
in the Graduate College of
The University of Iowa

July 2011

Thesis Supervisor: Assistant Professor Salam Rahmatalla

Graduate College
The University of Iowa
Iowa City, Iowa

CERTIFICATE OF APPROVAL

PH.D. THESIS

This is to certify that the Ph.D. thesis of

Ye Liu

has been approved by the Examining Committee for the thesis requirement for the Doctor of Philosophy degree in Mechanical Engineering at the July 2011 graduation.

Thesis Committee: _____
Salam Rahmatalla, Thesis Supervisor

_____
Jia Lu

_____
Shaoping Xiao

_____
David Wilder

_____
Nicole Grosland

_____
Karim Abdel-Malek

ACKNOWLEDGEMENTS

It has been a wonderful experience to study and work at the University of Iowa. First, I would like to thank my advisor, Dr. Salam Rahmatalla, for exploring with me in the interdisciplinary fields of vibration control and biomechanics. His numerous suggestions, inspiring ideas, patience, and support together have made this work possible.

I am deeply indebted to the committee members, Dr. Nicole Grosland, Dr. Jia Lu, Dr. Karim Abdel-Malek, Dr. David Wilder, and Dr. Shaoping Xiao for their constructive ideas and valuable suggestions.

I would especially like to thank Mr. Jonathan DeShaw and Mr. John Meusch for their hard work on setting-up experimental instruments and collecting experimental data.

I also would like to thank my friends in The University of Iowa, Dr. Yujiang Xiang, Dr. Liu Du, Dr. Jing Qian, Dr. Xuefeng Zhao, Dr. Youbing Yin, Mr. Jun Yang, Mr. Liang Zhao, Ms. Yang Wang, Ms. Xinhui Zhang, Ms. Shouhua Hu, Mr. Chao Zheng, and Mr. Weifei Hu for their friendship and helpful discussions.

Finally, I would like to thank my wife, Li Liu, for encouraging and supporting me to pursue what I want to do and my parents and my sister for their understanding and support.

ABSTRACT

With the advances in mechanical and robotic systems in terms of light weights, high speeds, and precision comes a great demand for more effective vibration suppression and control schemes. This work presents a novel algorithm, called Optimal-SNC/Optimal-SNC-PID, for vibration suppression and control of mechanical and robotic systems for better accuracy. The proposed method has been tested and compared with traditional control algorithms on several multi-degree-of-freedom systems and a robotic arm under simulated random vibration signals in the vertical and horizontal directions. The proposed control scheme has the potential to be applied for high precision surgical and fabrication applications.

Transmitted vibrations can affect human performance and comfort and can be a potential risk for injuries. According to the literature, vibration transmitted to seated humans would mostly affect their lumbar and cervical spine regions. Based on the structure of the proposed Optimal-SNC control algorithm, a human head-neck model is developed in this work to resemble the head-neck biodynamic response due to fore-aft whole-body vibration. The proposed model has the potential to be used for investigating head-neck discomfort and injury. It also has the potential to be used for the development of more effective seats in whole-body applications.

TABLE OF CONTENTS

LIST OF TABLES

Table

LIST OF FIGURES

Figure

PREFACE

This thesis is organized to cover two main themes. The first theme, covered by the first three chapters, is related to the development of accurate control algorithms that can be applied to vibration suppression and control of high precision fabrication and surgical mechanical systems due to ground vibration. The second theme, covered by Chapter 4, is to use the control algorithms developed in the first theme and apply it to the development of active biomechanical systems.

Chapter 1 gives an introduction to the current state-of-the-art in the vibration suppression systems and points to the current demands in this field. The chapter ends with the motivation and objectives of the thesis.

Chapter 2 introduces current practice in the control algorithms and presents several state-of-the-art control schemes. The chapter then introduces the proposed Optimal-SNC/Optimal-SNC-PID control algorithm in Section 2.5.

In Chapter 3, the proposed control algorithm of Chapter 2 is applied to many mechanical systems and a non-linear robotic arm. The effectiveness of the proposed control algorithm is verified with vibration files of different magnitudes and frequency contents. The proposed control algorithm is also compared with the state-of-the-art control algorithms.

The final chapter, Chapter 4, presents the development of active head-neck models that can be used to investigate human discomfort and injury risk under fore-aft whole-body vibration (WBV). It would also be used a guide to help seat designers

develop more effective seats in the fore-aft vibration.

CHAPTER 1
INTRODUCTION

Repeated motion due to ground vibration of rigid and deformable systems can cause a constellation of problems to the system and their occupants. Depending on its magnitude, vibration can cause significant amount of damage to the systems, such as those encountered during seismic activates, or can affect performance and cause long-term problems such as fatigue-type failures and possibly chronic health problems. For example, vehicle vibration and shocks due to bumpy roads may result in a considerable discomfort to the occupants, and floor vibration in high-tech labs and surgery rooms can generate signals that may interfere with the equipment and influence the accuracy of highly precision systems. Therefore, suppressing or controlling vibration caused by a ground/base motion becomes a vital economical and health issues.

Vibration suppression systems (VSS) are devices used to reduce the severity of the transmitted ground motion to the system based on energy dissipation and control schemes. The effectiveness of VSS is normally measured in achieving low vibration amplification around resonance areas. Depending on the severity and complexity of the system, VSS can be passive, active, semi-active, or hybrid systems. Different types of VSS have been proposed in the literatures [1, 2, 3, 4] with the objective of minimizing the vibration transmitted to the systems. Usually springs and dampers are considered the main energy-dissipating components in VSS.

In passive VSS, vibration energy is gradually converted to heat or sound [5] without the need for an external source of power. As a result, the displacement of the

system is gradually diminished. Due to their low cost, passive dampers are widely used in many applications. One well-known application of passive VSS is in vehicle suspension systems where a fluid medium, such as air or liquid, is used to produce frictional resistance that converts ground vibration energy into heat. Elastomeric based isolators such as rubber are another example of passive VSS where energy is dissipated due to the deformation of the rubber. Different types of rubber with different configurations are now wildly used in suppressing ground vibration in buildings and equipments.

The key problem in passive VSS is that they can perform effectively only in a certain range of frequencies; they perform poorly outside this frequency interval. For example, a high damping coefficient damper suppresses more system displacements than a low damping coefficient damper at low frequencies, while a high damping coefficient damper suppresses fewer system displacements than the low damping coefficient damper at high frequencies [6, 4]. Therefore, no matter which damping coefficients are selected, the system displacement cannot be suppressed well in the whole frequency domain.

Semi-active VSS are passive devices in which properties such as the stiffness and damping of the device can be altered in real time with a low power input. Semi-active VSS can only change the damping coefficient of the absorber; they add no energy to the system. Semi-active VSS are limited in their intervention—for example, the force of the semi-active VSS can never have a different direction that differs from that of that of the current speed of the suspension system. Examples of semi-active

VSS are the electrorheological (ER) dampers and magnetorheological (MR) dampers. Electrorheological dampers use the ER effect in electrorheological liquids [7]. An ER fluid can change its rheological properties, most notably its effective viscosity, by changing the electric field in the liquid. Magnetorheological dampers use MR liquids that are the magnetic analogs of ER liquids [8]. Magnetorheological liquids change their viscosity due to the change of the magnetic field in the liquids.

Active VSS uses separate actuators, such as voice-coil electromagnetic and piezoelectric actuators [9], to exert an independent force on the system to mitigate the transmitted vibration. For example, in hydraulic servomechanisms, the hydraulic pressure to the servos is supplied by a hydraulic pump with sensors continually monitoring the system vibration level and constantly supplying the computer with new data. Active VSS have shown to be very effective and have become standard tools in many high-tech fields such as precision system and robotic applications. The main advantages of the active or semi active VSS are low weight and low volume, adaptability even with nonlinear behavior, and the fact taht they work on large frequency bandwidth.

The effect of vibration exposure on systems' occupants may results in discomfort, health risk, and poor performance which are major concerns in many occupations with moving environments such as farming and construction machinery [10, 11, 12, 13, 14, 15]. Reduction in the latter problems may be achieved by reducing the magnitude of the energy transferred to the body or by changing the characteristics of the motion such that the energy transfers at frequencies that are less harmful to the body.

While experimentations may provide significant insight into human biodynamic during vibration [10, 12, 14], computer human models may present less expensive tools with a potential for evaluations that may go beyond the experimentation's allowable ethical limits and would help in the development of more effective suspension systems. Still, due to the complexity of the motion in WBV [16, 17], the nonlinearity, and the involuntary muscle activation of the human body [15, 18, 19], advances in predictive computer human modeling become a challenging issue.

1.1 Motivation

While passive and semi-active VSS have a wide range of applications, active VSS have the advantage of dealing with extreme and unexpected situations because they have the capability to apply external forces to mitigate the movement of the system with relatively high precisions. This type of situation could be hard to deal with using passive or semi-active VSS. Therefore, development of more accurate and effective active VSS with robust control algorithms is an essential topic in many fields.

While current active control algorithms such as proportional-integral-derivative (PID), fuzzy logic, linear quadratic regulator (LQR) [20, 21, 22], etc., have shown considerable success in the area of structures and robotics applications, there is still a lot of room for improvement. Additionally, there are many effective algorithms in other fields that are worth investigating and implementing in the field of structure and robotic control. For example, control algorithms in chemical, electrical, and biological [23, 24, 25] fields have shown very effective results within their applications

in these fields, but researchers have shown little attention to these applications.

A companion area that can benefit from the advancement in control theory is the area of human biodynamic during whole-body vibration (WBV), such as that encountered in construction and agricultural machinery [10, 11, 12, 13]. Studies have shown that prolonged exposure to vibration can cause problems in the lower back and the cervical spine areas of the human [10, 11, 12, 13]. Modeling human response to WBV has been an active area of research for many decades [26, 27, 28]. However, the complexity of the human anatomy, the nonlinearity of human response, and the active involuntary response of human muscles have make the modeling process very demanding for new ideas and algorithms; for example, one powerful forward dynamic modeling method to study muscle coordination is through control theory [29].

1.2 Objective

The objective of this work falls into two parts:

1. To develop an active control algorithm and then test its effectiveness by applying it to the control and vibration suppression of mechanical and robotic systems for high-precision applications.

2. To use the knowledge gained from the control algorithm of the first objective of this work to develop a data-based active muscle model and apply that to the development of a predictive multi-link head-neck human model that simulates human response to fore-aft WBV.

CHAPTER 2
CONTROL ALGORITHMS

Control algorithms that are currently implemented in real-time applications can be classified into two classes: open-loop and closed-loop (feedback) algorithms.

A flow chart of a fundamental open-loop control algorithm is shown in Figure 2.1. According to the reference output, the controller calculates the control parameters, uses them to produce the input, and then applies the input to the system. The open-loop control system doesn't recognize whether or not the system output reaches the reference output, so the control result is not precise. For example, a conventional dryer is an open-loop system. The user puts wet clothes in the dryer and chooses a certain procedure to run the dryer. The dryer runs according to the preset procedure regardless of how wet the clothes are. In this case, the dryer cannot change the running time according to the current wet status of the clothes. Therefore, open-loop controllers are only applied in simple and low-cost systems.

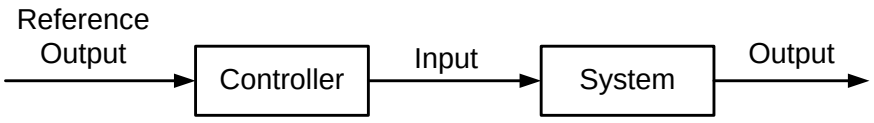

Figure 2.1: A open-loop control system

In contrast, a closed-loop controller uses measured system output to adjust

the control parameters in the process. A basic closed-loop control system is shown in Figure 2.2. The reference output is the desired value that the system output should reach. The reference output can be a number or a curve relative to the time. The system output is measured by sensors that send feedback to the controller. The measured system output is compared with the reference output, and the difference between the actual and desired value is the error. According to the error, the controller will adjust the control parameters to generate an appropriate input in order to minimize the output error. Since the controller knows the system output, the controller can suppress unknown disturbances in the system. When the error exists, the controller continues to adjust the input to reduce the error within the allowable capacity of the controller.

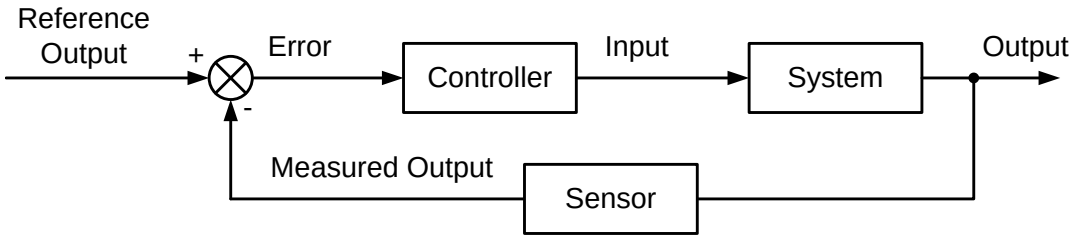

Figure 2.2: A closed-loop control system

Closed-loop controllers also have another advantage, in which an original unstable system may become stable when a closed-loop controller is applied to the system. Time lag in the control process is the main disadvantages of closed-loop

controllers. The deviation of the control input is not known until the input is applied in the system and the corresponding system output is measured.

In the following section, we present prominent active control algorithms that are widely used in mechanical and structural systems suppression.

2.1 Proportional-integral-derivative Controller

The proportional-integral-derivative (PID) controller is considered the most common control algorithm in the world. The PID Controller was developed in the early 1900s. One of the earliest PID-tpye controllers was developed by Elmer Sperry in 1911 and was used for automatic ship steering [30]. In 1922, Nicolas Minorsky first published theoretical analysis of a PID controller [31]. Even today, more than half of the industrial controllers in use are PID controllers or modified PID controllers [32].

The standard PID algorithm is described by the following equation and is shown in Figure 2.3,

$$u(t) = K_p \left(e(t) + \frac{1}{T_i} \int_0^t e(\tau) d\tau + T_d \frac{de(t)}{dt} \right) \tag{2.1}$$

where $e(t) = r(t) - y(t)$ is the system output error, $y(t)$ is the system output, and $r(t)$ is the reference output.

The PID control signal has three terms: the P-term, which is proportional to the error $e(t)$; the I-term, which is proportional to the integral of $e(t)$; and the D-term, which is proportional to the derivative of $e(t)$. Additionally, there are three control parameters that need to be tuned in the applications: proportional gain K_p, integral time T_i, and derivative time T_d. The P-term decreases the system steady-state error.

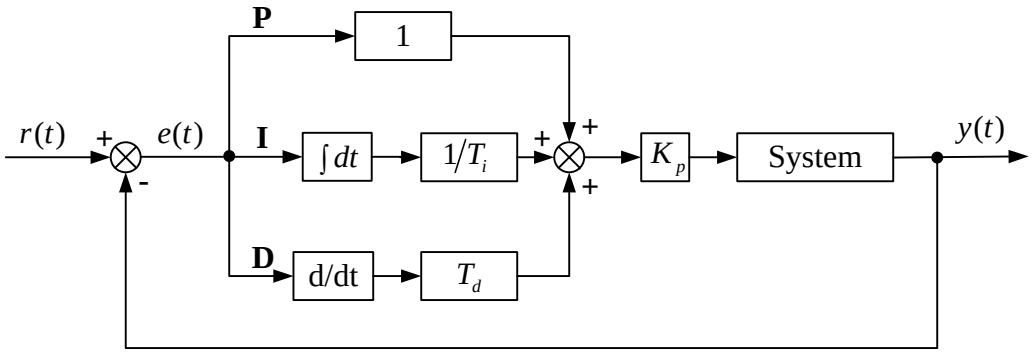

Figure 2.3: PID controller

The choice of K_p is critical because a large K_p could cause the system to oscillate and become unstable. The I-term eliminates the system-steady state error. The selection of a large T_i will cause the system to reach the reference output $r(t)$ too slowly. The D-term increases the system stability and improves the system dynamic performance; a large T_d causes the system to oscillate. The three terms, P-term, I-term, and D-term can be used in the difference combinations, such as a PD controller or a PI controller.

The PID controller is often used as the difference equation 2.2 in the discrete control process.

$$u(n+1) = u(n) + K_p\left(1 + \frac{T}{T_i} + \frac{T_d}{T}\right)e(n) - K_p\left(1 + \frac{2T_d}{T}\right)e(n-1) + \frac{K_pT_d}{T}e(n-2) \tag{2.2}$$

where n is the number of the current time step, $n-1$ is the last step, $n-2$ is the second last step, and $n+1$ is the next step. T is the sample time.

The PID controller doesn't rely on the mathematical model of the system. This means that even when the system model is not known, the PID controller can still be applied to control the system. Other control algorithms, such as optimal control algorithms, cannot be used in this case. This is one reason for the wide usage of PID controllers in many applications.

2.2 Linear Quadratic Regulator

A linear system is described by the following state-space equation:

$$\dot{\mathbf{x}} = \mathbf{A}\mathbf{x} + \mathbf{B}\mathbf{u} \tag{2.3}$$

$$\mathbf{y} = \mathbf{C}\mathbf{x} \tag{2.4}$$

with $\mathbf{x}(0) = \mathbf{x}_0$. $\mathbf{A}$ is an $n \times n$ constant matrix, $\mathbf{B}$ is an $n \times m$ constant matrix, $\mathbf{C}$ is a $k \times n$ constant matrix, $\mathbf{x}$ is an $n \times 1$ vector representing the system state, $\mathbf{y}$ is a $k \times 1$ vector representing the system output, and $\mathbf{u}$ is an $m \times 1$ vector representing the system input.

The linear quadratic regulator (LQR) is a fundamental optimal control algorithm that was proposed by Kalman in 1960 [33, 34]. The LQR algorithm determines the feedback gain matrix $\mathbf{K}$ of the optimal control vector $\mathbf{u}$ where $\mathbf{K}$ is an $m \times n$ constant matrix,

$$\mathbf{u} = -\mathbf{K}\mathbf{x} \tag{2.5}$$

to minimize the following quadratic cost function:

$$J = \int_0^\infty (\mathbf{y}^T\mathbf{Q}\mathbf{y} + \mathbf{u}^T\mathbf{R}\mathbf{u})dt \tag{2.6}$$

where $\mathbf{Q}$ is the state weight matrix and $\mathbf{R}$ is the input weight matrix. Both $\mathbf{Q}$ and $\mathbf{R}$ are positive-definite, real, and symmetric constant matrices. $\mathbf{Q}$ and $\mathbf{R}$ are control parameters and are selected to provide suitable performance to the system. The superscript T in Equation 2.6 denotes the transpose of a matrix.

Substituting Equation 2.4 into the cost function of Equation 2.6 results in a new cost function in terms of the state and the control:

$$J = \int_0^\infty (\mathbf{x}^T \mathbf{C}^T \mathbf{Q} \mathbf{C} \mathbf{x} + \mathbf{u}^T \mathbf{R} \mathbf{u}) dt \tag{2.7}$$

Equation 2.7 can be written as following:

$$J = \int_0^\infty (\mathbf{x}^T \mathbf{Q}^* \mathbf{x} + \mathbf{u}^T \mathbf{R} \mathbf{u}) dt \tag{2.8}$$

where $\mathbf{Q}^* = \mathbf{C}^T \mathbf{Q} \mathbf{C}$. The LQR algorithm usually uses Equation 2.8 as the cost function.

$\mathbf{K}$ in Equation 2.5 is given by

$$\mathbf{K} = \mathbf{R}^{-1} \mathbf{B}^T \mathbf{P} \tag{2.9}$$

The matrix $\mathbf{P}$ is solved from the following equation:

$$\mathbf{A}^T \mathbf{P} + \mathbf{P} \mathbf{A} - \mathbf{P} \mathbf{B} \mathbf{R}^{-1} \mathbf{B}^T \mathbf{P} + \mathbf{Q} = 0 \tag{2.10}$$

Equation 2.10 is the called *Algebraic Riccati Equation*.

The flow chart for the LQR control algorithm is demonstrated in Figure 2.4.

The LQR algorithm has several limitations:

1. The entire system state must be measured. Otherwise, $\mathbf{u}$ cannot be obtained.

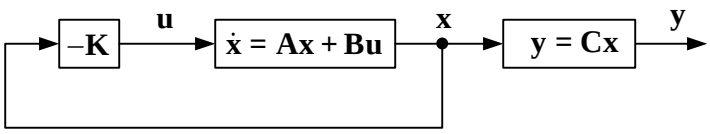

Figure 2.4: LQR system

2. The mathematical model of the system should be known accurately. If the system model is inaccurate, then there will be some errors in matrices **A** and **B**. As a result, **P** and **K** will inherent errors from Equation 2.10 and Equation 2.9, respectively. This will generate error in the control input **u**. Thus, the system output **y** will not be the desired output.

2.3 Linear Quadratic Gaussian Control

A major limitation of the LQR control algorithm of Section 2.2 is that it is a *full* state feedback controller and therefore it considers unsuitable for systems with many variables. Additionally, more measured variables means more noise involved in the system. The linear quadratic Gaussian (LQG) controller, also known as H_2 controller, was developed to overcome these problems.

Instead of measuring the entire state, the LQG controller uses a Kalman filter to estimate the system state with the control input and the system output. Therefore, the LQG is a combination of an LQR controller and a Kalman filter. The LQG controller also considers the inaccuracy of the system model and suppresses this noise.

The equation of motion of a linear system is

$$\dot{\mathbf{x}} = \mathbf{A}\mathbf{x} + \mathbf{B}\mathbf{u} + \mathbf{B}_w\mathbf{w} \tag{2.11}$$

$$\mathbf{y} = \mathbf{C}\mathbf{x} + \mathbf{v} \tag{2.12}$$

where matrices $\mathbf{A}$, $\mathbf{B}$, and $\mathbf{C}$ are defined in a similar way to that shown in Section 2.2. $\mathbf{B}_w$ is an $n \times m$ constant matrix; $\mathbf{y}$ and $\mathbf{u}$ are the system measured output and the control input, respectively; $\mathbf{w}$ is a random disturbance input also known as system noise; and $\mathbf{v}$ is also a random signal known as measurement noise. Both $\mathbf{w}$ and $\mathbf{v}$ have a zero-mean, independent white noise.

Constructing $\hat{\mathbf{x}}$ and $\hat{\mathbf{y}}$ using the system output $\mathbf{y}$ and the control input $\mathbf{u}$ yields

$$\dot{\hat{\mathbf{x}}} = \mathbf{A}\hat{\mathbf{x}} + \mathbf{B}\mathbf{u} + \mathbf{L}(\mathbf{y} - \hat{\mathbf{y}}) \tag{2.13}$$

$$\hat{\mathbf{y}} = \mathbf{C}\hat{\mathbf{x}} \tag{2.14}$$

where $\hat{\mathbf{x}}$ is the estimate of $\mathbf{x}$ and $\hat{\mathbf{y}}$ is the estimate of $\mathbf{y}$. When $\hat{\mathbf{x}}$ is equal to $\mathbf{x}$, $\hat{\mathbf{y}}$ is equal to $\mathbf{y}$, and the correction term $\mathbf{L}(\mathbf{y} - \hat{\mathbf{y}})$ is eliminated. However, when $\hat{\mathbf{x}}$ goes away from $\mathbf{x}$, the correction term will work and correct the error.

Substituting Equation 2.14 into the Equation 2.13 yields

$$\dot{\hat{\mathbf{x}}} = (\mathbf{A} - \mathbf{L}\mathbf{C})\hat{\mathbf{x}} + \mathbf{B}\mathbf{u} + \mathbf{L}\mathbf{y} \tag{2.15}$$

The estimation error is

$$\mathbf{e} = \mathbf{x} - \hat{\mathbf{x}} \tag{2.16}$$

The estimator gain matrix $\mathbf{L}$ is decided to minimize the asymptotic expected

value of the estimation error:

$$J_{LQG} = \lim_{t\to\infty} E[\|\mathbf{e}\|^2] \tag{2.17}$$

where E denotes expectation (mean value).

Set $\mathbf{Q}_N$ and $\mathbf{R}_N$ as the spectral densities of $\mathbf{w}$ and $\mathbf{v}$, respectively. The optimal estimator gain matrix $\mathbf{L}$ is given by

$$\mathbf{L} = \mathbf{P}\mathbf{C}^T\mathbf{R}_N^{-1} \tag{2.18}$$

$\mathbf{P}$ is solved by the following *Algebraic Riccati Equation*

$$\mathbf{A}\mathbf{P} + \mathbf{P}\mathbf{A}^T + \mathbf{B}_w\mathbf{Q}_N\mathbf{B}_w^T - \mathbf{P}\mathbf{C}^T\mathbf{R}_N^{-1}\mathbf{C}\mathbf{P} = 0 \tag{2.19}$$

When the optimal $\mathbf{L}$ is used in the Equation 2.15, the system is called the Kalman filter.

Therefore, the control input $\mathbf{u}$ is

$$\mathbf{u} = -\mathbf{K}\hat{\mathbf{x}} \tag{2.20}$$

where $\mathbf{K}$ is decided by Equation 2.9 and Equation 2.10 in the LQR controller.

The LQG control system is shown in Figure 2.5.

The LQG still has several disadvantages:

1. The system should be linear, and the system model should be completely known.

2. The noises $\mathbf{w}$ and $\mathbf{v}$ should be zero-mean white noise.

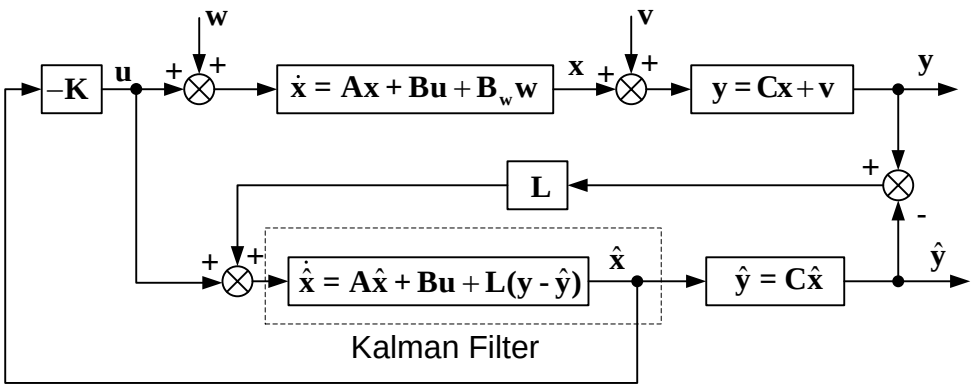

Figure 2.5: LQG control system

2.4 Single Neuron Controller

2.4.1 Single Self-adaptive Neuron Controller Mathematic Model

The single neuron controller (SNC) was introduced by Wang in 1992 [23]. A neuron is a multi-input single-output non-linear unit with self-learning and self-adaptive ability. A general single neuron is shown in Figure 2.6. The figure shows that a neuron has n inputs x_i $(i = 1, 2, \ldots, n)$, which are outside information transfer to the neuron. w_i are the weights relative to x_i and can be decided by learning rules, which will be explained in the next section. K is the gain of the neuron. $p_i(t)$ is the performance function, which is described in Equation 2.26. The system could be any single-input single-output (SISO) system, such as a single-degree-of-freedom mass spring system with an active damper. y_s is the system output, which could be any number, such as displacement, temperature, and so on. The converter will transfer the system output y_s to the neuron inputs x_i, and the operation could be any

mathematical operation, such as multiplication, derivation, integration, and so on.

The output of the neuron is shown in the following equation:

$$y = K \sum_{i=1}^{n} w_i x_i \tag{2.21}$$

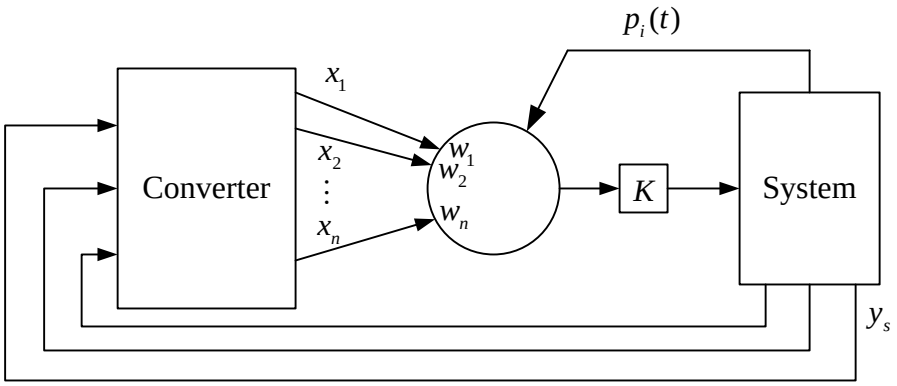

Figure 2.6: Single neuron model

2.4.2 Learning Rules

In 1949 D.O.Hebb [35] postulated that:

"When an axon of cell A is near enough to excite a cell B and repeatedly or persistently takes part in ring it, some growth process or metabolic change takes place in one or both cells such that A's efficiency, as one of the cells ring B, is increased."

That is, a synapse's strength is reinforced if neurons on the both sides of the synapse are activated synchronously and repeatedly. The *Hebb rule* is the first learning rule

of neurons and is described in the following equation:

$$w_{ij}(t+1) = w_{ij}(t) + d_{ij} \times y_j(t) \times x_i(t) \tag{2.22}$$

where x_i and y_i are the output of neurons i and j, respectively, and d_{ij} is the learning rate for the ijth weight.

The learning rule in a single self-adaptive neuron is described as

$$w_i(t+1) = (1-c)w_i(t) + d_i \times p_i(t) \tag{2.23}$$

where the learning rate d is large than 0, c is a number between 0 and 1, and $p_i(t)$ is the information signal deciding how $w_i(t)$ should change.

The self-adaptive neurons usually use two simple learning rules:

(1) The Hebb rule:

$$p_i(t) = s(t)x_i(t) \tag{2.24}$$

where $x_i(t)$ is the input of neurons, and $s(t)$ is neurons' adaptive property.

(2) The supervised learning rule:

$$p_i(t) = z(t)x_i(t) \tag{2.25}$$

where $z(t)$ is the supervised signal.

Both of the rules are used in the single self-adaptive neurons,

$$p_i(t) = z(t)s(t)x_i(t) \tag{2.26}$$

This means that a single self-adaptive neuron uses the Hebb rule and the supervised learning rule at the same time.

2.4.3 Self-adaptive Neuron Control Algorithm

If $c = 0$ in Equation 2.23, the control algorithm becomes

$$u(t) = K \sum_{i=1}^{n} w_i(t) x_i(t) \tag{2.27}$$

$$w_i(t+1) = w_i(t) + d_i \times (r(t) - y(t)) \times x_i(t) \tag{2.28}$$

where $r(t)$ is the reference output, and $y(t)$ is the system output.

In order to guarantee convergence and control stability, $w_i(t)$ are normalized.

$$u(t) = K \sum_{i=1}^{n} w_i^{'}(t) x_i(t) \tag{2.29}$$

$$w_i^{'}(t) = \frac{w_i(t)}{\sum_{i=1}^{n} |w_i(t)|} \tag{2.30}$$

$$w_i(t+1) = w_i(t) + d_i \times (r(t) - y(t)) \times x_i(t) \tag{2.31}$$

In order to use Equation 2.29 - 2.31 as a controller in a control system, n and $x_i(t)$ should be decided. There are several cases.

(1) If $r(t)$ is constant and is not zero, $n = 3$, and $x_i(t)$ are,

$$x_1(t) = r(t) \tag{2.32}$$

$$x_2(t) = r(t) - y(t) = e(t) \tag{2.33}$$

$$x_3(t) = \Delta x_2(t) = x_2(t) - x_2(t-1) = e(t) - e(t-1) \tag{2.34}$$

The control system with an adaptive neuron controller is shown in the Figure 2.7.

Figure 2.7 shows that the control signal of a signal neuron controller has three parts: feed-forward proportional control $u_1(t)$, feedback proportional control

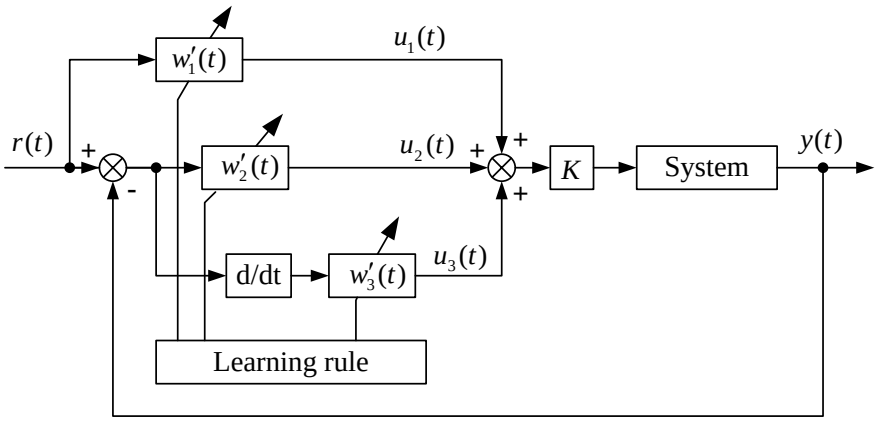

Figure 2.7: Single neuron control system

$u_2(t)$, and feedback derivative control $u_3(t)$. Therefore, a single neuron controller includes both the feed-forward control and feedback control. The feed-forward control put the reference output $r(t)$ through $w_1'(t)$ directly to the system, which increases the system's response rate but does not cause overshoot and oscillation. The feedback proportional control quickly decreases the system error. The feedback derivative control improves the system response rate and decreases overshoot. The single neuron controller integrates these three control ability, and the feed-forward control also increases the ability of overcoming external disturbance and decreases overshoot and oscillation caused by the feedback proportional control. The single neuron controller adjusts the weights according to the learning rule. When there is error in the system, the neuron uses the three control items together and rapidly decreases the system error in the process. When the error is zero, both $u_2(t)$ and $u_3(t)$ are zeros, and only the feed-forward proportional

control $u(t)$ works. Therefore, the single neuron controller does not need integral control to eliminate steady-state error in the process.

(2) If $r(t)$ changes in the process.

In order to fast track the reference output $r(t)$, a neuron input as the derivative of $r(t)$ is added, so n=4.

$$x_1(t) = r(t) \tag{2.35}$$

$$x_2(t) = \Delta r(t) = r(t) - r(t-1) \tag{2.36}$$

$$x_3(t) = r(t) - y(t) = e(t) \tag{2.37}$$

$$x_4(t) = \Delta x_3(t) = x_3(t) - x_3(t-1) = e(t) - e(t-1) \tag{2.38}$$

In this SNC controller, there are two feed-forward controls, $u_1(t)$ and $u_2(t)$, and two feedback controls, $u_3(t)$ and $u_4(t)$. The control system is shown in Figure 2.8.

(3) Combining the single neuron controller and the PID controller.

When the reference output $r(t)$ is zero, the feed-forward controller in a general SNC controller cannot be used in the process because $u_1(t)$ will be always zero. In this case, the proportional-integral-derivative controller is pulled into the single neuron controller, and the algorithm is called SNC-PID. n is still 3, and $x_i(t)$ are changed to the following equations,

$$x_1(t) = r(t) - y(t) = -y(t) = e(t) \tag{2.39}$$

$$x_2(t) = \int e(t)dt \tag{2.40}$$

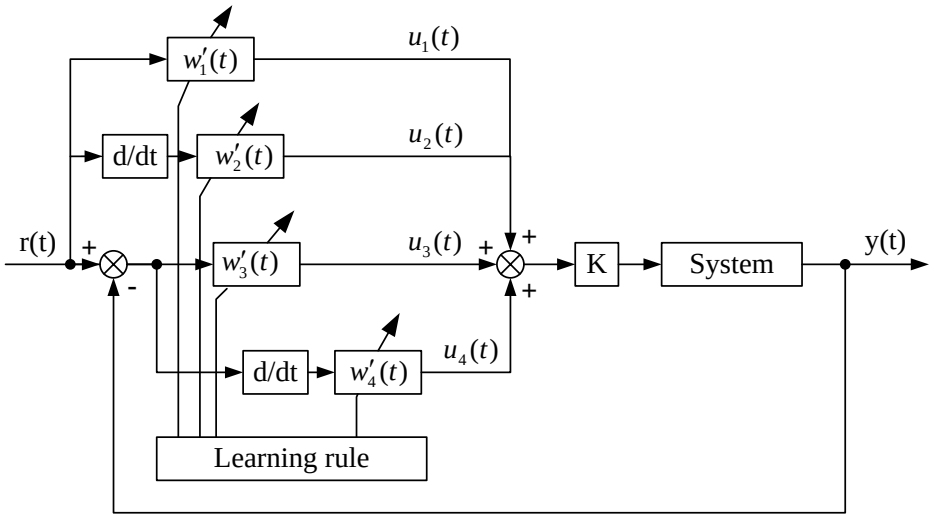

Figure 2.8: Tracking SNC control system

$$x_3(t) = \frac{de(t)}{dt} \tag{2.41}$$

Figure 2.9 shows an SNC-PID controller in the control system. Figure 2.9 shows that an SNC-PID controller has three parts: feedback proportional control $u_1(t)$, feedback integral control $u_2(t)$, and feedback derivative control $u_3(t)$, similar to a general PID controller. The difference between an SNC-PID controller and a general PID controller is that the weights $w_i(t)$ in an SNC-PID controller are adjusted according to a learning rule, but the similar coefficients in a PID controller are fixed in the process.

2.4.4 SNC Network Controllers in Multi-input Multi-output System

The SNC network control system is shown in Figure 2.10. The system is an n-inputs and n-outputs coupled system, so there is an SNC controller for each pair of

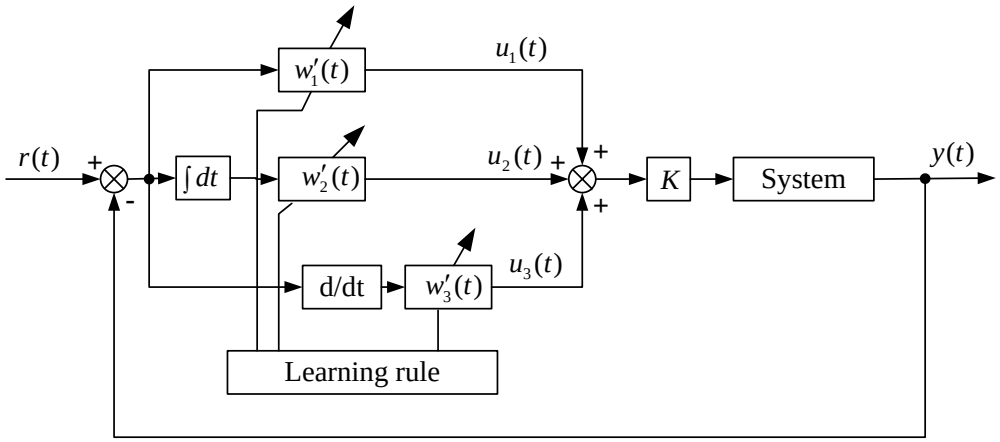

Figure 2.9: SNC-PID control system

inputs and outputs. The total number of SNC controllers is n. Each SNC controller has m inputs and produces $u_i(t)(i = 1, \ldots, n)$. The system also produces n outputs $y_i(t)(i = 1, \ldots, n)$. Here, the SNC controller can be an SNC or SNC-PID controller. The system output $y_i(t)$ and/or the reference output $r_i(t)$ are transferred to the state variables $x_{ij}(t)$ $(i = 1, \ldots, n, j = 1, \ldots, m)$ by the converter, which input to the neurons. $x_{ij}(t)$ is the jth state variable of the ith neurons, and $w_{ij}(t)$ is the weight with respect to $x_{ij}(t)$. $p_i(t)$ and $K_i(t)$ are the performance function and the gain of the ith neuron, respectively.

A multi-variable SNC network Controllers' algorithm is shown in the following equations:

$$u_i(t) = K_i \sum_{j=1}^{m} w'_{ij}(t) x_{ij}(t) \tag{2.42}$$

$$w_{ij}^{'} = \frac{w_{ij}(t)}{\sum_{j=1}^{m} |w_{ij}(t)|} \tag{2.43}$$

$$w_{ij}(t+1) = w_{ij}(t) + d_{ij}(r_i(t) - y_i(t))x_{ij}(t) \tag{2.44}$$

where $i = 1, \ldots, n, j = 1, \ldots, m$.

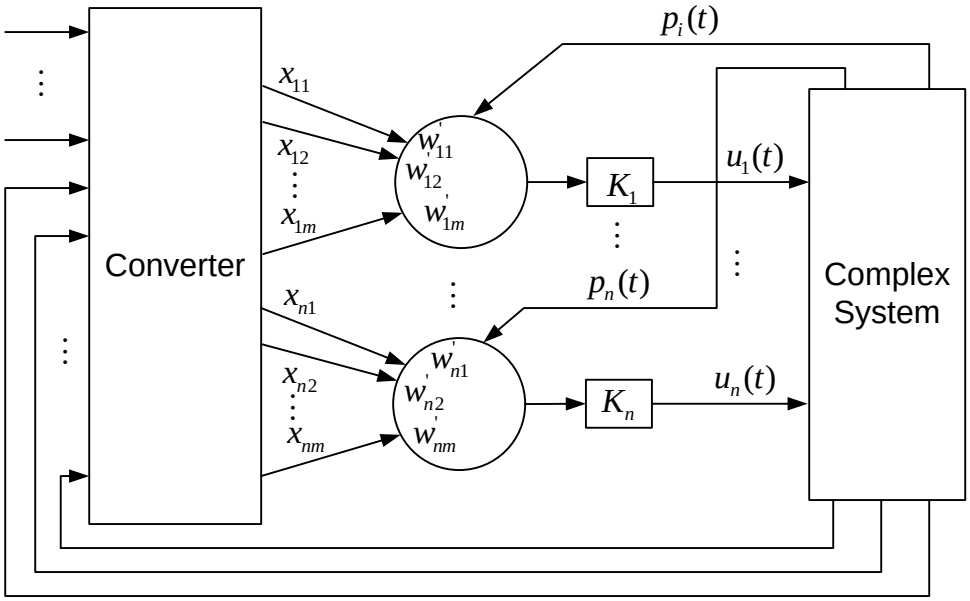

Figure 2.10: Multi-variable SNC network control system

2.5 Optimal-SNC/Optimal-SNC-PID Controller

Although the learning rule in the original SNC/SNC-PID control algorithms works well, SNC/SNC-PID still have the ability to improve the performance by changing the learning rule. In order to improve the control performance, a nonlinear opti-

mization algorithm module, SNOPT, with a novel object function is introduced for the learning rule and for updating all of the weights w_{ij} and the gain K_i of all SNC controllers. Since SNOPT is considered slow for real time applications and cannot be directly used in the real-time process, the kd-tree is introduced to the algorithm for improving calculation speed.

2.5.1 SNOPT

SNOPT is a software package, written by Philip Gill, Walter Murray and Michael Saunders [36], for solving large-scale optimization problems. It is especially effective for nonlinear problems with functions and gradients that are hard to calculate.

In this work we developed an algorithm to use optimization(SNOPT) in SNC controllers as described in Figure 2.11. First, w_{ij} and K_i are defined as design variables in optimization software(SNOPT). Second, a new objective function is proposed by the author and is described in equation 2.45.

$$f = \sum_{i=1}^{n} K_1\left(\frac{2}{1+e^{-K_2 e_i^2}} - 1\right) \tag{2.45}$$

$$e_i(t) = r_i(t) - y_i(t) \tag{2.46}$$

where i is the number of SNC controllers, e_i is the error of the system output, $r_i(t)$ is the reference system output, and $y_i(t)$ is the system output. K_1 and K_2 are two large value constants. If K_1 and K_2 are suitable, f is sensitive to tiny error changes. That is, if an error just changes a little bit, f will change a lot.

Third, the force $u_i(t)$ is calculated with the value of w_{ij} and K_i according to

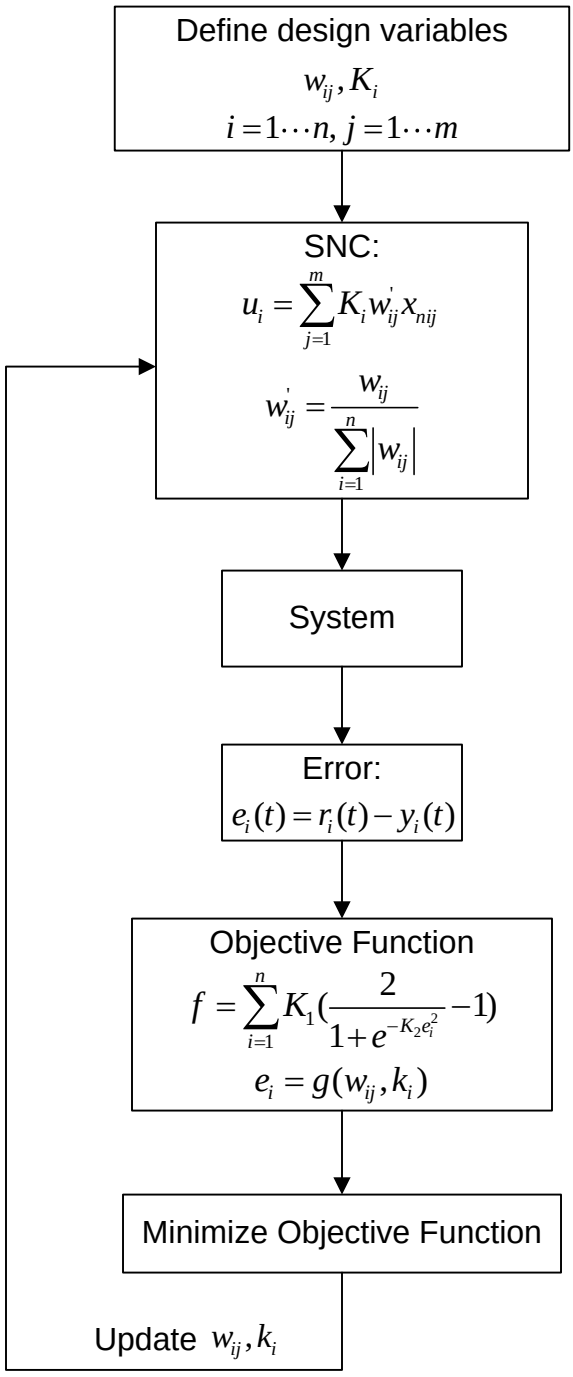

Figure 2.11: Optimization(SNOPT) in SNC controller

Equations 2.42 and 2.43. Fourth, apply the forces $u_i(t)$ into the system, and the system output $y_i(t)$ is computed. Then, the error $e_i(t)$ is calculated from equation 2.46. Next, the error is entered into in the objective function f, then the optimization solver NPOPT in SNOPT will minimize the f value. In every step, NPOPT will be called recursively and quits until reaching local optimal values of $w_{ij}(t)$ and $K_i(t)$. u_i is a function of w_{ij} and K_i, the system output y_i is a function of u_i, and the output e_i is a function of y_i. According to the chain rule, the objective function f is a function of w_{ij} and K_i. At every step in the control process, the SNOPT solver NPOPT is called to minimize the system output error e_i.

2.5.2 Kd-tree

A kd-tree (short for k-dimensional tree) is a data structure for storing points in a k-dimensional space [37]. A kd-tree is a binary tree, in which its parent nodes have at most two children nodes. To locate a point in a space, the method searches the data space using a multi-level searching algorithm. When it gets closer to the point, kd-tree uses information from the surrounding points to compute the best guess to the location of the point.

Figure 2.12 shows a two dimensional kd-tree example. In this example, a kd-tree structure is built for 11 points in the Cartesian x-y plane as shown in Figure 2.12a. At the first step, all the points split into two sub-domains using a vertical or horizontal line. The line is called a level, which in this case represents the first level, level 1 in the Figure2.12a. The method will choose the location of the level such that each

sub-domain contains, as much as possible, the same number of points. The next step is to create the second level. This is done on each sub-domain by dividing it into two sections in a manner similar to that used with the first level of the whole domain. With the second levels, we now have four sub-domains. The latter process will continue until we reach the last level where each point is contained inside one box defining the boarder of the point, named the domain of the point. Figure 2.12b depicts the final structure of the kd-tree for all points in the domain. In a k-dimensional space, horizontal or vertical lines will be hyperplanes.

To search for a point nearest the target location in the data space, such as P_* in Figure 2.12a, the kdtree uses the location of the levels as indicators of where the point P_* is located. First, P_* is examined with the first level and it is determined which subdomain the point is in, left or right. Then, this is done recursively until P_* is in a box. Finally, the method will use the information from the nearby surrounding points to choose the nearest neighbor.

The comparison of numerical performance of searching a nearest neighbor point using the kd-tree algorithm and the brute-force method is shown in Table 2.1. The brute-force method checks the target point with each point in the data space one by one. N is the points number. The data in the second and third columns of Table 2.1 represent the consuming time of the algorithms in seconds. The computer used in the comparison is a 64bit Linux computer with an 8-core 3.0GHz Intel Xeon CPU and 16GB memory. Each algorithm runs 10 times, and the consuming time in Table 2.1 represents the mean value of the results. The results show that the kd-tree

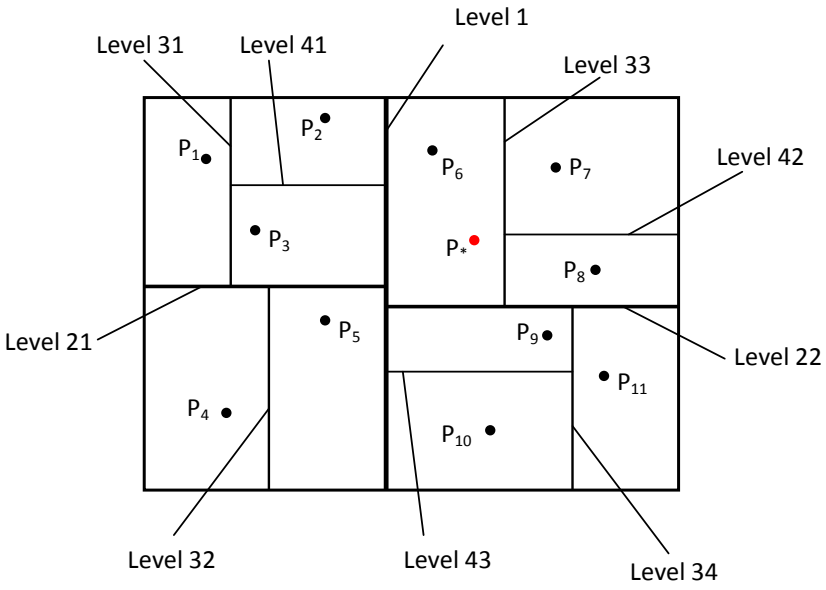

(a) Two dimensional points

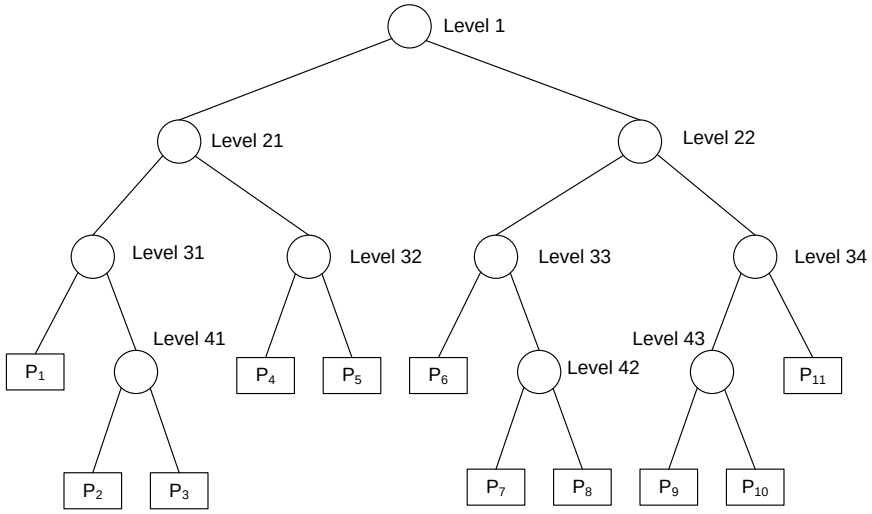

(b) Resulting kd-tree

Figure 2.12: Kd-tree

algorithm is much more efficient than the brute-force method, especially for a large number of points.

The kd-tree Maltab code was written by Steven Michael and can be downloaded from Mathwork website [38].

Table 2.1: Consuming time

N	Brute-force search(s)	kd-tree(s)
5×10^3	0.0006796	0.0001433
5×10^4	0.0051597	0.0001779
5×10^5	0.0512215	0.0001985
5×10^6	0.5278497	0.0002332
5×10^7	5.1730827	0.0004562

The proposed structure of the kd-tree in the Optimal-SNC/Optimal-SNC-PID algorithm of this work is described in the flow charts of Figure 2.13. The left chart in Figure 2.13 shows the steps using in building the kd-tree data space, where the data including $y_i(t)$, $w_{ij}(t)$, and $K_i(t)$ are first computed using SNOPT. This is followed by calculating $e_i(t)$ and $\Delta e_i(t)$. Finally, the kd-tree of $w_{ij}(t)$ and $K_i(t)$ are built based on $e_i(t)$ and $\Delta e_i(t)$.

The right flow chart in Figure 2.13 depicts the steps when using the kd-tree as

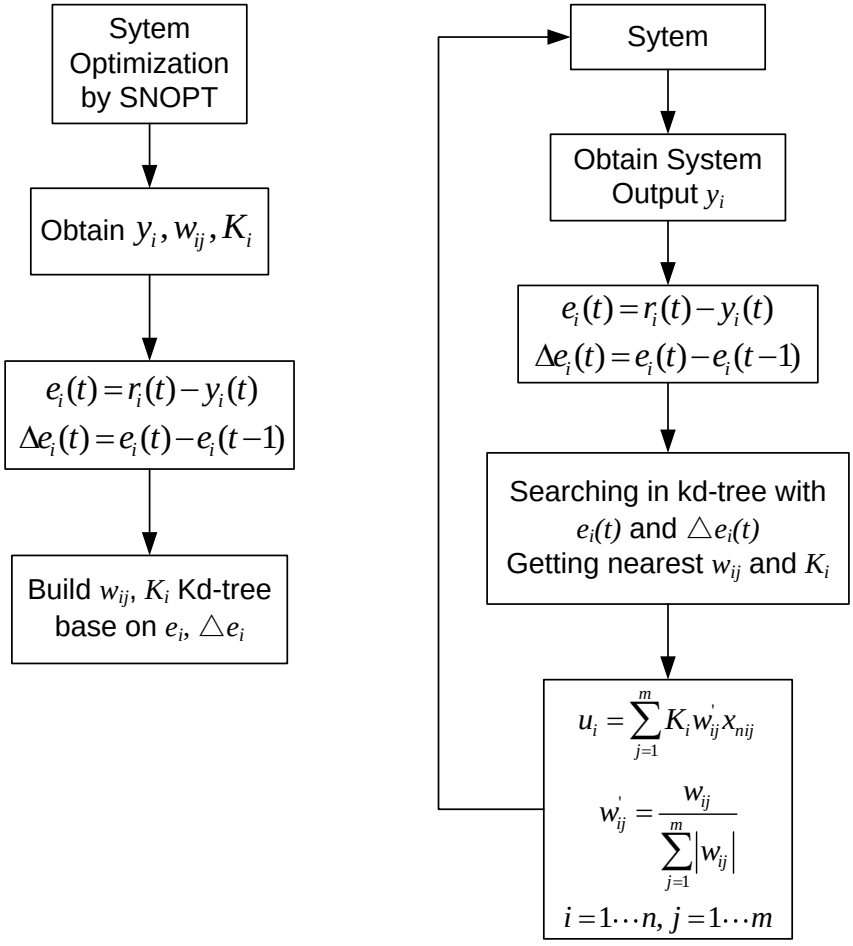

Figure 2.13: Kd-tree in SNC

a part of the system's solution process. In the system's solution process and during every step, the system output $y_i(t)$, $e_i(t)$ and $\Delta e_i(t)$ are calculated. With $e_i(t)$ and $\Delta e_i(t)$, a set of $w_{ij}(t)$ and $K_i(t)$ are found from the kd-tree data space. The resulting $w_{ij}(t)$ and $K_i(t)$ are used to calculate the force $u_i(t)$ using Equation 2.42 and 2.43. The resulting force $u_i(t)$ is then used as an input to the system, and the new output $y_i(t+1)$ is calculated. The process is then repeated for the next step until the control process reaches the finish time.

CHAPTER 3
VIBRATION SUPPRESSION OF SYSTEMS

In this chapter, the proposed Optimal-SNC/Optimal-SNC-PID control algorithm of Section 2.5 and the kd-tree search algorithm of Section 2.5.2 are implemented and compared with other control algorithms of Chapter 2 using mechanical systems. The mechanical systems are a single-degree-of-freedom mass-spring-damper system and several multi-degree-of-freedom systems. All systems are supported on vibrating bases and augmented with one or more active dampers to control and mitigate the transmitted vibration to the system.

3.1 Excitation Functions

3.1.1 Earthquake Data

Several earthquake data were used as the excitation functions that represent the base motion of the system. The excitation functions include the El Centro earthquake data, PET-UP, PSA-UP, SBA-UP, and 13160-UP. The El Centro earthquake happened in El Centro, California on May 18, 1940. The data is the north-south component of the ground motion and was obtained from vibrationdata.com [39]. The original data is the acceleration ratio with respect to the gravity acceleration. The sampling time is $0.02s$. The top curve in Figure 3.1 shows the ground acceleration with time. The velocity of the signal is calculated by integrating the acceleration signal with time (the middle curve in Figure 3.1). Subsequently, the ground displacement is calculated by integrating the velocity with time (the lower curve in Figure

3.1). As can be seen from Figure 3.1, the El Centro earthquake is strong and has a maximum amplitude around $0.212m$.

Other earthquake data are obtained from the PEER NGA strong motion database of Berkeley university [40].

3.2 A Single Degree of Freedom Forced Vibration System

A single-degree-of-freedom mass-spring system is shown in Figure 3.2. The system is supported on a base that is allowed to move vertically. y_0 is the excitation input function, y is the mass displacement, k is the spring stiffness, and u is the active force determined by the control algorithms described in Chapter 2. In real-life applications, u could be produced by MR/ER dampers.

When the excitation input function is applied to base of the system, the mass m vibrates subsequently. The active force u is then applied to the system to suppress and minimize the motion of the mass and tries to keep the mass at the original equilibrium position.

The system is governed by the following differential equation.

$$m\ddot{y} + ky - u - ky_0 = 0 \tag{3.1}$$

If x_1 is set as y and x_2 is set as $\dot{y}$, then Equation 3.1 is transferred to the state-space equation.

$$\begin{pmatrix} \dot{x_1} \\ \dot{x_2} \end{pmatrix} = \begin{pmatrix} 0 & 1 \\ -\frac{k}{m} & 0 \end{pmatrix} \begin{pmatrix} x_1 \\ x_2 \end{pmatrix} + \begin{pmatrix} 0 & 0 \\ \frac{k}{m} & \frac{1}{m} \end{pmatrix} \begin{pmatrix} y_0 \\ u \end{pmatrix}$$

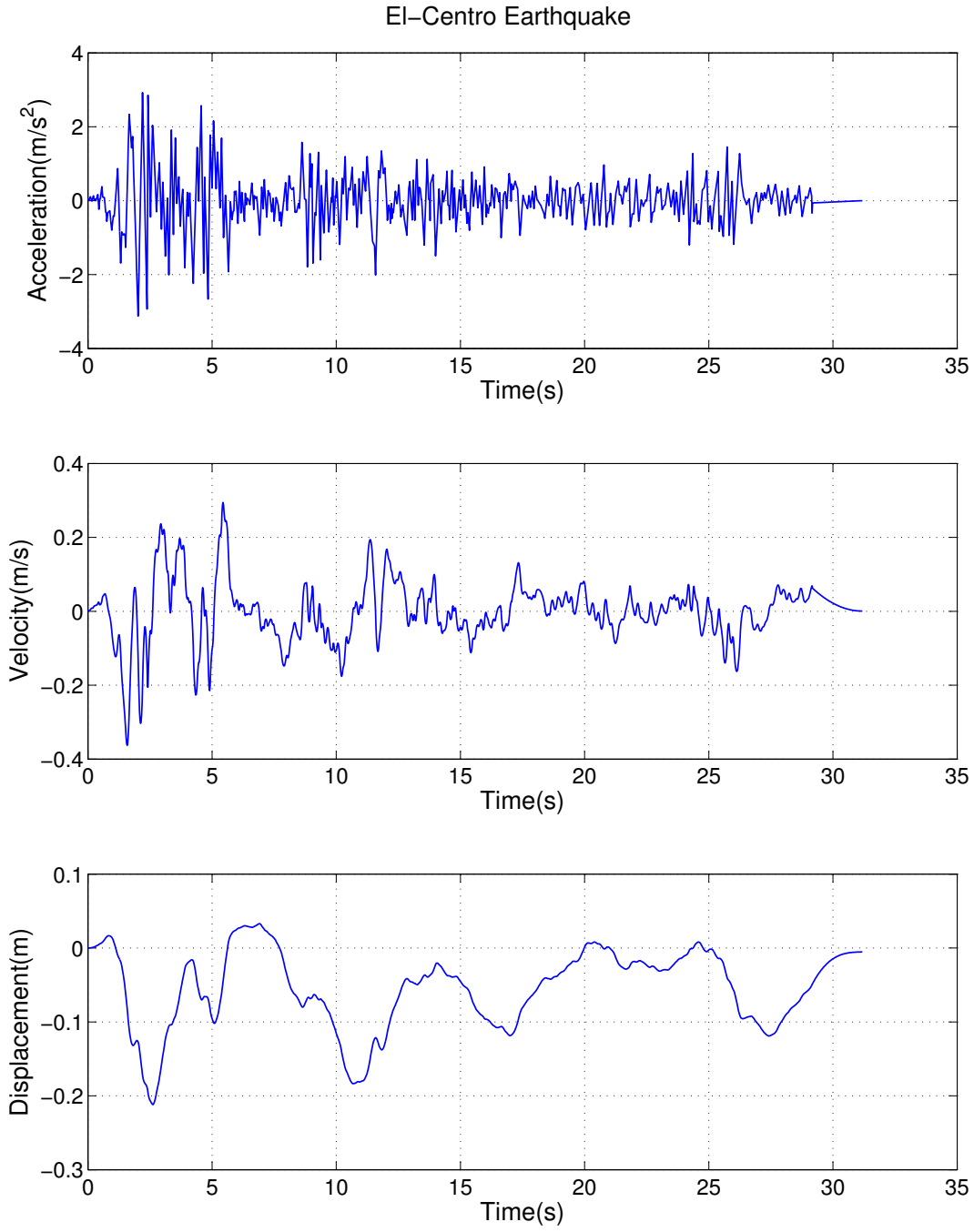

Figure 3.1: El-Centro earthquake data

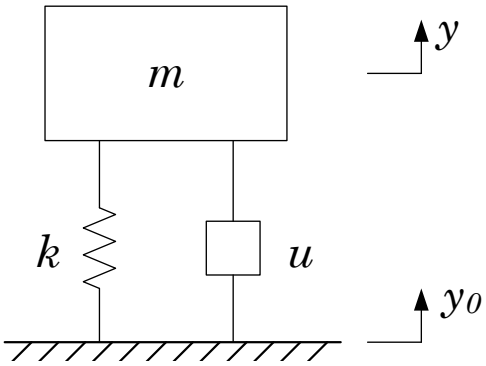

Figure 3.2: A single degree of freedom force vibration system

$$y = \begin{pmatrix} 1 & 0 \end{pmatrix} \begin{pmatrix} x_1 \\ x_2 \end{pmatrix} \tag{3.2}$$

Therefore,

$$\begin{aligned} \dot{\mathbf{x}} &= \mathbf{A}\mathbf{x} + \mathbf{B}\mathbf{u} \\ y &= \mathbf{C}\mathbf{x} \end{aligned} \tag{3.3}$$

where

$$\mathbf{x} = \begin{pmatrix} x_1 \\ x_2 \end{pmatrix} = \begin{pmatrix} y \\ \dot{y} \end{pmatrix}, \mathbf{u} = \begin{pmatrix} y_0 \\ u \end{pmatrix},$$

$$\mathbf{A} = \begin{pmatrix} 0 & 1 \\ -\frac{k}{m} & 0 \end{pmatrix}, \mathbf{B} = \begin{pmatrix} 0 & 0 \\ \frac{k}{m} & \frac{k}{m} \end{pmatrix}, \mathbf{C} = \begin{pmatrix} 1 & 0 \end{pmatrix}.$$

Thus, the system is a two-input, single-output system where u and y_0 are the system's inputs and y is the system's output.

The parameters of the system are $m = 10$kg and $k = 40$N/m. The control parameters of the control algorithms of Chapter 2 are as following:

PID: $K_p = 1100$, $T_i = 0.5$, $T_d = 0.5$.

SNC-PID: $w_1 = 450$, $w_2 = 880$, $w_3 = 40$, which are initial values for the weights.

$$K = 1000,\ d_1 = 1.0 \times 10^8,\ d_2 = 9.0 \times 10^6,\ d_3 = 6.0 \times 10^4.$$

LQR: $\mathbf{K} = \begin{pmatrix} 0 & 0 \\ 38520 & 878 \end{pmatrix}$.

LQG: $\mathbf{K} = \begin{pmatrix} 0 & 0 \\ 48445.5 & 984.5 \end{pmatrix}$.

Optimal-SNC-PID: As described in Section 2.5 on page 29, w_{ij} and K_i are optimized by SNOPT under the El-Centro earthquake data excitation. Then, the kd-tree database of w_{ij} and K_i is built based on the resulting e and Δe.

The results using the different control algorithms are shown Figure 3.3-3.8. Figure 3.3 shows the displacement of the mass without control and with control. The magenta curve is the El-Centro earthquake data, which represents the motion of the base. The orange line is the displacement of the mass without control. It is clear from the figure that all of the control algorithms did fairly well. All algorithms suppressed the mass displacement by considerable amounts. Figure 3.4 demonstrates the

displacement of the mass using the different control algorithms where the PID algorithm performed poorly compared to the rest of the algorithms under investigation. Figure 3.5 shows that the proposed Optimal-SNC-PID algorithm is the best. The LQR still has an advantage, in that the displacement is much smoother than those of the other algorithms.

In this example, the database for the Optimal-SNC-PID was built base on the control forces using the El-Centro earthquake data. In order to validate the algorithm, other earthquakes' data are applied to the system. The control results for the PET-UP earthquake data are shown in Figure 3.6, 3.7, and 3.8, respectively. The PET-UP earthquake was also a strong ground motion and took place in Cape Mendocind, California, on April 25, 1992. As shown in Figure 3.8, the Optimal-SNC-PID performs the best among all of the control algorithms under investigation. There are 2,500 points in the kd-tree data structure.

3.3 Two-Degree-Of-Freedom Forced Vibration Systems

3.3.1 A Two-Mass-Spring System

A two-degree-of-freedom, i.e., a two-mass-spring system, is shown in Figure 3.9. There are two masses in the system, and each mass is supported by a linear spring and an active damper. The system is supported on the moving base. y_0 represents the excitation functions, which are earthquake data. y_1 is the displacement of the 1st mass, and y_2 is the displacement of the 2nd mass. k_1 and k_2 are the stiffness of the 1st and 2nd springs, respectively. u_1 and u_2 are the active forces produced by

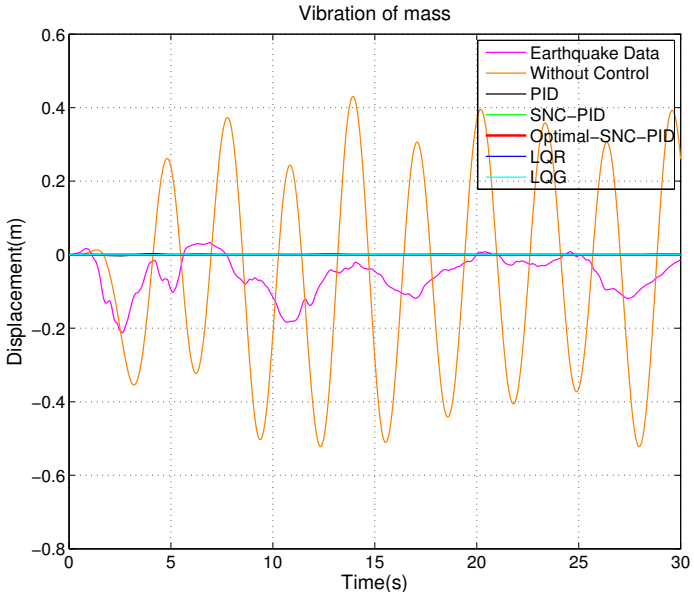

Figure 3.3: Results with control and without control

of a single-mass-spring system for El-Centro earthquake

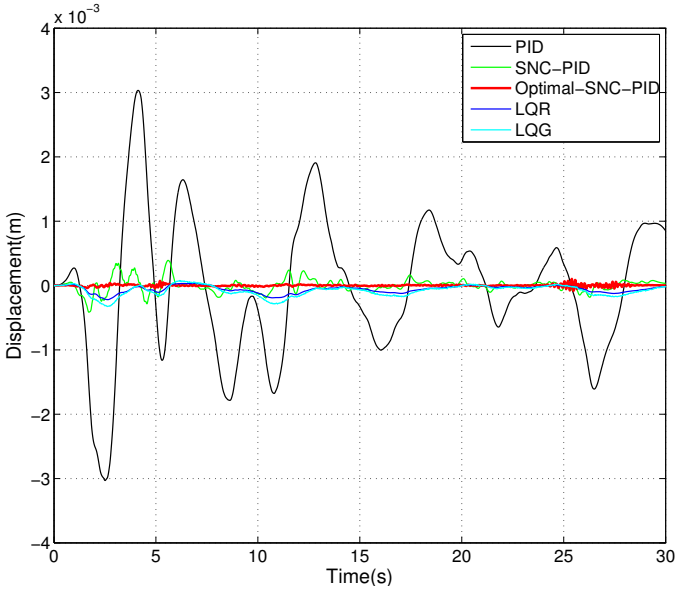

Figure 3.4: Control results of a single-mass-spring system

for El-Centro earthquake

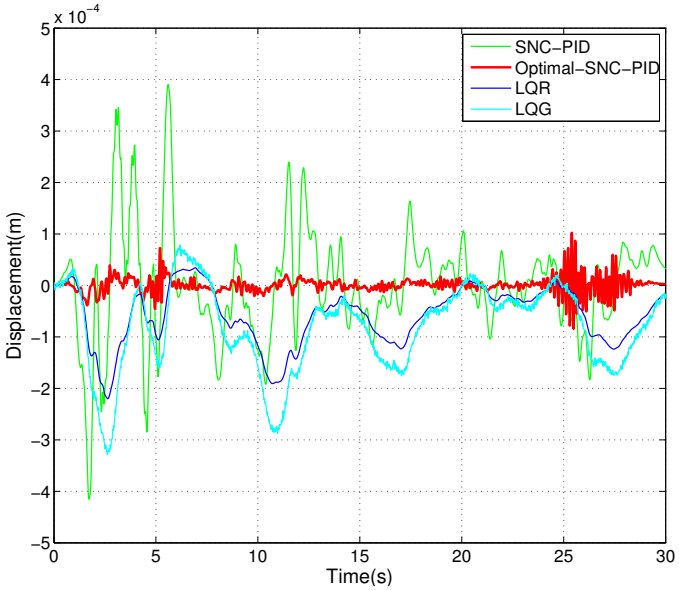

Figure 3.5: Control results except PID of a single-mass-spring system for El-Centro earthquake

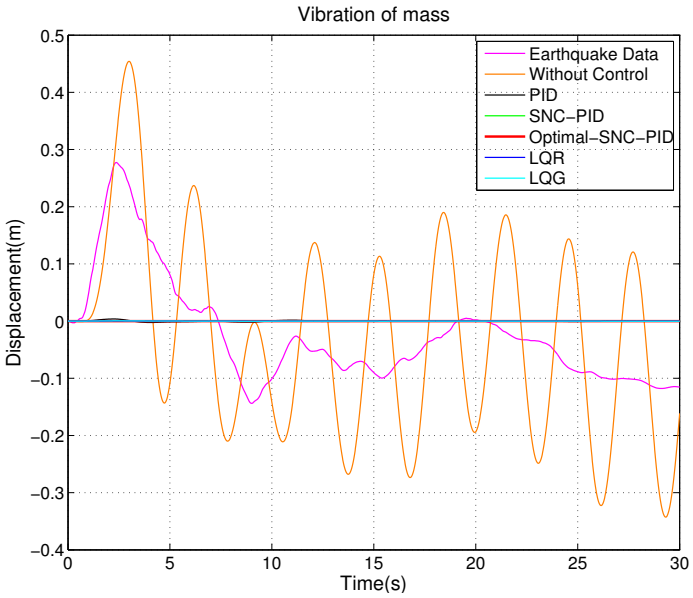

Figure 3.6: Results with control and without control of a single-mass-spring system for PET-UP earthquake

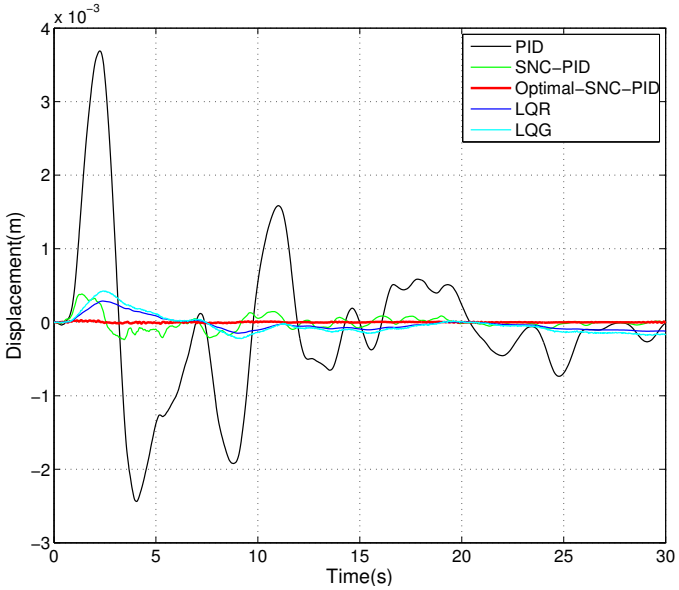

Figure 3.7: Control results of a single-mass-spring system

for PET-UP earthquake

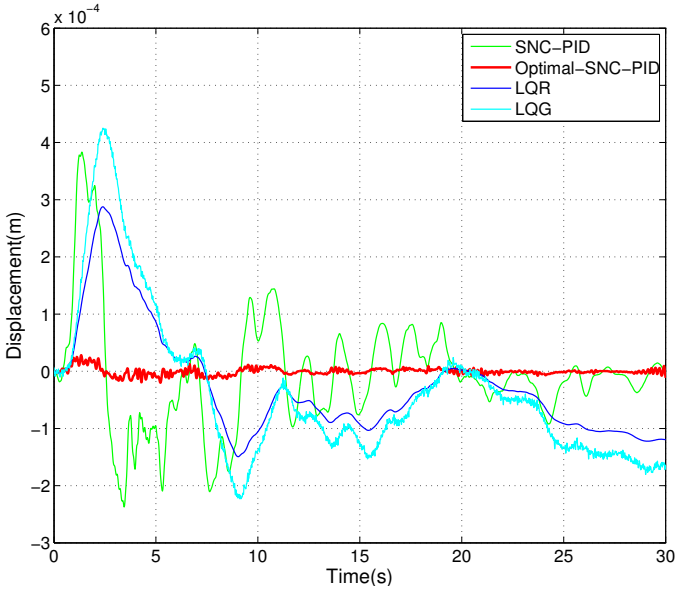

Figure 3.8: Control results except PID of a single-mass-spring system

for PET-UP earthquake

active dampers. u_1 and u_2 are determined by control algorithms. When the base begins vibrating, the masses start moving from their equilibrium static positions. Then, the active forces u_1 and u_2 start to work, suppress the vibration, and keep the masses at the original equilibrium positions.

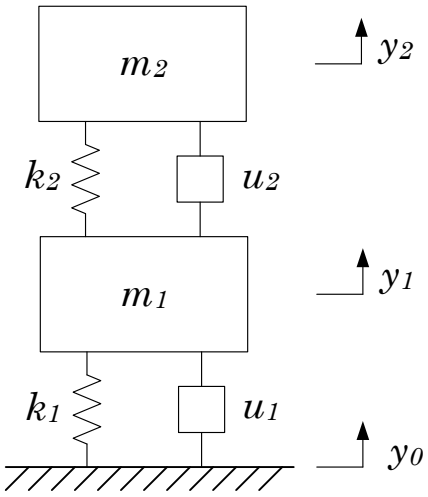

Figure 3.9: A two-mass-spring system

The mathematical model of the system is

$$m_1\ddot{y}_1 + (k_1 + k_2)y_1 - k_2y_2 = u_1 - u_2 + k_1y_0 \tag{3.4}$$

$$m_2\ddot{y}_2 - k_2y_1 + k_2y_2 = u_2 \tag{3.5}$$

Set $x_1 = y_1$, $x_2 = y_2$, $x_3 = \dot{y}_1$, and $x_4 = \dot{y}_2$, the differential equations 3.4 and

3.5 are transferred to the state-space equation.

$$\begin{aligned} \dot{\mathbf{x}} &= \mathbf{A}\mathbf{x} + \mathbf{B}\mathbf{u} \\ \mathbf{y} &= \mathbf{C}\mathbf{x} \end{aligned} \tag{3.6}$$

where

$$\mathbf{x} = \begin{pmatrix} x_1 \\ x_2 \\ x_3 \\ x_4 \end{pmatrix} = \begin{pmatrix} y_1 \\ y_2 \\ \dot{y}_1 \\ \dot{y}_2 \end{pmatrix}, \mathbf{y} = \begin{pmatrix} y_1 \\ y_2 \end{pmatrix}, \mathbf{u} = \begin{pmatrix} y_0 \\ u_1 \\ u_2 \end{pmatrix},$$

$$\mathbf{A} = \begin{pmatrix} 0 & 0 & 1 & 0 \\ 0 & 0 & 0 & 1 \\ -\frac{k_1+k_2}{m_1} & \frac{k_2}{m_1} & 0 & 0 \\ \frac{k_2}{m_2} & -\frac{k_2}{m_2} & 0 & 0 \end{pmatrix}, \mathbf{B} = \begin{pmatrix} 0 & 0 & 0 \\ 0 & 0 & 0 \\ \frac{k_1}{m_1} & \frac{1}{m_1} & -\frac{1}{m_1} \\ 0 & 0 & \frac{1}{m_2} \end{pmatrix},$$

$$\mathbf{C} = \begin{pmatrix} 1 & 0 & 0 & 0 \\ 0 & 1 & 0 & 0 \end{pmatrix},$$

The system is a linear weak coupled system, because, if u_1 works well and suppresses the vibration from the base, y_1 will be small and around 0. Then, for the second mass, the vibration and the influence from the 1st mass is relatively small. Thus, u_2 can use only small forces to suppress the vibration, and this keeps the second mass vibrating near the original equilibrium position.

The parameters of the system are $m_1 = 12$kg, $m_2 = 10$kg, $k_1 = 60$N/m, and

$k_2 = 50\text{N/m}$. The control parameters of the control algorithms of Chapter 2 are as following:

PID: for u_1, $K_p = 960$, $T_i = 1.0$, $T_d = 0.7$,

for u_2, $K_p = 500$, $T_i = 1.1$, $T_d = 1.1$.

SNC-PID: for u_1, $w_1 = 44$, $w_2 = 38$, $w_3 = 1.6$, $K_1 = 480$, $d_1 = 5$,

for u_2, $w_1 = 21$, $w_2 = 16.6$, $w_3 = 1.5$, $K_2 = 90$, $d_2 = 5$.

$$\textbf{LQR: } \mathbf{K} = \begin{pmatrix} 0 & 0 & 0 & 0 \\ 5993.3 & 3292.6 & 375.2 & 263.3 \\ -2047.2 & 5761.2 & -59.2 & 334.7 \end{pmatrix}.$$

$$\textbf{LQG: } \mathbf{K} = \begin{pmatrix} 0 & 0 & 0 & 0 \\ 14080 & 8550 & 577 & 420 \\ -3825 & 13151 & -73 & 508 \end{pmatrix}.$$

The results using the different control algorithms are shown Figure 3.10-3.13. Figure 3.10 shows the resulting displacements of the two masses without and with the control algorithms. The curves in the top graph of Figure 3.10 are the displacements of y_1, and the curves in the bottom graph are the displacements of y_2. The magenta curve in the top graph is the input El-Centro earthquake data. In both graphs, the orange lines are the displacements of y_1 and y_2 without the control applied. It is clear from Figure 3.10 that all of the control algorithms worked quiet well and suppressed both y_1 and y_2 considerably. Figure 3.11 compares the results from the different control algorithms, where again the Optimal-SNC-PID was the most effective.

The databases for the Optimal-SNC-PID are based on the control forces corresponding to the El-Centro earthquake data. In order to validate the algorithm, other earthquakes' data are applied to the system. The control results for the PET-UP earthquake data are shown in Figure 3.12 and 3.13, respectively. The results show that the Optimal-SNC-PID is still the best control algorithms among those under investigation. The results also show that y_2 is about 10 times smaller than y_1. This confirms that the system is a weak coupled system. There are 2,500 points in the kd-tree data structure.

3.3.2 A Bar-Spring System

A bar-spring system is also in this investigation and is considered as a two-degree-of-freedom system where translational and rotational motions are allowed as shown in Figure 3.14. The bar is rigid with uniformly distributed mass m and length L and is supported by two linear springs and two active dampers at both ends of the bar. The system is attached to a base that is allowed to move in the vertical direction. y_0 is the excitation function, which represents earthquake data. There are two generalized coordinates for this system represented by the displacements of the two ends, y_1 and y_2. k_1 and k_2 are the stiffness of the springs at the left and right ends, respectively. u_1 and u_2 are the active forces produced by active dampers. u_1 and u_2 are determined by the control algorithms. When the base begins vibrating, the bar starts moving from its equilibrium static position. Then, the active forces u_1 and u_2 start to work, suppress the vibration, and keep the bar at the original

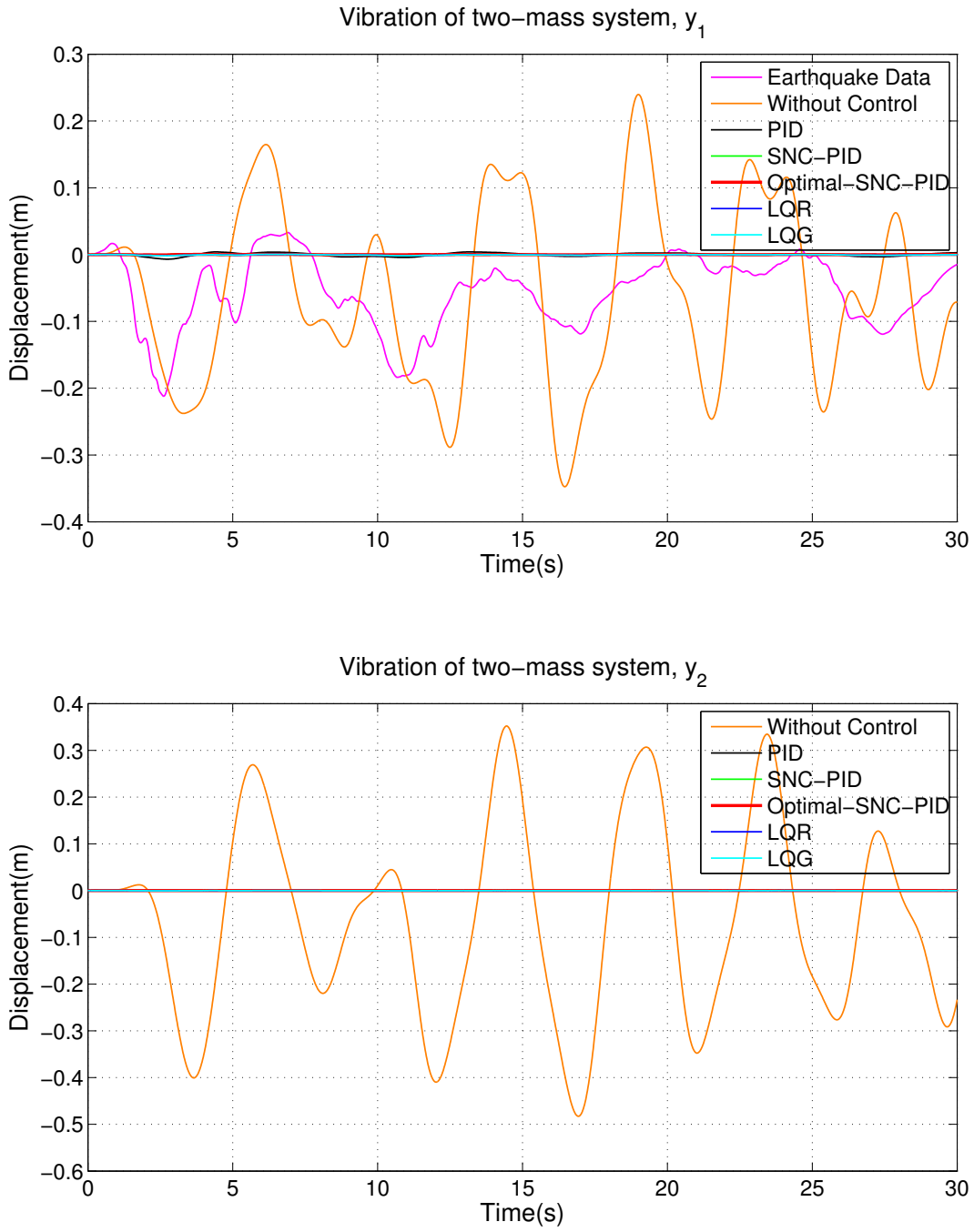

Figure 3.10: Results with control and without control

of a two-mass system for El-Centro earthquake

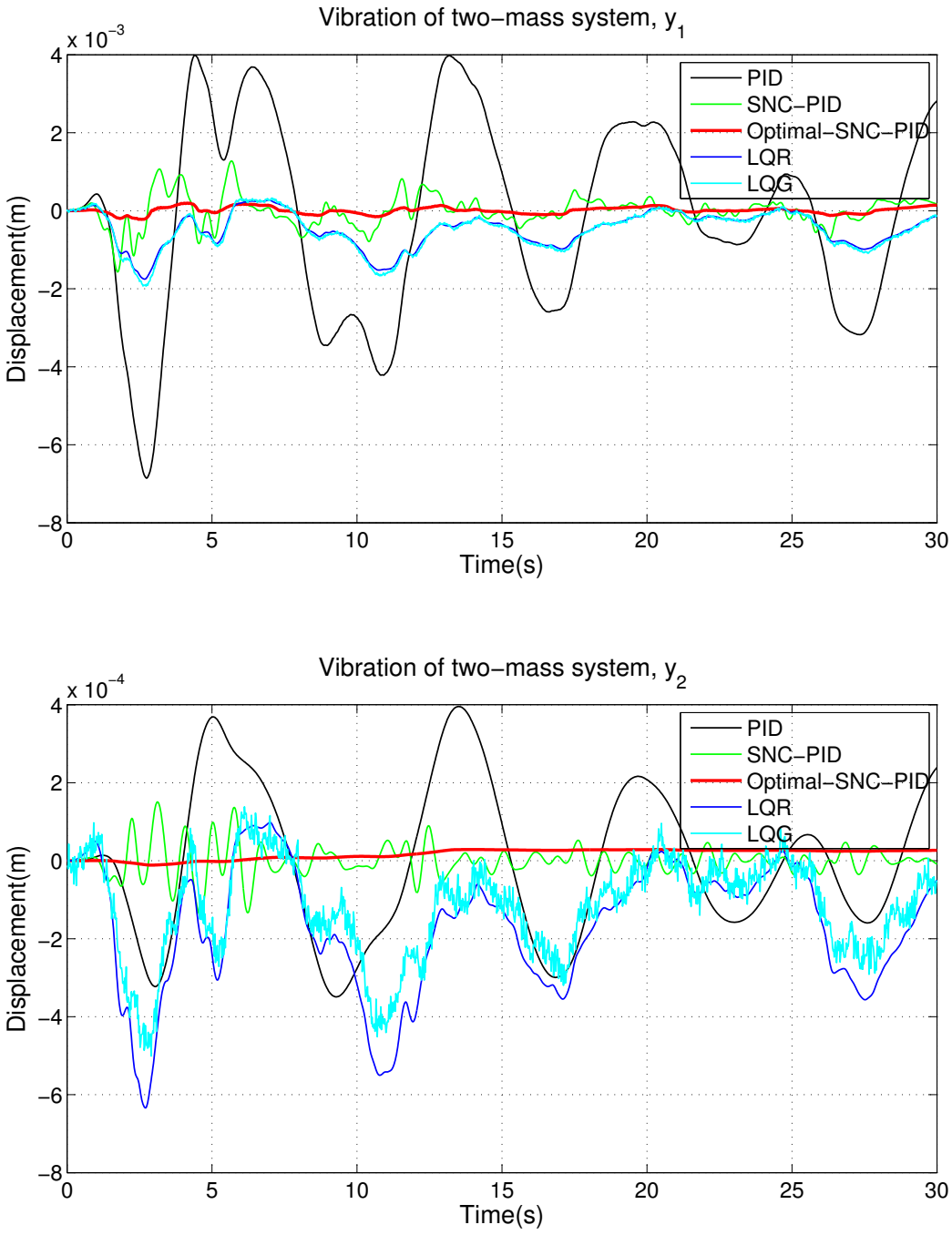

Figure 3.11: Control results of a two-mass system for El-Centro earthquake

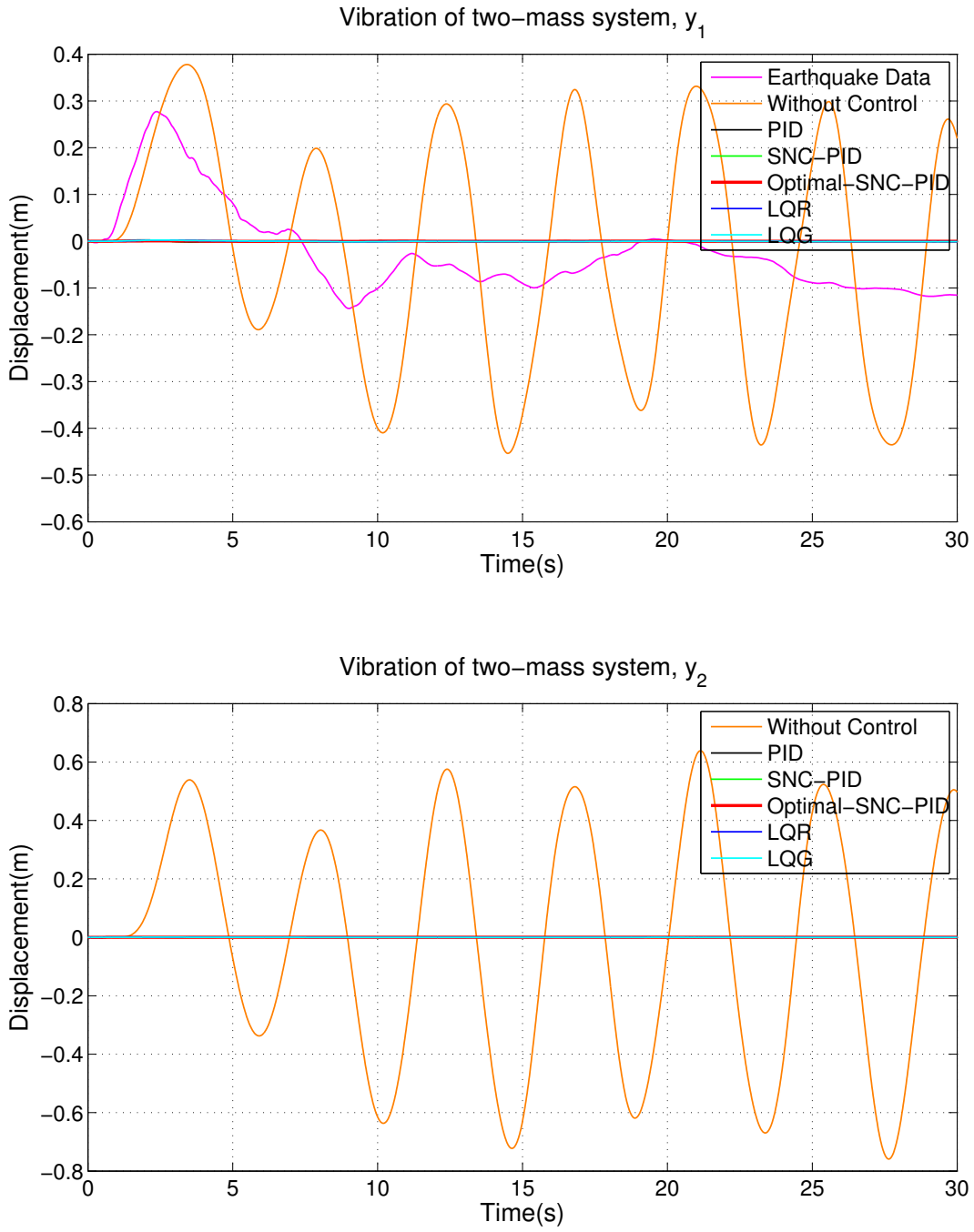

Figure 3.12: Results with control and without control

of a two-mass system for PET-UP earthquake

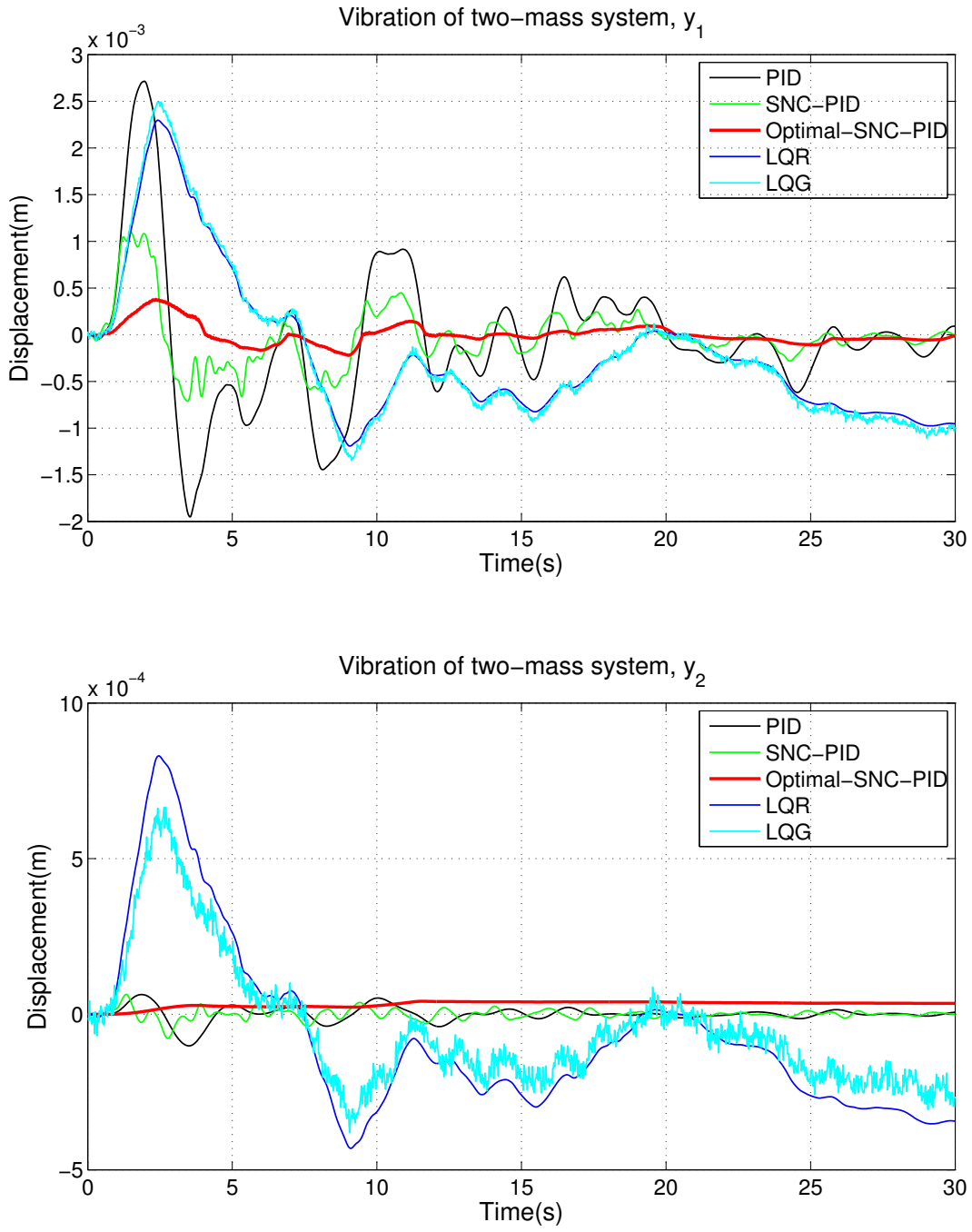

Figure 3.13: Control results of a two-mass system for PET-UP earthquake

equilibrium positions.

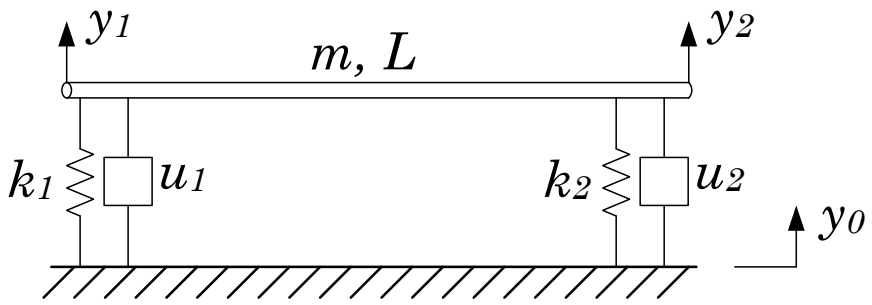

Figure 3.14: A bar-spring system

The bar-spring system is a nonlinear and strongly coupled system, because y_1 or y_2 are affected by both springs and active forces. Only when both y_1 and y_2 are small does the bar vibrate near the equilibrium position. If u_1 and u_2 work well, then the bar vibrates lightly, and y_1, y_2, and the rotation angle θ of the bar are small too. Therefore,

$$\theta \approx tg\theta = \frac{y_2 - y_1}{L} \tag{3.7}$$

Then, the linearized mathematical model of the system is gotten,

$$m\ddot{y}_1 + 4k_1y_1 - 2k_2y_2 = (4k_1 - 2k_2)y_0 + 4u_1 - 2u_2 \tag{3.8}$$

$$m\ddot{y}_2 - 2k_1y_1 + 4k_2y_2 = (-2k_1 + 4k_2)y_0 - 2u_1 + 4u_2 \tag{3.9}$$

Set $x_1 = y_1$, $x_2 = y_2$, $x_3 = \dot{y}_1$, and $x_4 = \dot{y}_2$, the differential equations 3.8

and 3.9 are transferred to the state-space equation.

$$\begin{aligned} \dot{\mathbf{x}} &= \mathbf{A}\mathbf{x} + \mathbf{B}\mathbf{u} \\ \mathbf{y} &= \mathbf{C}\mathbf{x} \end{aligned} \tag{3.10}$$

where

$$\mathbf{x} = \begin{pmatrix} x_1 \\ x_2 \\ x_3 \\ x_4 \end{pmatrix} = \begin{pmatrix} y_1 \\ y_2 \\ \dot{y}_1 \\ \dot{y}_2 \end{pmatrix}, \mathbf{y} = \begin{pmatrix} y_1 \\ y_2 \end{pmatrix}, \mathbf{u} = \begin{pmatrix} y_0 \\ u_1 \\ u_2 \end{pmatrix},$$

$$\mathbf{A} = \begin{pmatrix} 0 & 0 & 1 & 0 \\ 0 & 0 & 0 & 1 \\ -\frac{4k_1}{m} & \frac{2k_2}{m} & 0 & 0 \\ \frac{2k_1}{m} & -\frac{4k_2}{m} & 0 & 0 \end{pmatrix}, \mathbf{B} = \begin{pmatrix} 0 & 0 & 0 \\ 0 & 0 & 0 \\ \frac{4k_1 - 2k_2}{m} & \frac{4}{m} & -\frac{2}{m} \\ \frac{-2k_1 + 4k_2}{m} & -\frac{2}{m} & \frac{4}{m} \end{pmatrix},$$

$$\mathbf{C} = \begin{pmatrix} 1 & 0 & 0 & 0 \\ 0 & 1 & 0 & 0 \end{pmatrix}.$$

The parameters of the system are $m = 10$kg, $k_1 = 40$N/m, $k_2 = 30$N/m, and $L = 1$m. The control parameters of the control algorithms of Chapter 2 are listed as following:

PID: for u_1, $K_p = 580$, $T_i = 0.26$, $T_d = 0.14$,

for u_2, $K_p = 580$, $T_i = 0.26$, $T_d = 0.14$.

SNC-PID: for u_1, $w_1 = 7.4$, $w_2 = 12.3$, $w_3 = 0.3$, $K_1 = 225$, $d_1 = 0.6$,

for u_2, $w_1 = 7.4$, $w_2 = 12.3$, $w_3 = 0.3$, $K_2 = 225$, $d_2 = 0.6$.

$$\textbf{LQR: } \mathbf{K} = \begin{pmatrix} 0 & 0 & 0 & 0 \\ 4406 & 927.2 & 169.6 & 61.7 \\ 928.5 & 4413.9 & 61.7 & 169.7 \end{pmatrix}.$$

$$\textbf{LQG: } \mathbf{K} = \begin{pmatrix} 0 & 0 & 0 & 0 \\ 8193 & 2594.2 & 232.8 & 95.9 \\ 2595.1 & 8200.8 & 95.9 & 232.8 \end{pmatrix}.$$

The results using the different control algorithms are shown Figures 3.15-3.18. The curves in the top graph of Figure 3.15 are the displacements of y_1, and the curves in the bottom graph are the displacements of y_2. The magenta curve is the El-Centro earthquake data. The orange lines are the displacements of y_1 and y_2 without control algorithms applied. It is clear that all of the control algorithms worked quiet well. They suppressed both y_1 and y_2 significantly. In order to compare the control algorithms, the control results are shown in Figure 3.16.

Figure 3.16 shows that the Optimal-SNC-PID has the best performance because the displacements of y_1 and y_2 are the smallest among all of the control results.

The databases for the Optimal-SNC-PID are based on the control forces corresponding to the El-Centro earthquake data. In order to validate the algorithm, other earthquakes' data are applied to the system. The control results for the PET-UP earthquake data are shown in Figure 3.17 and 3.18, respectively. The results show that the Optimal-SNC-PID is still the best control algorithm among those under investigation. There are 2,500 points in the kd-tree data structure.

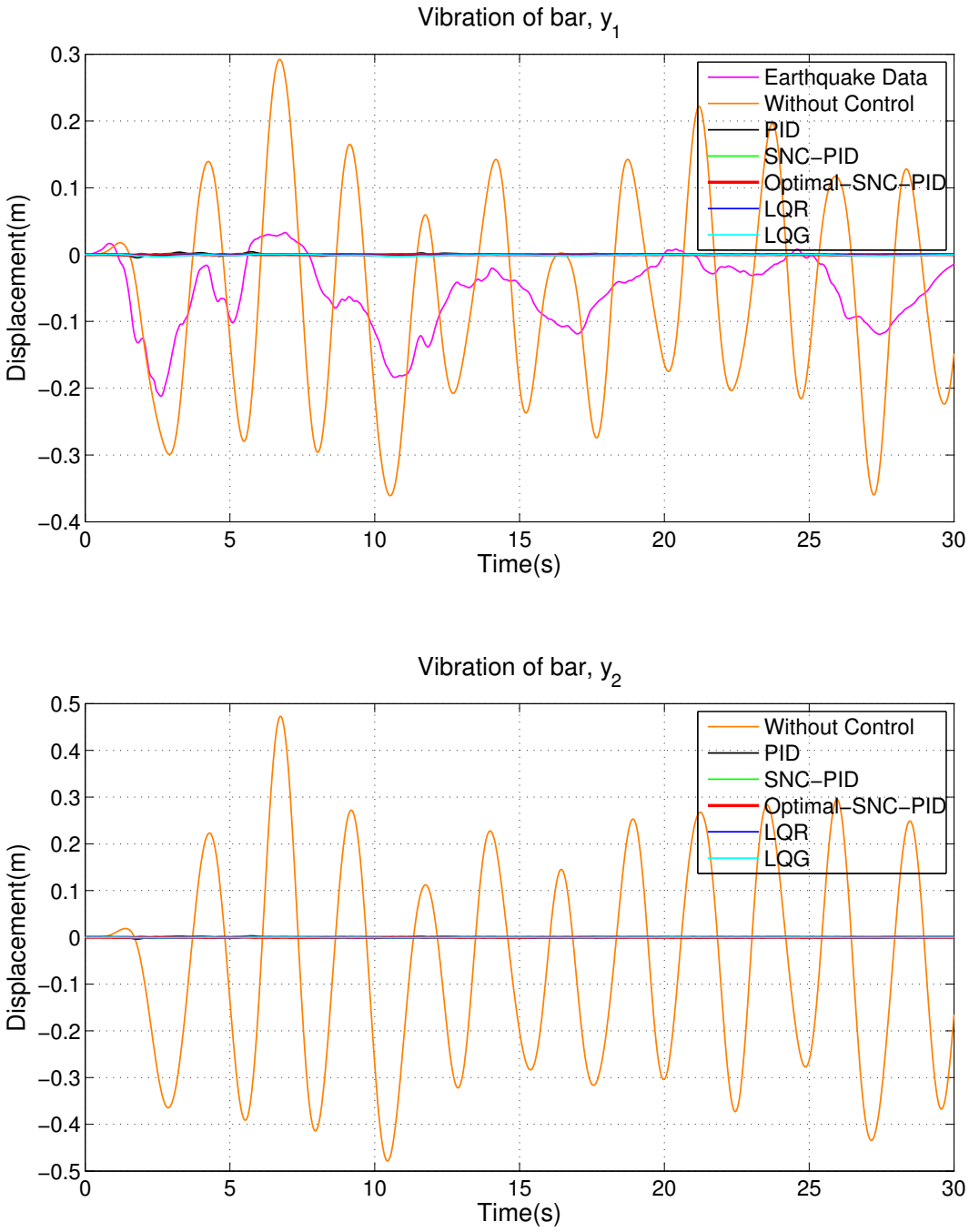

Figure 3.15: Results with control and without control

of a bar-spring system for El-Centro earthquake

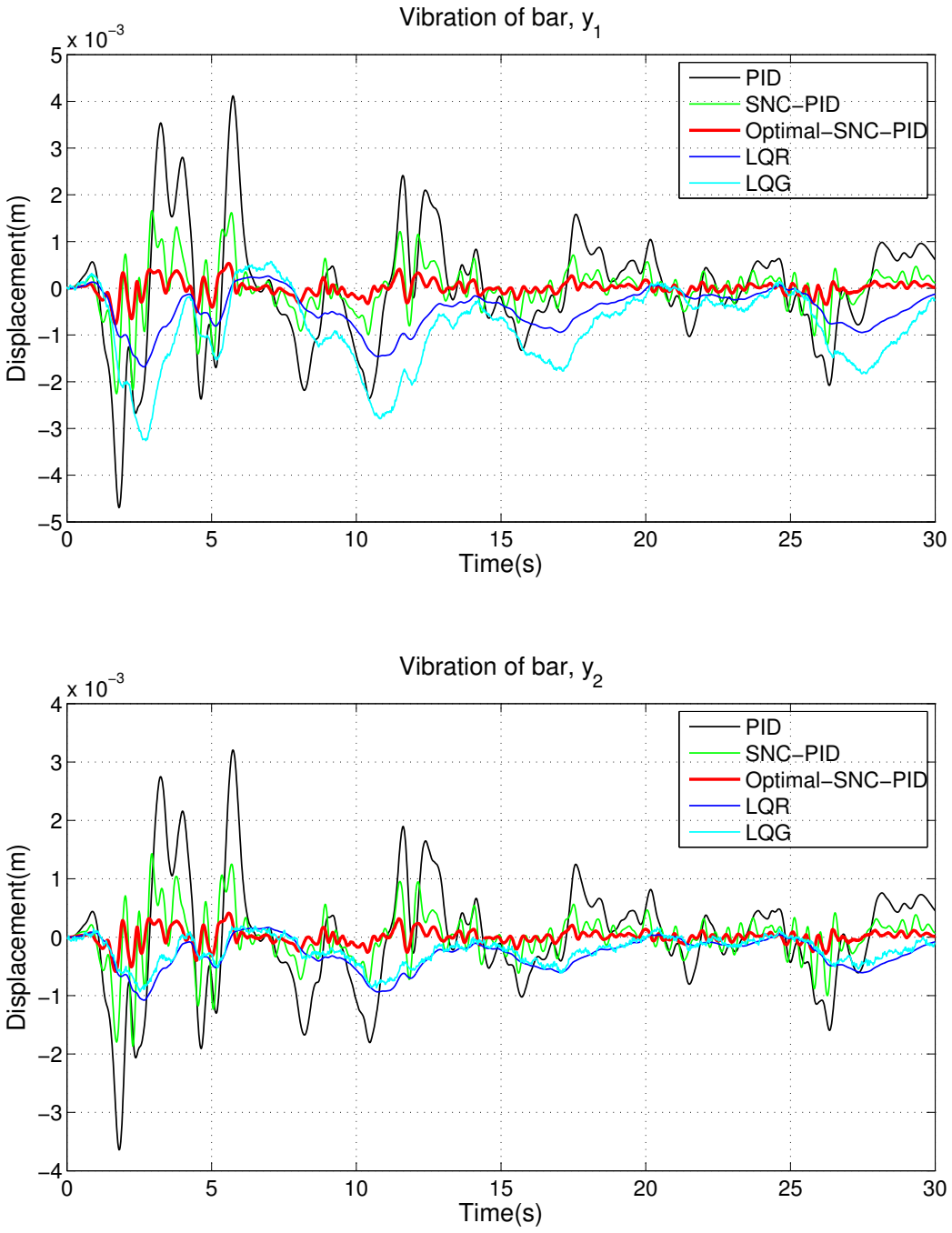

Figure 3.16: Control results of a bar-spring system for El-Centro earthquake

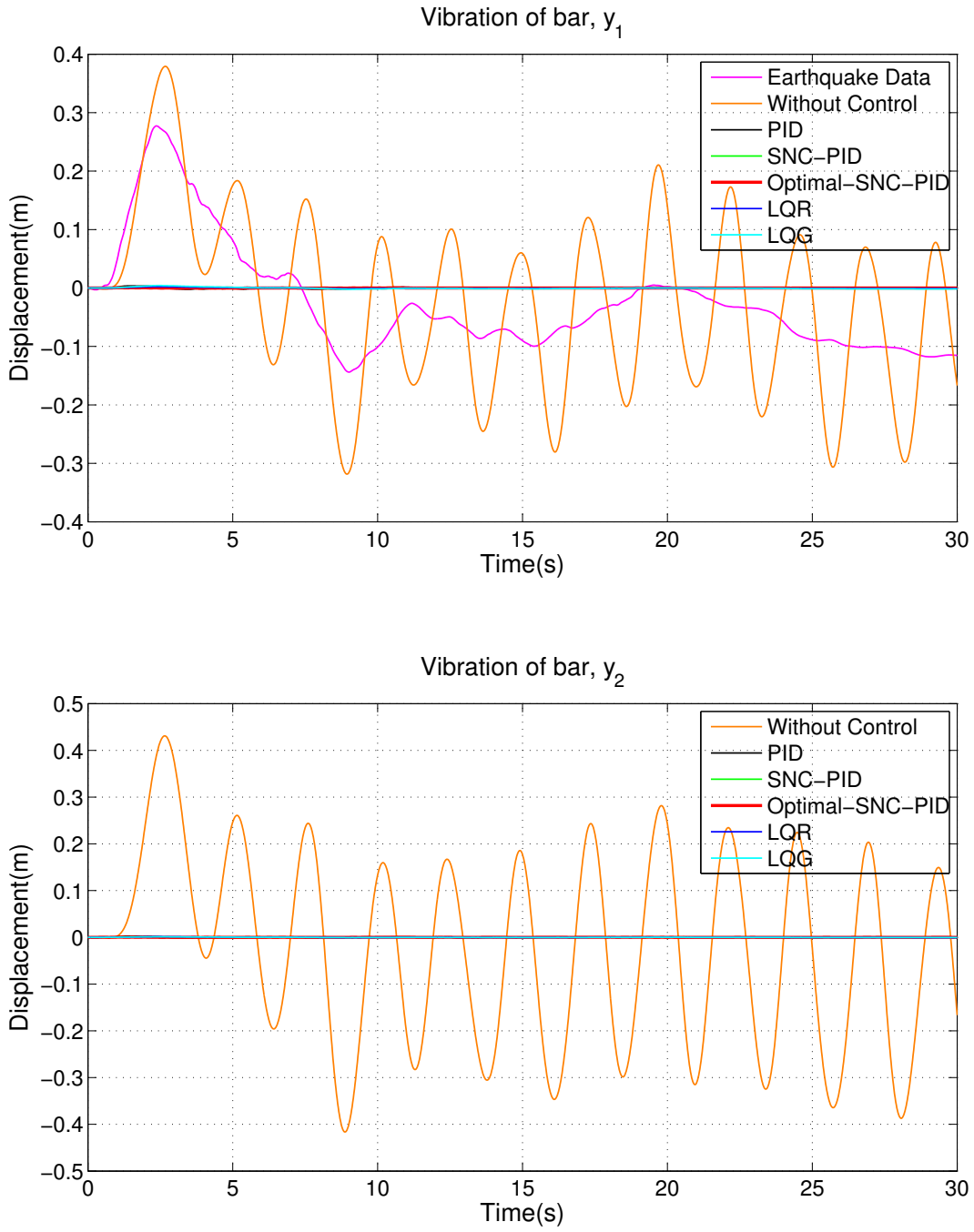

Figure 3.17: Results with control and without control

of a bar-spring system for PET-UP earthquake

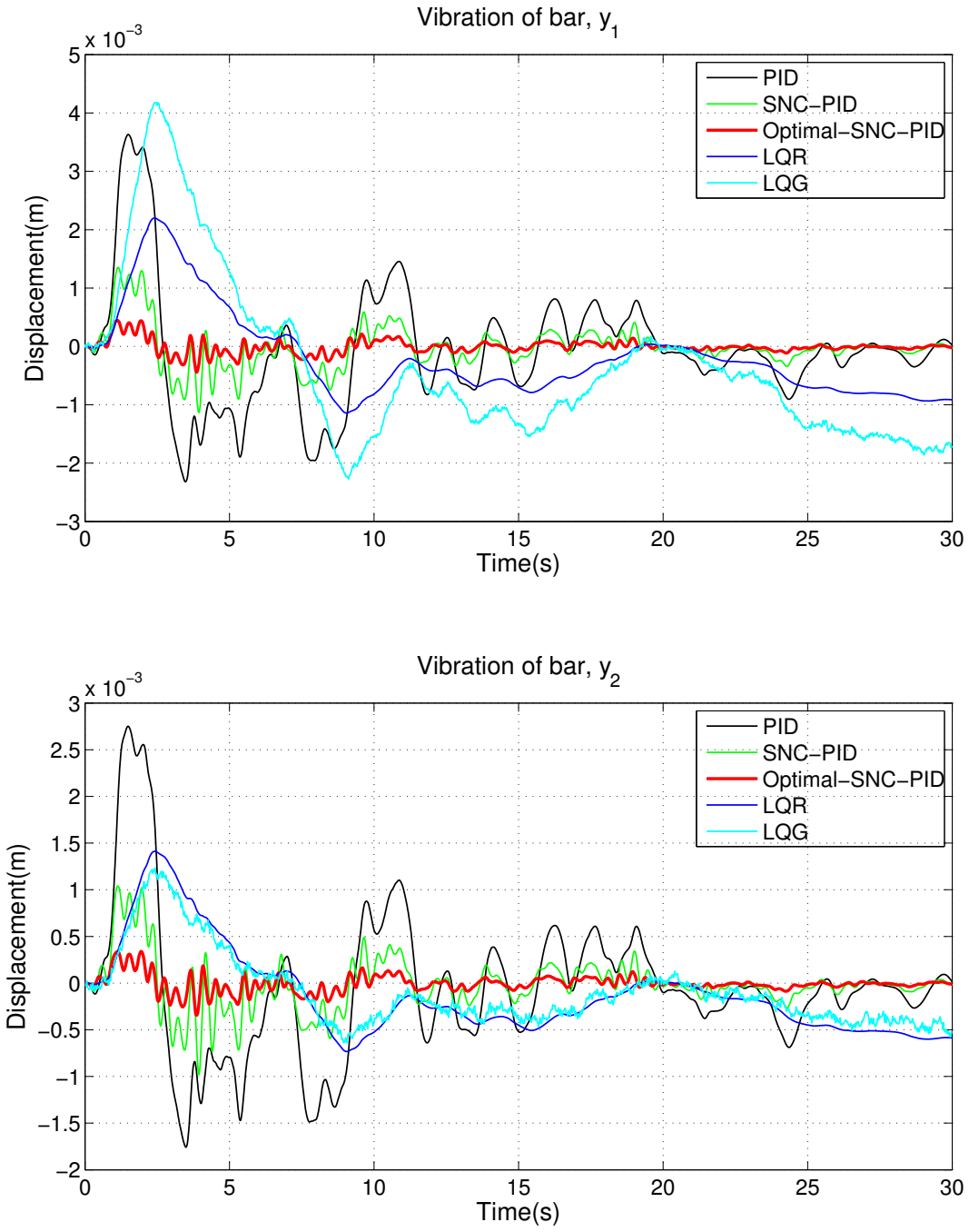

Figure 3.18: Control results of a bar-spring system for PET-UP earthquake

3.4 Three-Degree-of-Freedom Forced Vibration Systems

3.4.1 A Plate-Spring System

A plate-spring system, which could be considered as a base for a mechanical system, is shown in Figure 3.19. The plate is rigid and has a uniformly distributed mass. The system has three degrees of freedom. y_1, y_2, and y_3 are three generalized coordinates of the displacements. The plate is supported by three linear springs and three active dampers. The dampers are controlled by control algorithms. k_1, k_2, and k_3 are the stiffness of the springs, and u_1, u_2, and u_3 are the active forces produced by the active dampers. L_1 and L_2 are the length and width, respectively, of the plate. The system is installed on a base that is allowed to move in the vertical direction. y_0 is the excitation functions, which represents the earthquake data. When the ground starts vibrating, the plate begins moving from its original static equilibrium position. Then, the active forces u_1, u_2, and u_3 start to work, suppress the vibration from the base, and keep the plate near the original equilibrium position.

The plate-spring system is a nonlinear and strongly coupled system. Linearizing the original nonlinear mathematical equations at the equilibrium position, the linearized mathematical model of the system is derived.

$$(\frac{1}{16}+\frac{5}{48}L_1L_2)m\ddot{y}_1+(\frac{1}{16}-\frac{1}{16}L_1L_2)m\ddot{y}_2+(\frac{1}{8}-\frac{1}{24}L_1L_2)m\ddot{y}_3$$
$$+k_1y_1-k_1y_0=u_1 \tag{3.11}$$
$$(\frac{1}{16}-\frac{1}{16}L_1L_2)m\ddot{y}_1+(\frac{1}{16}+\frac{5}{48}L_1L_2)m\ddot{y}_2+(\frac{1}{8}-\frac{1}{24}L_1L_2)m\ddot{y}_3$$
$$+k_2y_2-k_2y_0=u_2 \tag{3.12}$$

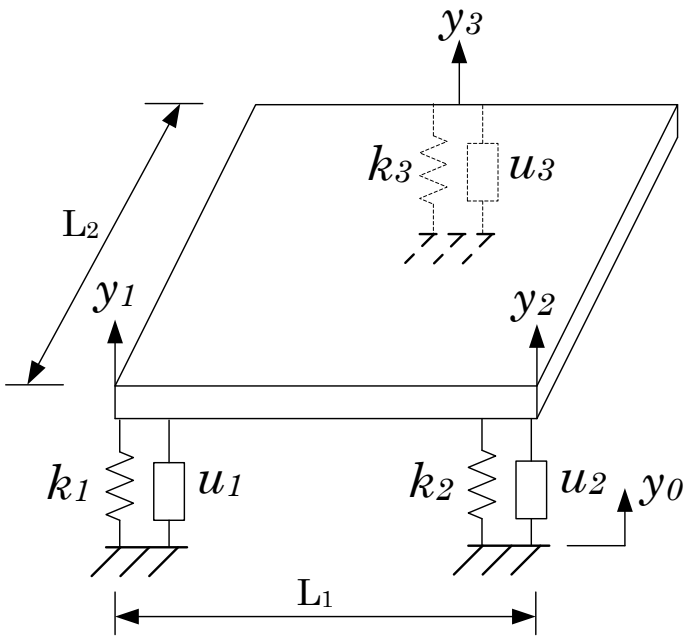

Figure 3.19: A plate-spring system

$$(\frac{1}{8}-\frac{1}{24}L_1L_2)m\ddot{y}_1+(\frac{1}{8}-\frac{1}{24}L_1L_2)m\ddot{y}_2+(\frac{1}{4}+\frac{1}{12}L_1L_2)m\ddot{y}_3$$
$$+k_3y_3-k_3y_0=u_3 \tag{3.13}$$

Set $x_1=y_1$, $x_2=\dot{y}_1$, $x_3=y_2$, $x_4=\dot{y}_2$, $x_5=y_3$, $x_6=\dot{y}_3$, $L_1=1\text{m}$, $L_2=1\text{m}$. The differential equations 3.11, 3.12, and 3.13 are transferred to the state-space equation.

$$\begin{aligned}\dot{\mathbf{x}} &= \mathbf{Ax}+\mathbf{Bu}\\ \mathbf{y} &= \mathbf{Cx}\end{aligned} \tag{3.14}$$

where

$$\mathbf{x} = \begin{pmatrix} x_1 \\ x_2 \\ x_3 \\ x_4 \\ x_5 \\ x_6 \end{pmatrix} = \begin{pmatrix} y_1 \\ \dot{y}_1 \\ y_2 \\ \dot{y}_2 \\ y_3 \\ \dot{y}_3 \end{pmatrix}, \mathbf{y} = \begin{pmatrix} y_1 \\ y_2 \\ y_3 \end{pmatrix}, \mathbf{u} = \begin{pmatrix} y_0 \\ u_1 \\ u_2 \\ u_3 \end{pmatrix},$$

$$\mathbf{A} = \begin{pmatrix} 0 & 1 & 0 & 0 & 0 & 0 \\ -\frac{-7k_1}{m} & 0 & -\frac{k_2}{m} & 0 & \frac{2k_3}{m} & 0 \\ 0 & 0 & 0 & 1 & 0 & 0 \\ -\frac{k_1}{m} & 0 & -\frac{7k_2}{m} & 0 & \frac{2k_3}{m} & 0 \\ 0 & 0 & 0 & 0 & 0 & 1 \\ \frac{2k_1}{m} & 0 & \frac{2k_2}{m} & 0 & -\frac{4k_3}{m} & 0 \end{pmatrix},$$

$$\mathbf{B} = \begin{pmatrix} 0 & 0 & 0 & 0 \\ \frac{7k_1 + k_2 - 2k_3}{m} & \frac{7}{m} & \frac{1}{m} & \frac{2}{m} \\ 0 & 0 & 0 & 0 \\ \frac{k_1 + 7k_2 - 2k_3}{m} & \frac{1}{m} & \frac{7}{m} & -\frac{2}{m} \\ 0 & 0 & 0 & 0 \\ \frac{-2k_1 - 2k_2 + 4k_3}{m} & -\frac{2}{m} & -\frac{2}{m} & \frac{4}{m} \end{pmatrix},$$

$$\mathbf{C} = \begin{pmatrix} 1 & 0 & 0 & 0 & 0 & 0 \\ 0 & 0 & 1 & 0 & 0 & 0 \\ 0 & 0 & 0 & 0 & 1 & 0 \end{pmatrix}.$$

The parameters of the system are $m = 10\text{kg}$, $k_1 = 40\text{N/m}$, $k_2 = 35\text{N/m}$, $k_3 = 45\text{N/m}$, $L_1 = 1\text{m}$, and $L_2 = 1\text{m}$. The control parameters of the control algorithms of Chapter 2 are listed in the following:

PID: for u_1, $K_p = 240$, $T_i = 0.9$, $T_d = 0.2$,

for u_2, $K_p = 240$, $T_i = 0.9$, $T_d = 0.2$.

for u_3, $K_p = 240$, $T_i = 0.9$, $T_d = 0.2$.

SNC-PID: for u_1, $w_1 = 400$, $w_2 = 350$, $w_3 = 20$, $K_1 = 80$, $d_1 = 150$,

for u_2, $w_1 = 400$, $w_2 = 350$, $w_3 = 20$, $K_2 = 80$, $d_2 = 150$,

for u_3, $w_1 = 400$, $w_2 = 350$, $w_3 = 20$, $K_3 = 120$, $d_3 = 150$.

LQR:

$$\mathbf{K} = \begin{pmatrix} 0 & 0 & 0 & 0 & 0 & 0 \\ 602.9020 & 39.1957 & -53.8259 & -7.6037 & -236.3250 & -19.5835 \\ 27.1886 & 0.7428 & 663.3133 & 46.5408 & 61.3735 & 13.1725 \\ 249.4749 & 17.5677 & 9.6326 & 8.4783 & 675.0922 & 57.9392 \end{pmatrix}.$$

LQG:

$$\mathbf{K} = \begin{pmatrix} 0 & 0 & 0 & 0 & 0 & 0 \\ 602.9020 & 39.1957 & -53.8259 & -7.6037 & -236.3250 & -19.5835 \\ 27.1886 & 0.7428 & 663.3133 & 46.5408 & 61.3735 & 13.1725 \\ 249.4749 & 17.5677 & 9.6326 & 8.4783 & 675.0922 & 57.9392 \end{pmatrix}.$$

The results using the different control algorithms are shown in Figures 3.20-3.23. The curves in the top graph of Figure 3.20 are the displacements of y_1, the curves in the middle graph are the displacements of y_2, and the curves in the bottom graph are the displacements of y_3. The magenta curve is the El-Centro earthquake data. The orange lines are the displacements of y_1, y_2, and y_3 without control algorithms applied. It is clear that all of the control algorithms worked quiet well. They suppressed all of y_1, y_2, and y_3 considerably. In order to compare the control algorithms, the control results are shown in Figure 3.21.

It can be seen from Figure 3.21 that the Optimal-SNC-PID is the best control algorithm because the displacements of y_1, y_2, and y_3 corresponding to the Optimal-SNC-PID are the smallest among all of the control results. However, for y_1 and y_2, the Optimal-SNC-PID is only slightly better than the SNC-PID algorithm. For y_3, the results of the Optimal-SNC-PID and the SNC-PID are similar.

The databases for the Optimal-SNC-PID are based on the control forces corresponding to the El-Centro earthquake data. In order to validate the algorithm, other earthquake data are applied to the system. The control results for the PET-UP earthquake data are shown in Figure 3.22 and 3.23, respectively. The results show

that the Optimal-SNC-PID has the same characteristics as before, when its performance was the best among all of the control algorithms for y_1 and y_2; it yields a result similar to that of SNC-PID for y_3. There are 2,500 points in the kd-tree data structure.

3.4.2 A Three-Link Planar Robotic Arm

Few people have studied robot vibration caused by ground motion. Tahboub [41] studied a mobile manipulator with moving bases. He used a linearized model for the robot, 3 DOF PUMA 560, where only two degrees of freedom were used in the simulation, and he built an estimator to find the nonlinear items. The base force and/or base motion were thought of as unknown external disturbances. However, Tahboub did not achieve good results for tracking the errors and encounted divergence issues with the errors when the base was bumpy. Bucklaew et al. [42] studied a two links PD-controlled robotic system with only horizontal base motion and found the bifurcation steady-state errors of joints' angles. Wu et al. [43] used the Lyapunov control algorithm to stabilize a two-link planar manipulator with a non-fixed base, whose motions are since functions in both the horizontal and vertical directions. The system with control was almost stabilized after 5 seconds from the starting time of the motion.

In this work, we introduce a three-link planar non-fixed-base robotic arm (Figure 3.24) as another challenging system for testing the effectiveness of the proposed Optimal-SNC/Optimal-SNC-PID control algorithm. The links are rigid with uni-

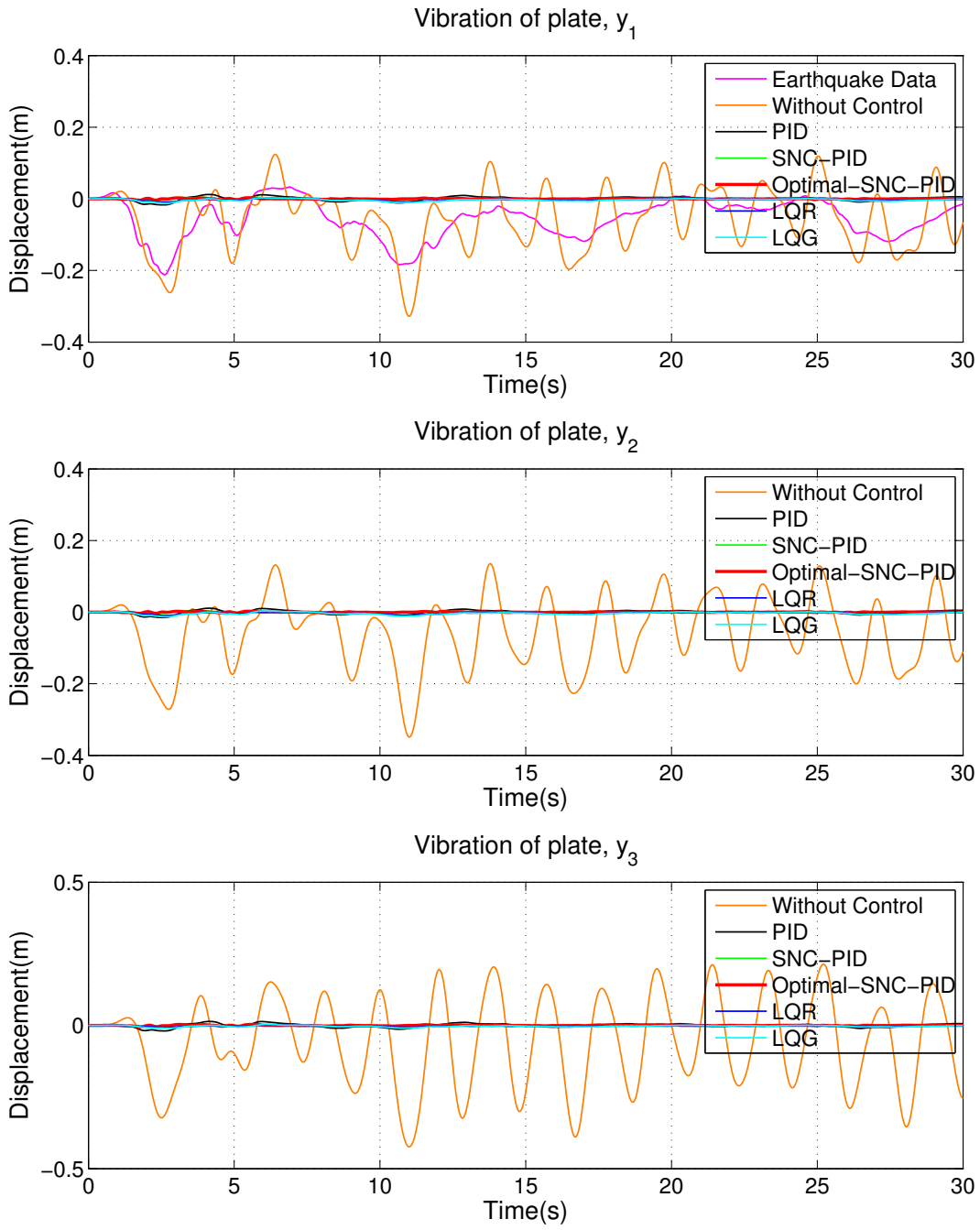

Figure 3.20: Results with control and without control

of a plate system for El-Centro earthquake

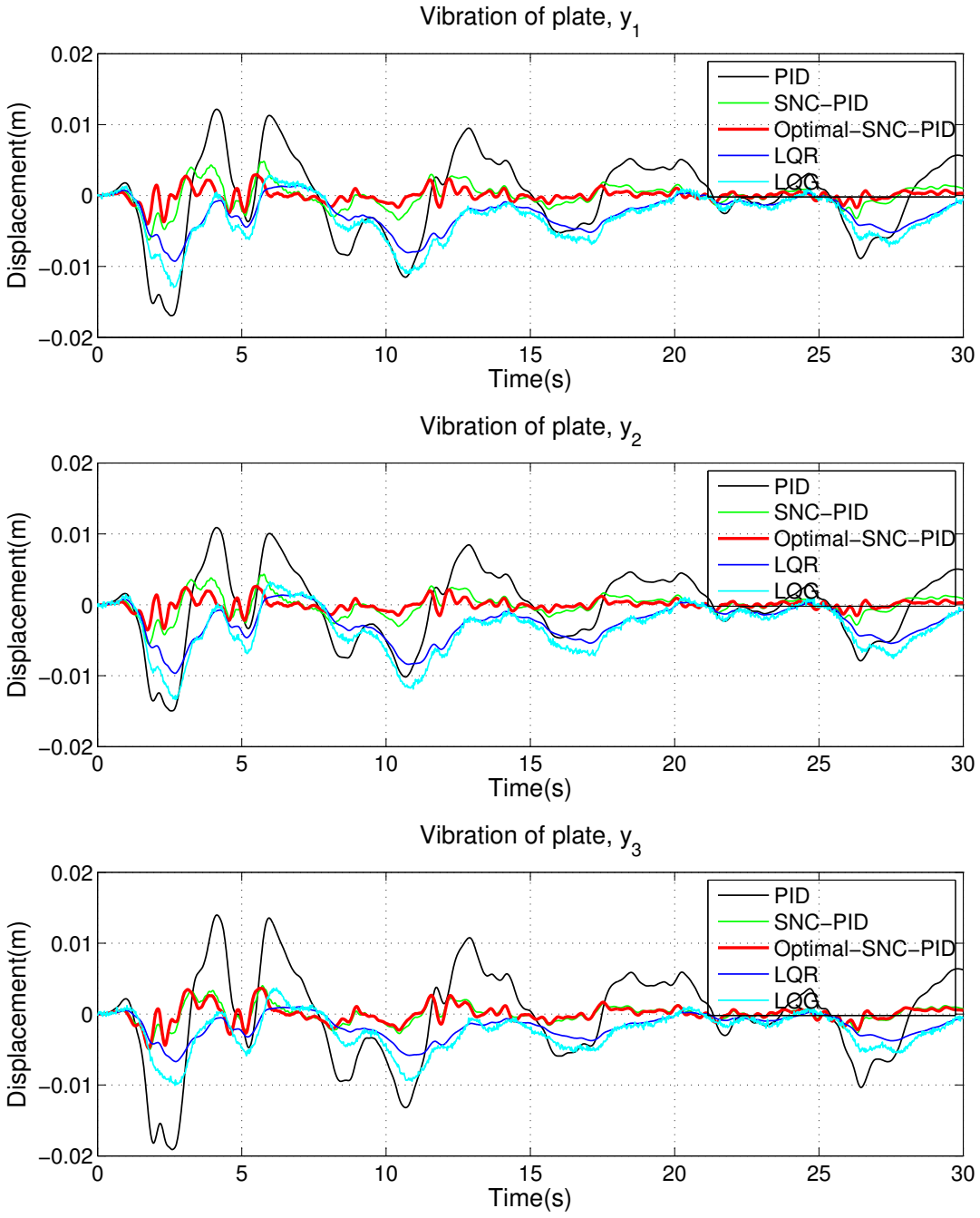

Figure 3.21: Control results of a plate system for El-Centro earthquake

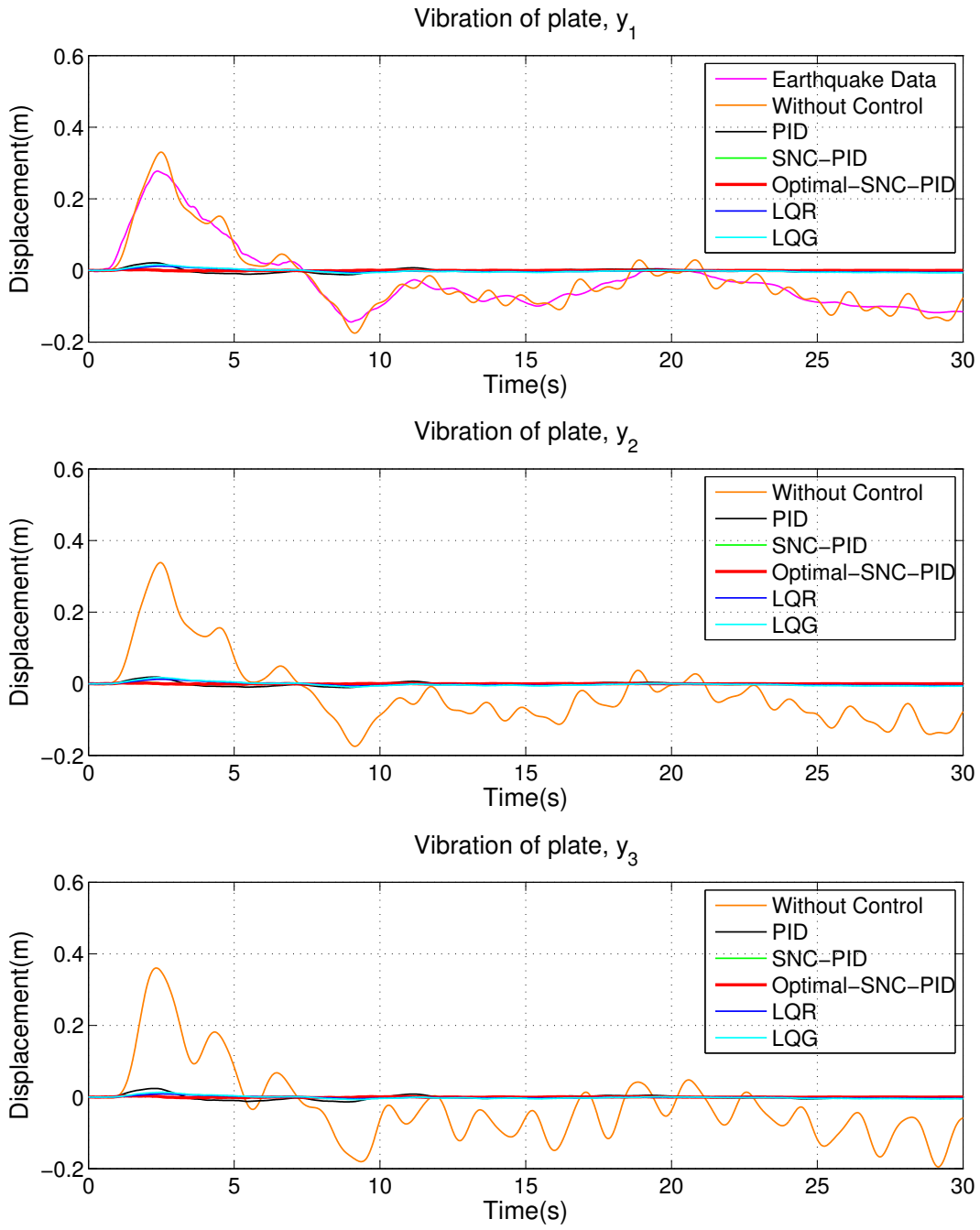

Figure 3.22: Results with control and without control

of a plate system for PET-UP earthquake

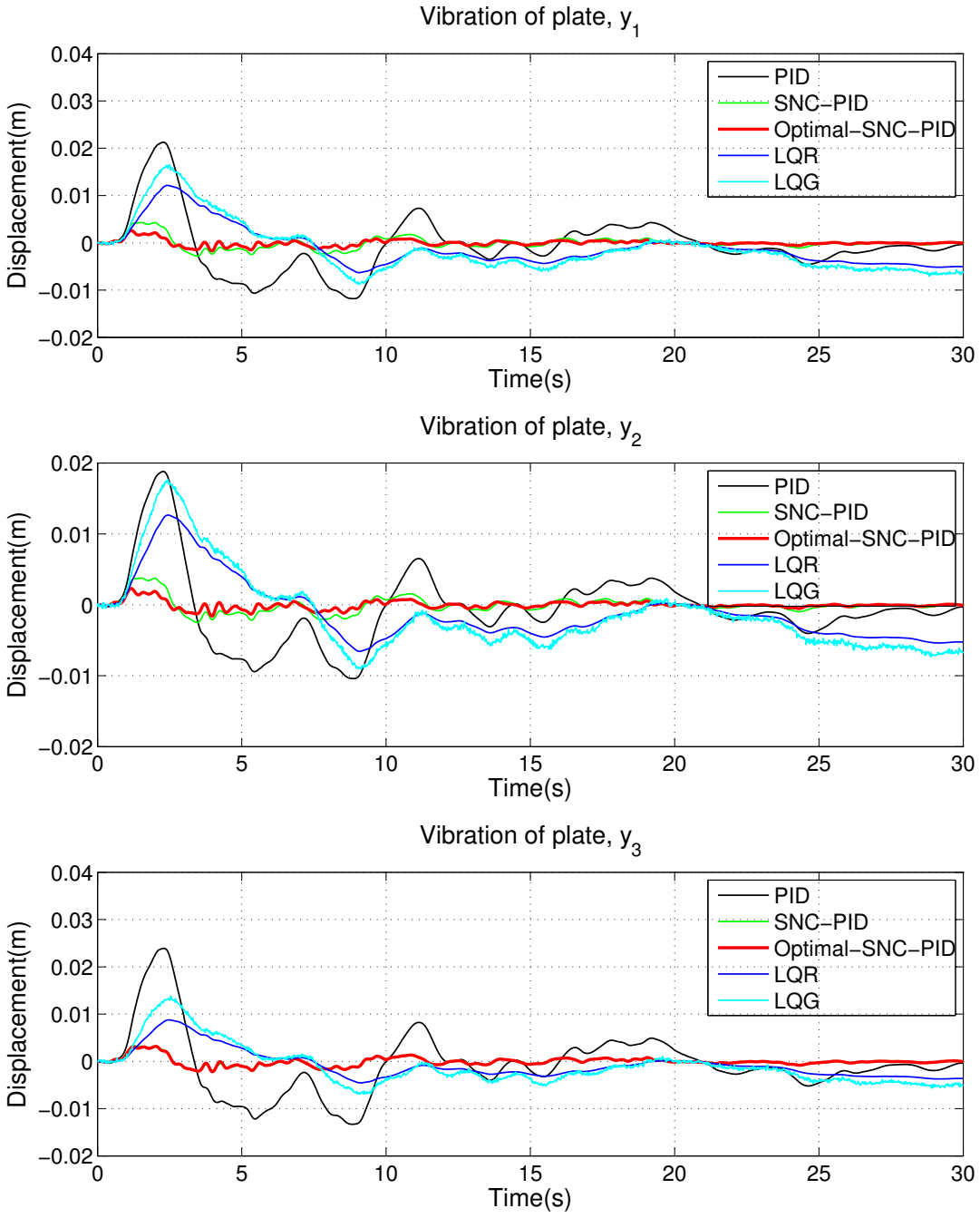

Figure 3.23: Control results of a plate system for PET-UP earthquake

formly distributed masses and rotate around the joints. Link 1 has length L_1 and mass m_1, Link 2 has length L_2 and mass m_2, and link 3 has length L_3 and mass m_3. θ_1, θ_2, θ_3 are the relative angular displacements of each link. x_i and y_i, $i = 1, \ldots, 3$, are the coordinates of the end of each link. l_i is the length between the center of mass at the link i and the joint $i - 1$. There is an active damper at each joint to produce rotational torques τ_1, τ_2, and τ_3.

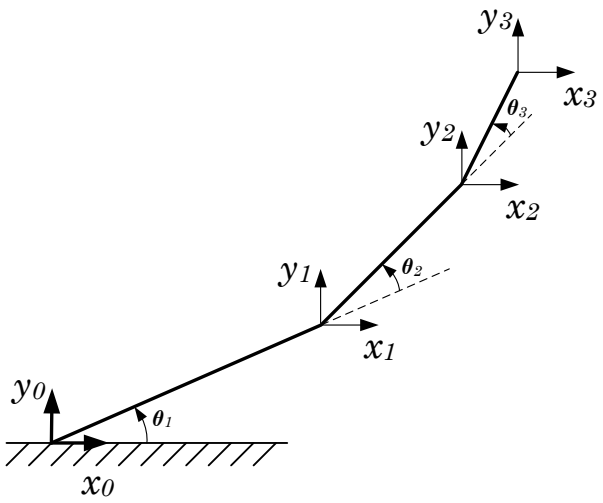

Figure 3.24: A three-link planar system

The system is supported on a base that is allowed to move in the horizontal and vertical directions. x_0 and y_0 are the excitation functions, which are earthquake data. When the ground starts vibrating, the system begins moving from its original static equilibrium position. Then, the active forces τ_1, τ_2, and τ_3 start to work and

keep link 3 at the original static position. That is, it is not only applied to the end effector x_3 and y_3, but also to x_2 and y_2, which keeps the position and orientation of the link 3 unchanged during the dynamic process.

The system is a nonlinear coupled system. Since θ_1, θ_2, and θ_3 rotate in a large scale during the dynamic process, the system cannot be linearized. Therefore, the original nonlinear mathematical model is used in the simulation. The differential equations are as following:

$$
\begin{aligned}
&\left(m_1 l_1^2 + \frac{1}{12} m_1 L_1^2 + m_2 L_1^2 + m_2 l_2^2 + 2 m_2 L_1 l_2 cos\theta_2 + \frac{1}{12} m_2 L_2^2 + m_3 L_1^2 + m_3 L_2^2 \right. \\
&\left. + m_3 l_3^2 + 2 m_3 L_1 L_2 cos\theta_2 + 2 m_3 L_1 l_3 cos(\theta_2 + \theta_3) + 2 m_3 L_2 l_3 cos\theta_3 + \frac{1}{12} m_3 L_3^2 \right) \ddot{\theta}_1 \\
&+ \left(m_2 l_2^2 + m_2 L_1 l_2 cos\theta_2 + \frac{1}{12} m_2 L_2^2 + m_3 L_2^2 + m_3 l_3^2 + m_3 L_1 L_2 cos\theta_2 \right. \\
&\left. + m_3 L_1 l_3 cos(\theta_2 + \theta_3) + 2 m_3 L_2 l_3 cos\theta_3 + \frac{1}{12} m_3 L_3^2 \right) \ddot{\theta}_2 \\
&+ \left(m_3 l_3^2 + m_3 L_1 l_3 cos(\theta_2 + \theta_3) + m_3 L_2 l_3 cos\theta_3 + \frac{1}{12} m_3 L_3^2 \right) \ddot{\theta}_3 \\
&+ (-2 m_2 L_1 l_2 sin\theta_2 - 2 m_3 L_1 L_2 sin\theta_2 - 2 m_3 L_1 l_3 sin(\theta_2 + \theta_3)) \dot{\theta}_1 \dot{\theta}_2 \\
&+ (-2 m_3 L_1 l_3 sin(\theta_2 + \theta_3) - 2 m_3 L_2 l_3 sin\theta_3) \dot{\theta}_1 \dot{\theta}_3 \\
&+ (-2 m_3 L_1 l_3 sin(\theta_2 + \theta_3) - 2 m_3 L_2 l_3 sin\theta_3) \dot{\theta}_2 \dot{\theta}_3 \\
&+ (-m_2 L_1 l_2 sin\theta_2 - m_3 L_1 L_2 sin\theta_2 - m_3 L_1 l_3 sin(\theta_2 + \theta_3)) \dot{\theta}_2^2 \\
&+ (-m_3 L_1 l_3 sin(\theta_2 + \theta_3) - m_3 L_2 l_3 sin\theta_3) \dot{\theta}_3^2 \\
&+ (-m_1 l_1 sin\theta_1 - m_2 L_1 sin\theta_1 - m_2 l_2 sin(\theta_1 + \theta_2) - m_3 L_1 sin\theta_1 \\
&- m_3 L_2 sin(\theta_1 + \theta_2) - m_3 l_3 sin(\theta_1 + \theta_2 + \theta_3)) \ddot{x}_0 \\
&+ (m_1 l_1 cos\theta_1 + m_2 L_1 cos\theta_1 + m_2 l_2 cos(\theta_1 + \theta_2) + m_3 L_1 cos\theta_1
\end{aligned}
$$

$$+m_3L_2cos(\theta_1+\theta_2)+m_3l_3cos(\theta_1+\theta_2+\theta_3))\ddot{y}_0$$

$$+m_1gl_1cos\theta_1+m_2gL_1cos\theta_1+m_2gl_2cos(\theta_1+\theta_2)$$

$$+m_3gL_1cos\theta_1+m_3gL_2cos(\theta_1+\theta_2)+m_3gl_3cos(\theta_1+\theta_2+\theta_3)$$

$$=\tau_1 \tag{3.15}$$

$$\left(m_2l_2^2+m_2L_1l_2cos\theta_2+\frac{1}{12}m_2L_2^2+m_3L_2^2+m_3l_3^2+m_3L_1L_2cos\theta_2\right.$$
$$\left.+m_3L_1l_3cos(\theta_2+\theta_3)+2m_3L_2l_3cos\theta_3+\frac{1}{12}m_3L_3^2\right)\ddot{\theta}_1$$
$$+\left(m_2l_2^2+\frac{1}{12}m_2L_2^2+m_3L_2^2+m_3l_3^2+2m_3L_2l_3cos\theta_3+\frac{1}{12}m_3L_3^2\right)\ddot{\theta}_2$$
$$+\left(m_3l_3^2+m_3L_2l_3cos\theta_3+\frac{1}{12}m_3L_3^2\right)\ddot{\theta}_3$$
$$-2m_3L_2l_3sin\theta_3\dot{\theta}_1\dot{\theta}_3-2m_3L_2l_3sin\theta_3\dot{\theta}_2\dot{\theta}_3$$
$$+(m_2L_1l_2sin\theta_2+m_3L_1L_2sin\theta_2+m_3L_1l_3sin(\theta_2+\theta_3))\dot{\theta}_1^2-m_3L_2l_3sin\theta_3\dot{\theta}_3^2$$
$$+(-m_2l_2sin(\theta_1+\theta_2)-m_3L_2sin(\theta_1+\theta_2)-m_3l_3sin(\theta_1+\theta_2+\theta_3))\ddot{x}_0$$
$$+(m_2l_2cos(\theta_1+\theta_2)+m_3L_2cos(\theta_1+\theta_2)+m_3l_3cos(\theta_1+\theta_2+\theta_3))\ddot{y}_0$$
$$+m_2gl_2cos(\theta_1+\theta_2)+m_3gL_2cos(\theta_1+\theta_2)+m_3gl_3cos(\theta_1+\theta_2+\theta_3)$$
$$=\tau_2 \tag{3.16}$$

$$\left(m_3l_3^2+m_3L_1l_3cos(\theta_2+\theta_3)+m_3L_2l_3cos\theta_3+\frac{1}{12}m_3L_3^2\right)\ddot{\theta}_1$$
$$+\left(m_3l_3^2+m_3L_2l_3cos\theta_3+\frac{1}{12}m_3L_3^2\right)\ddot{\theta}_2+\left(m_3l_3^2+\frac{1}{12}m_3L_3^2\right)\ddot{\theta}_3$$
$$+\left(m_3L_1l_3sin(\theta_2+\theta_3)+m_3L_2l_3sin\theta_3\right)\dot{\theta}_1^2+m_3L_2l_3sin\theta_3\dot{\theta}_2^2$$
$$+2m_3L_2l_3sin\theta_3\dot{\theta}_1\dot{\theta}_2+m_3gl_3cos(\theta_1+\theta_2+\theta_3)$$
$$-m_3l_3sin(\theta_1+\theta_2+\theta_3)\ddot{x}_0+m_3l_3cos(\theta_1+\theta_2+\theta_3)\ddot{y}_0$$

$$= \tau_3 \tag{3.17}$$

The Denavit-Hartenberg (D-H) convention [44] was used in analyzing the system kinematics. The parameters of the three-link system in the D-H representation are shown in Table 3.1. The four parameters θ_i, d_i, a_i, and α_i are the joint angle, link offset, link length, and link twist, respectively.

Table 3.1: DH parameters for the three-link system

Link	θ_i	d_i	a_i	α_i
1	θ_1	0	L_1	0
2	θ_2	0	L_2	0
3	θ_3	0	L_3	0

Therefore, the transformation matrices are constructed as shown in the following.

$$A_{01} = \begin{pmatrix} cos\theta_1 & -sin\theta_1 & 0 & L_1 cos\theta_1 \\ sin\theta_1 & cos\theta_1 & 0 & L_1 sin\theta_1 \\ 0 & 0 & 1 & 0 \\ 0 & 0 & 0 & 1 \end{pmatrix} \tag{3.18}$$

$$A_{12} = \begin{pmatrix} cos\theta_2 & -sin\theta_2 & 0 & L_2 cos\theta_2 \\ sin\theta_2 & cos\theta_2 & 0 & L_2 sin\theta_2 \\ 0 & 0 & 2 & 0 \\ 0 & 0 & 0 & 1 \end{pmatrix} \tag{3.19}$$

$$A_{23} = \begin{pmatrix} cos\theta_3 & -sin\theta_3 & 0 & L_3 cos\theta_3 \\ sin\theta_3 & cos\theta_3 & 0 & L_3 sin\theta_3 \\ 0 & 0 & 1 & 0 \\ 0 & 0 & 0 & 1 \end{pmatrix} \tag{3.20}$$

The links matrices are:

$$T_1 = A_{01} \tag{3.21}$$

$$T_2 = A_{01} A_{12} \tag{3.22}$$

$$T_3 = A_{01} A_{12} A_{23} \tag{3.23}$$

Thus, the coordinates of the links' ends x_i and y_i are

$$\begin{pmatrix} x_i \\ y_i \\ 0 \\ 1 \end{pmatrix} = T_i \begin{pmatrix} 0 \\ 0 \\ 0 \\ 1 \end{pmatrix} + \begin{pmatrix} x_0 \\ y_0 \\ 0 \\ 0 \end{pmatrix} \tag{3.24}$$

where $i = 1, \ldots, 3$.

Inverse kinematics is also used in the simulation in order to calculate the reference joint angles at each step [45]. Since the control goal is to keep link 3 at

the original static position, only link 1 end's coordinates x_1 and y_1 are needed to be calculated. In Figure 3.25, there are two coordinate systems. x and y represent the global coordinate system, whose origin point o is at the beginning static position of x_0 and y_0. x' and y' represent the current local coordinate system. x_0 and y_0 are the current horizontal and vertical displacements of the base from the current local coordinate system to the global coordinate system.

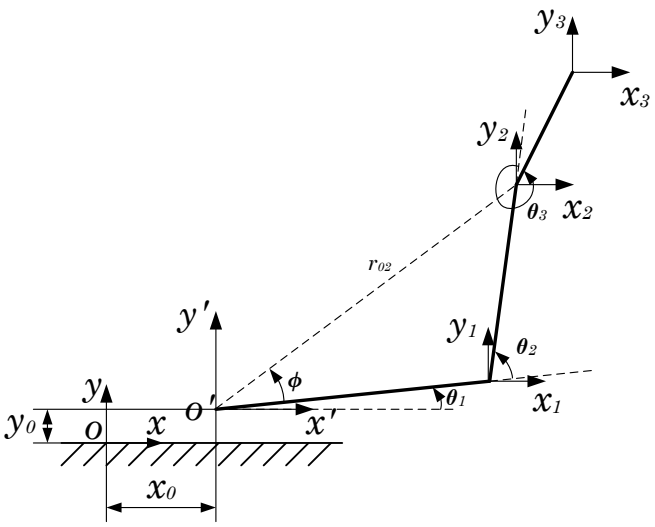

Figure 3.25: Inverse kinematics for the three-links system

First, θ_2 is decided,

$$\theta_2 = arccos\left(\frac{r_{02}^2 - L_1^2 - L_2^2}{2L_1L_2}\right) \tag{3.25}$$

where r_{02} is the distance between point o$'$ and point (x_2, y_2).

Then,

$$tg\phi = \frac{L_2 sin\theta_2}{L_1 + L_2 cos\theta_2}$$
$$\theta_1 = arctan\left(\frac{y_2}{x_2}\right) - \phi \tag{3.26}$$

Finally,

$$\theta_3 = \pi + arccos\left(\frac{r_{13}^2 - L_3^2 - L_2^2}{2L_2L_3}\right) \tag{3.27}$$

where r_{13} is the distance between point (x_1, y_1) and point (x_3, y_3). x_i and y_i are the coordinates at the current local coordinate system.

The parameters of the manipulator are $m_1 = 15$kg, $L_1 = 1$m, $m_2 = 10$kg, $L_2 = 0.6$m, $m_3 = 5$kg, $L_3 = 0.4$m. The initial angular displacements are $\theta_{10} = \theta_{20} = \theta_{30} = \pi/9$.

Since the system is nonlinear, LQR and LQG can not be applied to the system. Thus, only PD, SNC, and Optimal-SNC are used. For SNC and Optimal-SNC, four neuron inputs are used, which are the reference angular displacements, reference angular velocities, angular displacements error, and the change of the angular displacements error, as described in item 2 on page 20. The control parameters of the control algorithms under investigation are listed in the following.

PD: for u_1, $K_p = 0.4$, $T_d = 80$,

for u_2, $K_p = 0.4$, $T_d = 80$.

for u_3, $K_p = 0.4$, $T_d = 80$.

SNC: for u_1, $w_1 = 0.001$, $w_2 = 0.01$, $w_3 = 300$, $w_4 = 100$, $K_1 = 350$, $d_1 = 1.5$,

for u_2, $w_1 = 0.001$, $w_2 = 0.01$, $w_3 = 300$, $w_4 = 100$, $K_2 = 350$, $d_2 = 1.5$,

for u_3, $w_1 = 0.001$, $w_2 = 0.01$, $w_3 = 300$, $w_4 = 100$, $K_3 = 350$, $d_3 = 1.5$.

x_0 and y_0 are the same earthquake data with different scale factors for the original data. Figure 3.26 shows the displacements and accelerations of the scaled El-Centro earthquake data. Figure 3.28 shows the displacements and accelerations of the scaled PET-UP earthquake data.

The manipulator is an extremely sensitive system. If no control is applied to the system, then the system becomes unstable as the base moves. The results of the manipulator motion for the scaled El-Centro earthquake data with control are shown in Figure 3.27. All of the control algorithms work well. The displacements of the joint 2 and the end effector are less than 1mm. The Optimal-SNC shows a little bit better results than those of SNC, especially for the y coordinate of the end effector.

The database for the Optimal-SNC was based on the control torques corresponding to the scaled El-Centro earthquake data. In order to validate the algorithm, the scaled PET-UP earthquake data as x_0 and y_0 are applied to the system. The control results are shown in Figure 3.29. The results show that the Optimal-SNC is still the best algorithm among the algorithms under investigation. There are 2,500 points in the kd-tree data structure.

In order to check effectiveness of the proposed Optimal-SNC under more critical situations, a different initial condition of the manipulator is used. This means that the algorithm will be tested under different starting conditions than those used in building the database. Now, $\theta_{10} = \pi/3$, $\theta_{20} = \pi/3$, and $\theta_{30} = \pi/4$. x_0 and y_0 are the scaled PET-UP earthquake data. The results show that the Optimal-SNC

still works well when the displacements of joints 2 and the end effector are less than 0.7mm.

3.5 Discussion

A novel active control algorithm called Optimal-SNC/Optimal-SNC-PID is introduced in this work to suppress and control the vibration transmitted to mechanical and robotic systems. The proposed method is developed by modifying a current single neuron controller (SNC) using a parameters-updating optimization algorithm with a novel objective function. The proposed method is then integrated within a data search algorithm, kd-tree. The proposed method, called Optimal-SNC/Optimal-SNC-PID, has been tested on several mechanical systems under vertical base vibration and on a planar three-degree-of-freedom robotic arm under combined vertical and horizontal random base vibration. When compared with the current state-of-the-art control algorithms such as PID, LQR, and LQG, the proposed algorithm of this work was the best in terms of real-time capability and accuracy. Therefore, the proposed algorithm will have significant impact on the current state of structural and mechanical systems control. For robotic applications, the proposed method was very stable and effective in increasing the accuracy of the end-effector of a robotic arm under severe ground vibration. The latter will have significant value, for example, in stabilizing monitoring equipment and controlling surgical robotics in medical transportation vehicles. Additionally, the proposed control method showed stability and effectiveness even when used on robotic systems with different initial conditions.

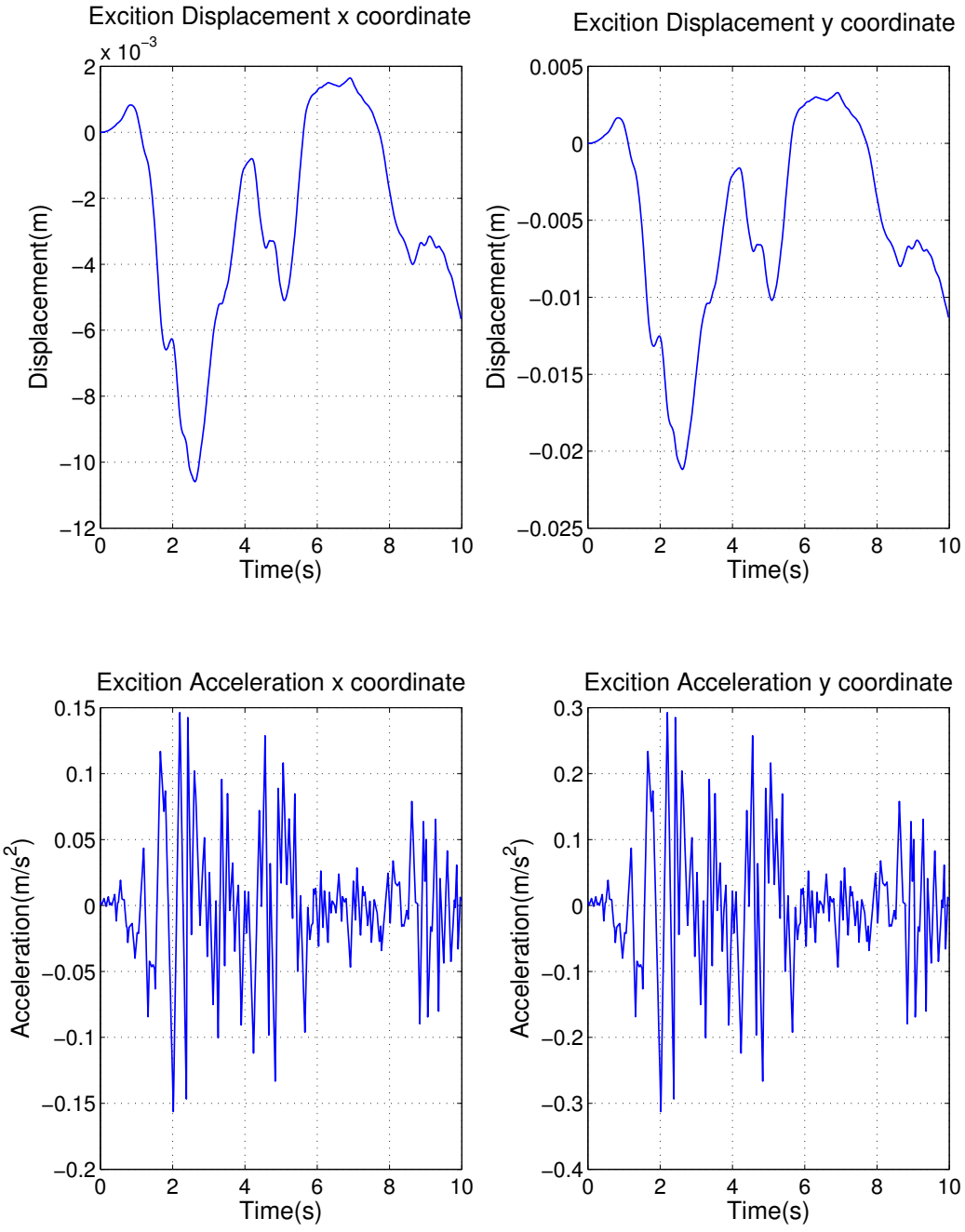

Figure 3.26: Displacement and acceleration of El-Centro earthquake

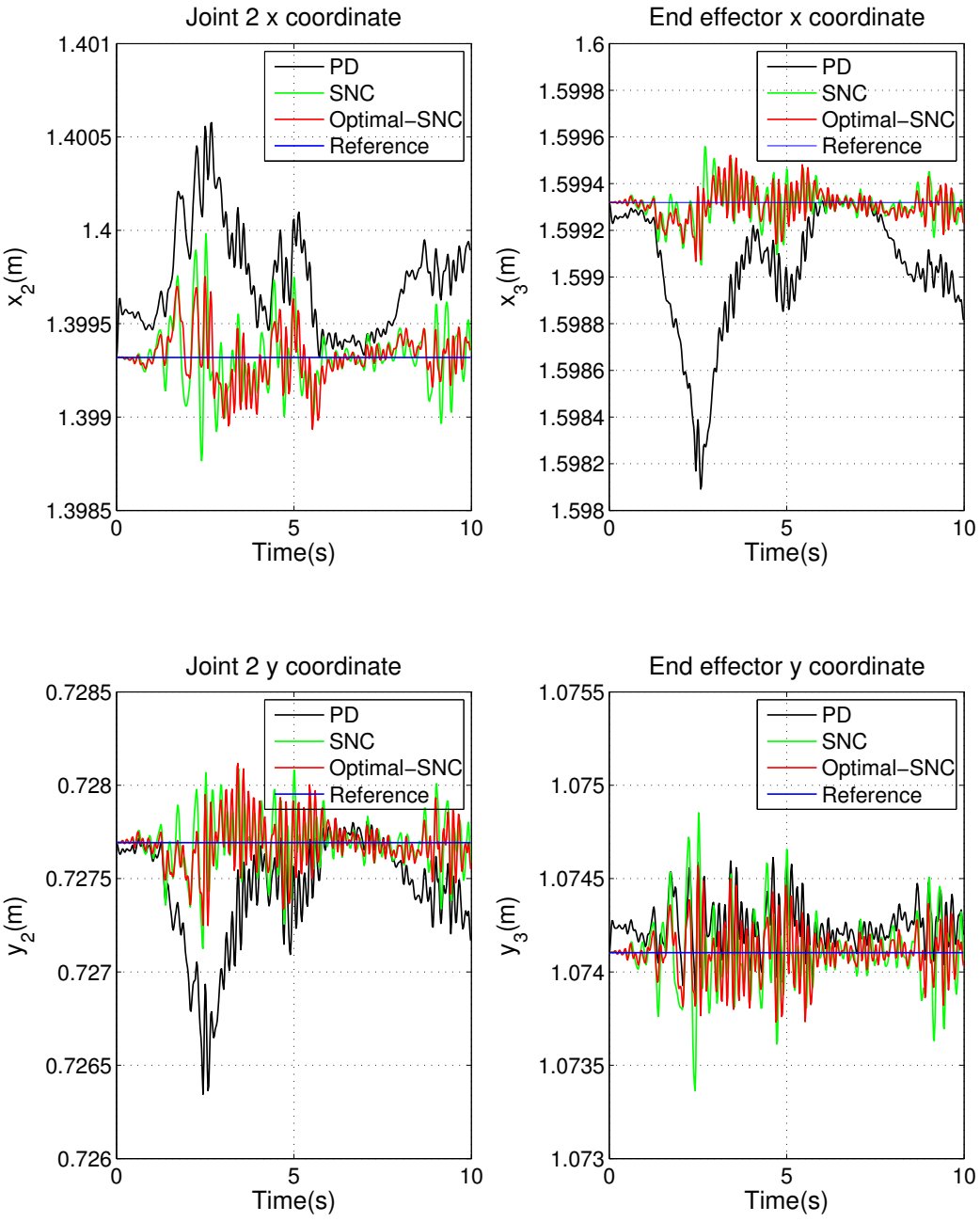

Figure 3.27: Manipulator's displacements for El-Centro earthquake

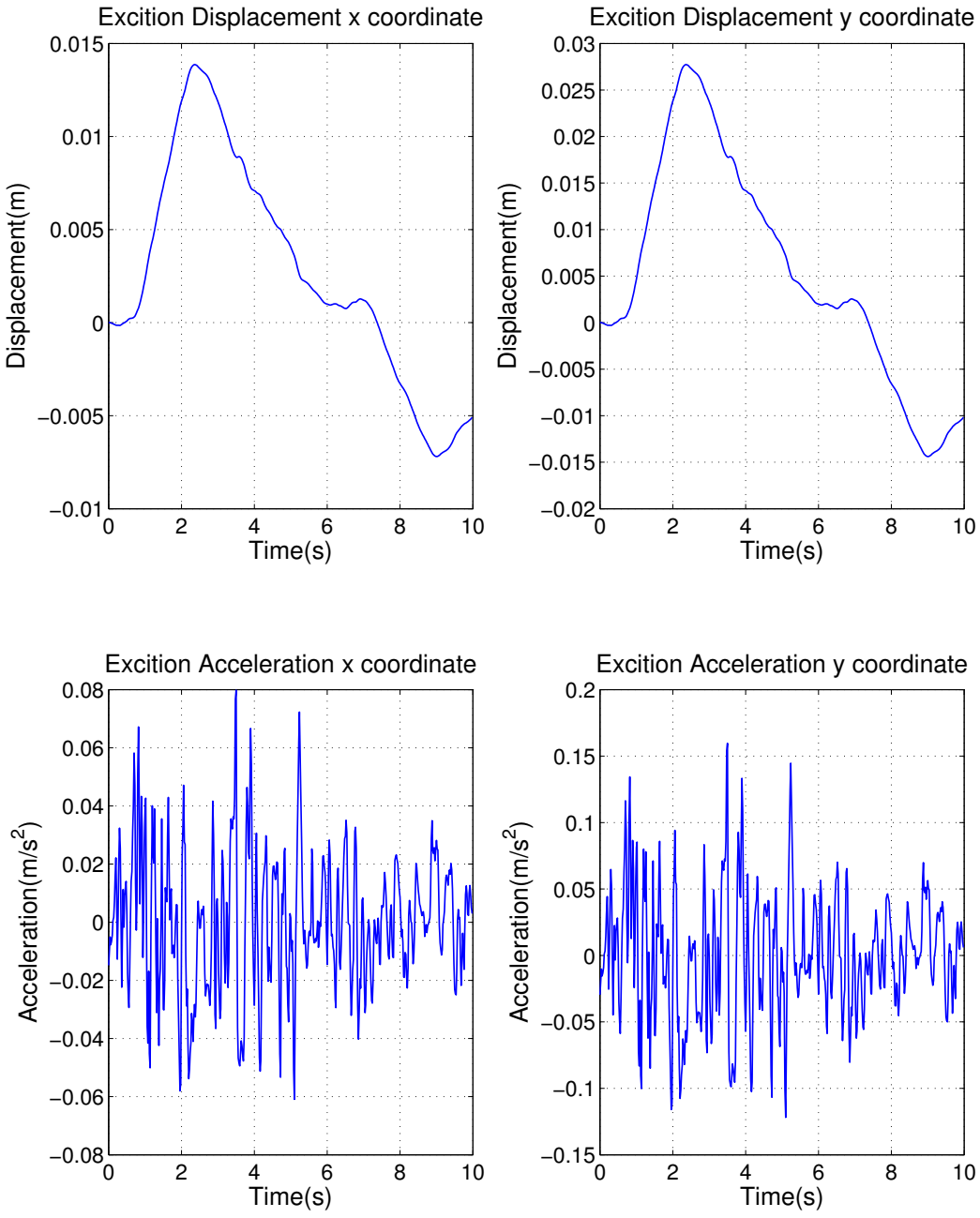

Figure 3.28: Displacement and acceleration of PET-UP earthquake

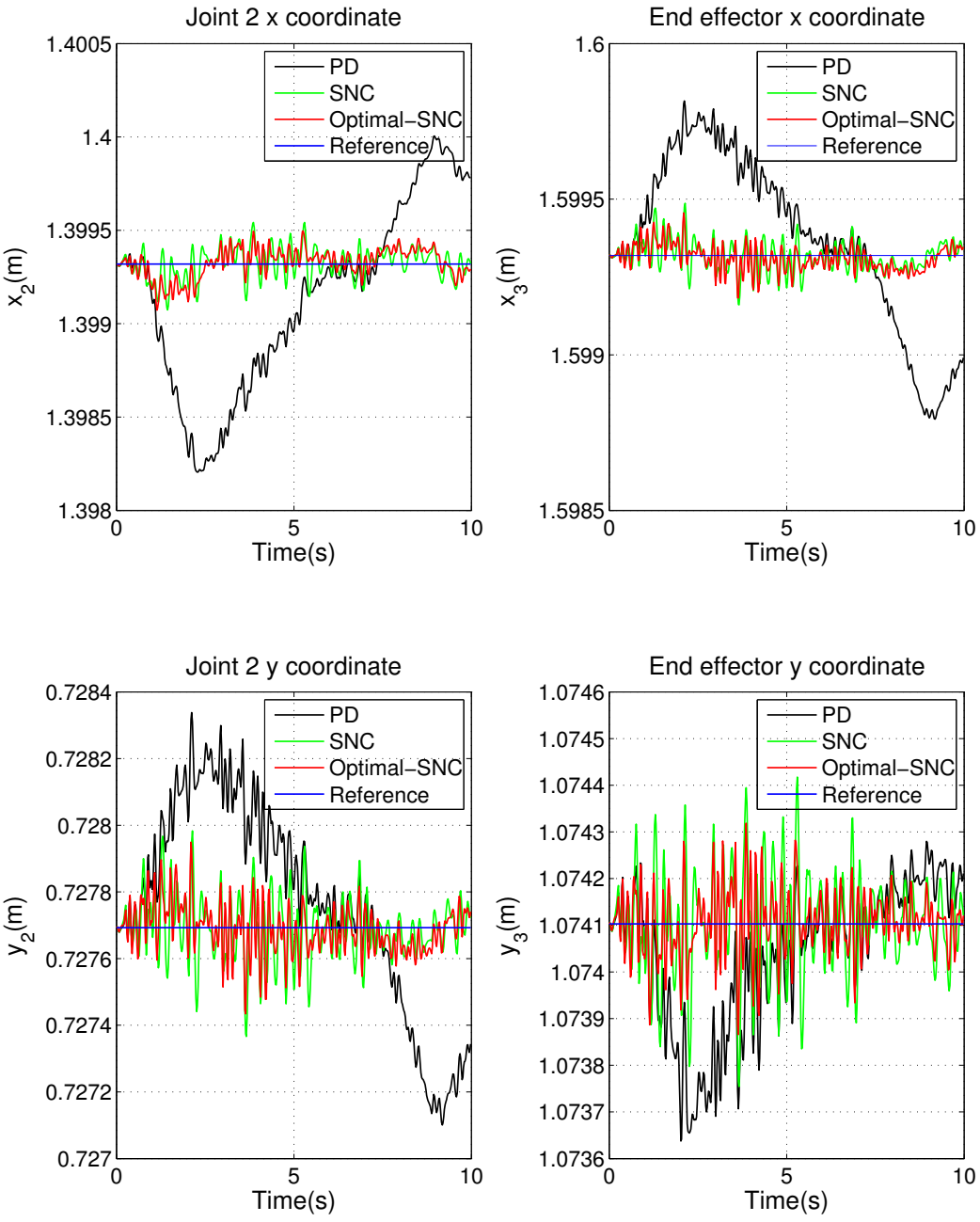

Figure 3.29: Manipulator's displacements for PET-UP earthquake

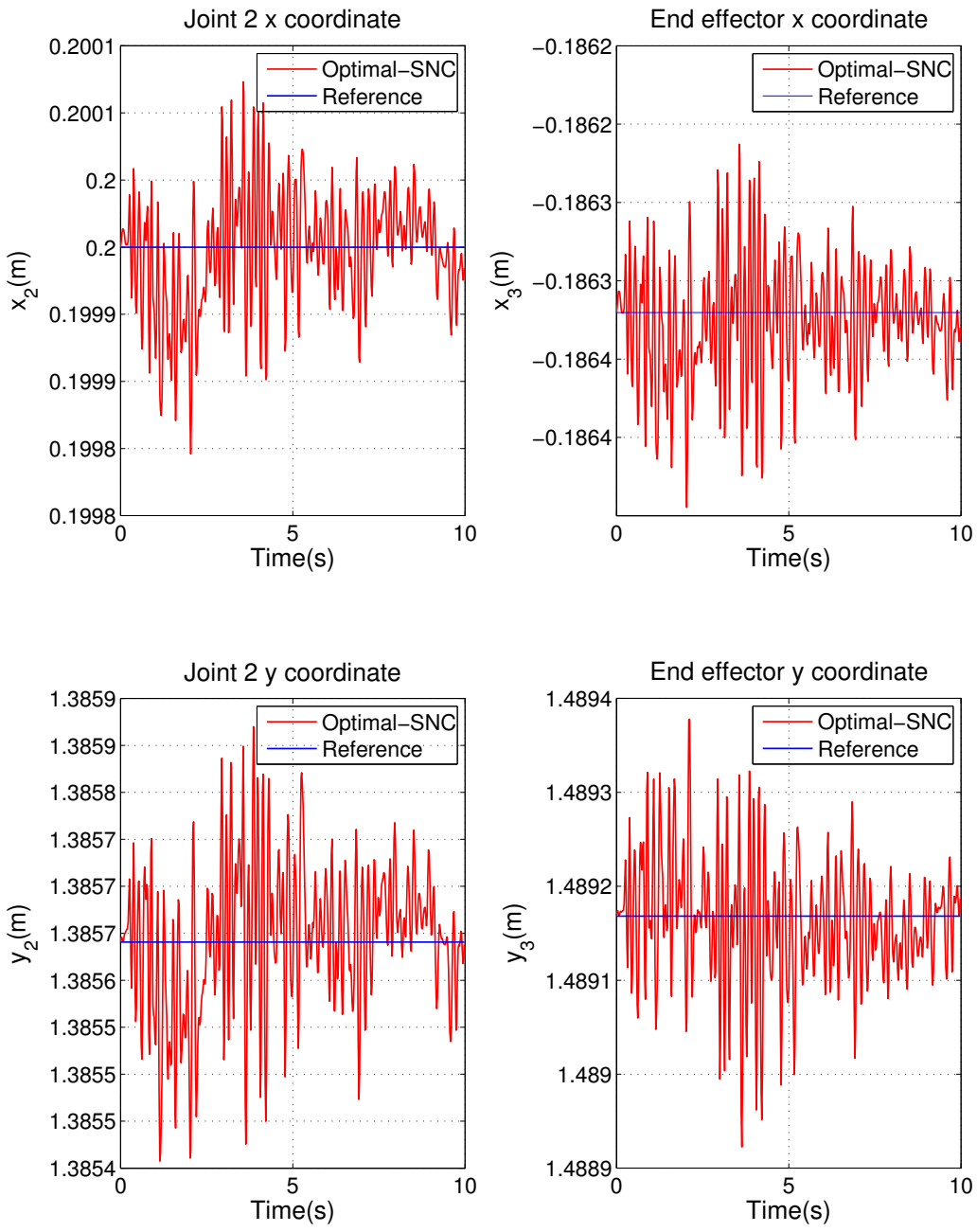

Figure 3.30: Different initial condition

CHAPTER 4
BIO-DYNAMICS OF THE CERVICAL SPINE

4.1 Background

The effects of vibration exposure on system occupants may be discomfort, health risk, and poor performance, which are major concerns in many occupations with moving environments such as farming and construction machinery [10, 11, 12, 13, 14, 15]. Reduction in the latter problems may be achieved by reducing the magnitude of the energy transferred to the body or by changing the characteristics of the motion such that the energy transfers at frequencies that are less harmful to the human body. While experimentations may provide significant insight into human biodynamics during vibration [10, 12, 14], computer human models may present less expensive tools with a potential for evaluations that go beyond the experimentation's allowable ethical limits and would help in the development of more effective suspension systems. Still, due to the complexity of the motion in WBV [16, 17], the nonlinearity, and the involuntary muscle activation of the human body [15, 18, 19], advances in predictive computer human modeling become a challenging issue.

Many human models have been suggested to resemble human response under dynamic loading including low frequency vibration, impact, and blast [46, 47, 48]. Most models developed to assess impact and blast are not suitable to assess WBV application or repeated shock responses [49] because they are designed for high acceleration that can reach hundreds of gravitational accelerations (g) and therefore are

very sensitive to inertia forces. On the other hand, WBV is occurring at relatively low frequency, which is affected by the stiffness and the damping of the human body.

The development of predictive computer human models in WBV has shown some success in predicting simple types of motion, mostly in the uni-axial vertical direction, under specific boundary conditions [49, 50, 18, 51]. In these models, discrete mass-spring-damper [52, 53], rigid bodies connected by viscoelastic elements and muscle groups [26, 50], and finite element models [27, 28, 19] were used to model human body response to vibration. Some of these models [50, 27, 28] showed good potential in predicting joint and muscle forces and stresses using in some instances [27] very detailed finite element based schemes; however, the validity of these models have to be shown.

4.2 Current Computer Human Models in WBV

4.2.1 Spring-mass-damper Models

While detailed biomechanical models may provide comprehensive information about the system response and its physiological characteristics, a simple mechanism may also offer a good general picture about the system behavior.

Simple forms of spring-mass-damper models can be used to resemble the human response to vibration. A single mass resting on a spring and a parallel damper in Figure 4.1a is one example; its transmissibility graph is depicted in Figure 4.1b. The transmissibility is defined as the complex ratio between the cross-spectral density $S_{hs}(jw)$ of the input acceleration, which could be at a point on the seat, and

the output head acceleration, which could be at a point on the head, divided by the auto-spectral density $S_{ss}(jw)$ of the input acceleration.

$$T_h(jw) = \frac{S_{hs}(jw)}{S_{ss}(jw)} \tag{4.1}$$

Experimental data can be easily fit to such type of models. For example Griffin et al. [18] showed that, with damping coefficient $c = 0.6$ and natural frequency $w_n = 14$Hz, this simple model can resemble the vertical seat-to-head transmissibility of a group of males of 5th percentile to 95th percentile at a frequency range from $1 - 100$Hz. The spring-mass-damper system can be more involved with more degrees of freedom, such as the system shown in Figure 4.2 that has been adapted and used by the ISO 5982 (2001) for calculating the vertical transmissibility for sitting and standing human positions. Just recently, Toward and Griffin [54], 2010, used a single-degree-of-freedom model with appropriate variations in the model's parameters to investigate the effect of posture and vibration magnitudes on the apparent mass, which represents the complex ratio between the reaction forces and the accelerations at the input point on the seat, during vertical whole-body vibration.

In another study, Fritz [27] developed a human model for standing and sitting positions during vibration. The vibration properties of the model were adapted to fit a transfer function, which correlates the output and the input vibration signals, provided in the international standards and the literature. In the latter model, the compressive forces at the input point of the body were simulated under a vertical random vibration and the transfer functions between the accelerations of the

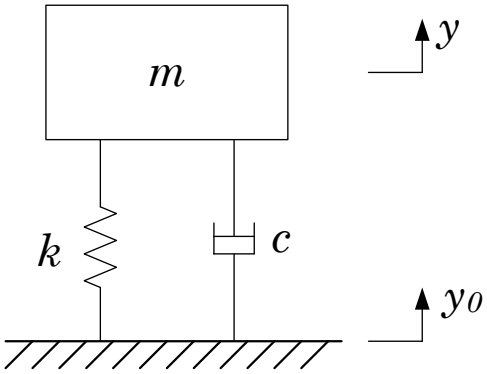

(a) A Single degree-of-freedom mass-spring-damper model

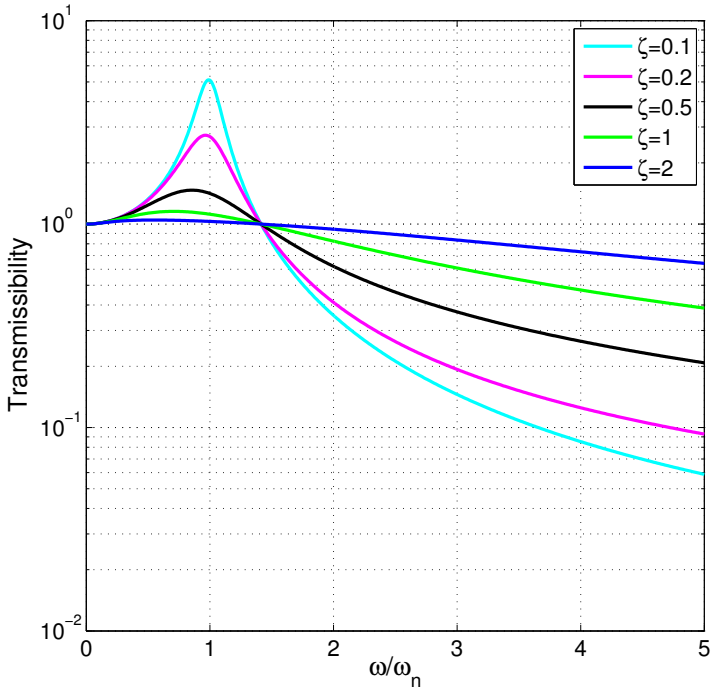

(b) The relationship between the transmissibility and the ratio of the applied frequency and the natural frequency under different damping conditions

Figure 4.1: A single degree-of-freedom model

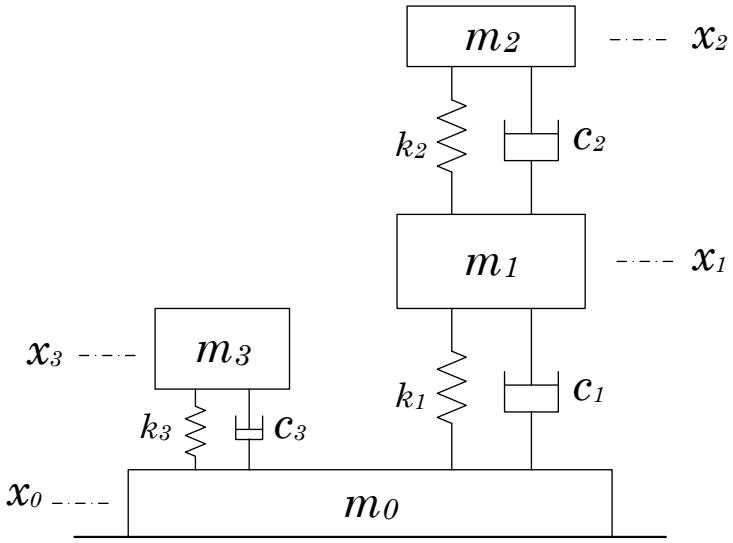

Figure 4.2: Multi-degree-of-freedom mass-spring-damper model to resemble human response to vertical whole-body vibration

ground or of the seat and the forces were computed. Using the mass and inertia properties of humans, three-dimensional complex head-spine models were developed by Belytschko et al. [46], and including the response of the head, rib cage, viscera, spinal elements, seatback, and restrain systems. In another study, Williams and Belyschko [55] included a detailed cervical spine model with muscles. Belytschko and Privitzer [56] in 1978, commented that the interaction of the spine and the viscera, ribs, and abdominal walls has a significant effect on the body's response to some impacts. Amirouche [57] proposed a 13-degree-of-freedom model coupled by linear springs of a multi-axis dynamic response of the body.

4.2.2 Multi-links Models

The multi-link models simulate the kinematics and inertial properties by a chain of rigid bodies linked by ideal pivot joints without modeling the stiffness and damping. Roberts [58] presented plane dynamic models with six segments coupled by springs to predict the human reaction to crash.

Fard et al. [59] used a double-inverted-pendulum to simulate the head-neck response to fore-aft WBV. They used the frequency domain identification method to determine the coefficients of the mathematical model of the head-neck and optimization methods to compute the coefficient of the spring-damper components. The authors found that the head-neck complex behavior was quasilinear with one dominant resonance frequency between 0.8 and 1.6 Hz and another dominant frequency between 5 and 6 Hz.

4.2.3 Anatomical-structure Models

Coupling of various directions of motions is a typical need for biodynamic response of a human, however, this is not considered in the anatomical models that mainly concentrate on vertical motions [60, 61, 62, 63, 64, 65, 66, 67, 19]. Dietrich et al. [68, 69] were the first to present a finite element model to the seated human containing one-dimensional and two-dimensional elements. Pankoke et al. [28] introduced an anatomical model that includes a large number of degree of freedom, considering geometrical and material nonlinearity.

Pankoke [70] developed a dynamic three-dimensional finite element model with a detailed representation of the lumbar spine and back muscles (102 elements). All part of the human model were compared with experimental data in the literature (especially for vertical single axis motion).

4.3 Head-Neck Models

There is a great need for a detailed cervical spine model for characterization of the flexion-extension motion in the sagittal plane due to fore-aft WBV. Only a limited number of models currently exist in the literature, such as the models by Fard [59, 71]. As with other biomechanical models, the head-neck model can be categorized into passive and active models.

4.3.1 Passive Model

In this model, the systems' parameters such as stiffness and damping are selected to fit the experimental data. One example is the system shown in Figure 4.2.

The logic behind the passive human models is to consider the human body as a black box and then identify its properties using information from the experimental input and output signals. In this process, experimental vibration input data are applied to the human body and the human response output data are collected using motion tracking systems. In the passive human model identification process, the input vibration data is applied to the passive human model and its properties are varied until the model output matches the output of the recorded experimental data.

Both the time domain and the frequency domain analyses can be used for the system identification. If the frequency analysis is used, then, the data is transferred from the time domain to the frequency domain using the fast Fourier transform (FFT). A transfer function is then created as the complex ratio between the output and the input signals. A system identification process augmented with optimization schemes is then used to induce appropriate spring and damper coefficients. The resulting system is then used to predict the output displacement in response to the vibration input signals. The predicted capability of these models is normally restricted within the data used during the system identification process. Still, these models can predict human responses under vibration signals that are outside the range of the signals used in the first place in the model development; however, their prediction will have some errors. Figure 4.3 demonstrated the steps in identifying the parameters of a passive human model.

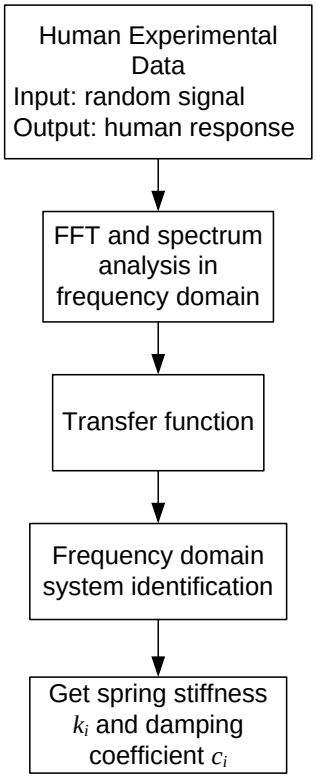

Figure 4.3: Identification of passive model

4.3.2 Active Model

The active head-neck model is similar to the passive model in terms of having spring and passive dampers representing the passive muscle and soft tissues, however it has additional active dampers representing the active muscle joint torques. The coefficients of the parameters are usually inferred from experimental data or from control schemes.

4.4 Motivation

Besides the complexity of developing effective rigid-link biomechanical models with viscoelastic parameters during fore-aft WBV, one major issue that has not yet been solved in the field of human biodynamic in WBV is the non-linearity of the human response under different vibration magnitudes. Previous studies [14, 51, 72] showed that the response of the human body to vertical and fore-aft directions is sensitive to the vibration magnitudes and therefore demonstrates nonlinearity in the response. The nonlinearity is characterized by a softening response with increases in the magnitude of vibration, meaning that the natural frequencies of the human body become smaller with increasing vibration acceleration magnitudes. This change in human characteristics may also affect human perception to discomfort and injury risk [14]. Robertson and Grin [73], 1989, showed that a doubling of the vibration magnitude did not result in a doubling of the EMG activity. They related this behavior to a softening system in the muscle forces. They concluded that the resonance frequencies and the non-linearities in the response may be caused by a complex combination

of sources that could include the dynamic response of the tissue beneath the ischial tuberosities, the bending or buckling response of the spine, and the active responses of the muscles. Thus passive human models that are based on optimization at one vibration magnitude may be inappropriate for capturing the response of human at different vibration magnitudes.

While the non-linearity of the human biodynamic and the softening behaviors have been investigated experimentally by several researchers, the work has still mainly focused on the spine area of the human body. To the author's knowledge, there is no experimental study that investigates the nonlinearity in the cervical spine response under different vibration magnitudes.

In addition to affecting the capability of the human model to predict human response at different vibration magnitudes, the nonlinearity in human response and the softening behavior play a significant role on the design of seat's vibration suppression systems. With different vibration magnitudes, the critical harmful frequencies will be shifted, which may decrease the effectiveness of the seats' suspension systems if the latter is designed to target certain frequencies based on one vibration magnitude. Therefore, the development of computer human models that can capture the softening characteristic of the human body response under different vibration magnitude will enable the improvement of spinal and cervical models as well as the design of seats with better performances.

Additionally, most current models are able to correlate the motions of the output point (end-effector) and the input point with a certain degree of accuracy;

however, they might face difficulties predicting the motion at the intermediate points between the input and the end-effector. Therefore, the development of a multi-link model that predicts the motion of the intermediate critical joints on the neck such as C1-C2, C4-C5, and C7-T1 can assist researchers in investigating pathological or design problems at certain locations on the cervical spine due to exposure to vibration.

4.5 Chapter Objective

- Experimentally investigate the types of nonlinearity in the cervical spine response under fore-aft WBV.
- Develop active rigid-link human head-neck computer models with viscoelastic elements to predict human response to fore-aft WBV.
- Investigate the capability of the proposed models in capturing the softening response (nonlinearity) of the head-neck with increased vibration magnitudes and compare that with a passive model.
- Investigate the capability of the model to predict the motion at intermediate joints between the input and the end-effector.

4.6 Methods

Experimental data from seated human subjects under fore-aft WBV files were collected and used in the development of the proposed active head-neck model.

4.6.1 Participants

Five healthy male subjects were used in this study with an average age of 20.4 ± 3.2 years, height of 1.788 ± 0.062m, and weight of 75.24 ± 12.56kg. Subjects reported no prior neck, shoulder, or head injuries, nor any neurological conditions. Written informed consent, as approved by the University of Iowa Institutional Review Board, was obtained prior to testing. Experiments were conducted where the subjects sat with their back leaning and strapped to the seat-back and their arms on their laps.

4.6.2 Measurements

A 12 infrared camera Vicon Motion Capture System (Vicon, California, Los-Angeles, USA) with a resolution of 0.3 megapixels per frame and a peak capture rate of 200 Hz) was used to collect position data on passive reflective markers. Fifteen reflective markers were attached to the subject's skin to highlight anatomical landmarks on the head-neck area (Figure 4.4), the shoulder, the clavicle, and the sternum. The markers on the head were placed just superior and lateral to each eyebrow, as well as on each side of the back of the head. The four markers were then used to calculate the position of a point at the center of the head during the motion. For the neck, three markers were placed on C7-T1, three markers were placed on C4-C5, and one marker was placed on each side at C1-C2. The finite difference method was used to calculate the velocity and the acceleration from the position-based markers; however, accelerometers were attached to the rigid platform and were used as references for the post-processing filtration [74].

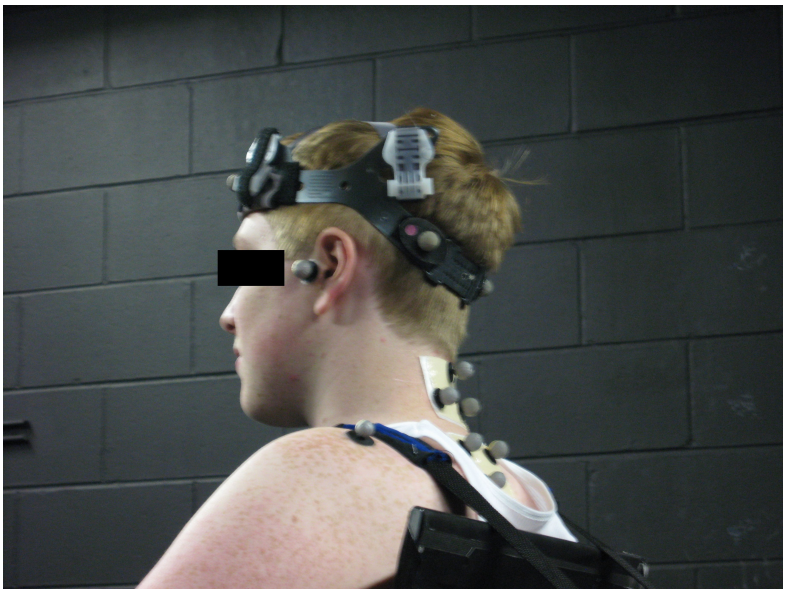

Figure 4.4: Markers on the head and neck

A six-degree-of-freedom man-rated motion platform (the Moog-FCS 628-1800 six-degree-of-freedom electrical motion system, Moog-FCS, Ann Arbor, Michigan, USA) with a rigid seat was used to simulate input random vibration files with different vibration magnitudes.

4.6.3 Performance Measures

In vibration studies, the system accelerations and velocity are considered critical parameters in calculating various vibration performance measures such as the transmissibility, apparent mass, and impedance. However, for some applications, the displacement is very important [72]. In this work, the displacement, acceleration, power spectral density, and transmissibility will be used as measures for the effectiveness of the proposed active human head-neck model.

4.7 Proposed Active Head-Neck Model

Our hypothesis is that the experimental human response data during fore-aft WBV contain all the information that describes the biodynamic response of the head-neck region in a strong coupled mode. The goal is to extract the information that contains the passive and the active part of the response. While the passive response including the tissue and the passive parts of the muscles can be modeled by spring type modules (could be linear or nonlinear), the active part of the muscle is normally proportional to the velocity, acceleration, and possibly the jerk of the motion. In this work, the parameters of the passive system are derived from cadaver studies to resemble the stiffness of the joint and the passive tissues.

In order to extract the active information from the experimental data, a passive model is first initialized with appropriate spring of stiffness coefficients. Initial joint torques are then applied to the joints of the system to assist the system in achieving the required posture and the static equilibrium condition. This is followed by applying the experimental vibration input data to the base of the model. At this step, and as expected, the output motion of the model will not match that of the experiments, and error will be presented. Following this step, active dampers with unknown coefficients are added to the system to resemble the active part of the muscles. Optimization and control schemes are then used to determine and refine the parameters of the active dampers, so that the active model can reproduce the experimental output data with a high degree of accuracy. During the latter refining process, the final active damper parameters' magnitudes are stored with the current model joint angles in a database

with a structure that can be searched using the kd-tree method of Section 2.5.2. The following flow chart (Figure 4.5) demonstrates the steps for building the database.

Once the database is established, the magnitudes of the active dampers in response to new external fore-aft vibration input signals can be derived from the database based on the angle, angular velocity, and angular acceleration of each link in the model. Figure 4.6 shows the steps in using the database in predicting the output motion.

Studies in static and dynamics biomechanics of the cervical spine [75, 76] showed the importance of considering the motion of the individual cervical inverte-brate. Most studies agreed that the critical regions would be C1-C2, C4-C5, and C7-T1. In the following sections a one link model is first introduced to demonstrate the structure and the effectiveness of the proposed active head-neck model. Two- and three-link models are then introduced to show the capability of this model to deal with multiple-link systems.

4.7.1 One-link Head and Neck Model

A single-degree-of-freedom model of the head and neck system is shown in Figure 4.7. In this model, m_1 is the mass of the neck, which is represented by a uniformly distributed mass straight bar. m_2 is the mass of the head, which is represented by a uniformly distributed circular-planar mass. The head is rigidly attached to the neck. L is the distance between the center of the head at $C0$ and the center of the neck at $C7$. r is the radius of the head. Point p is the center of mass of

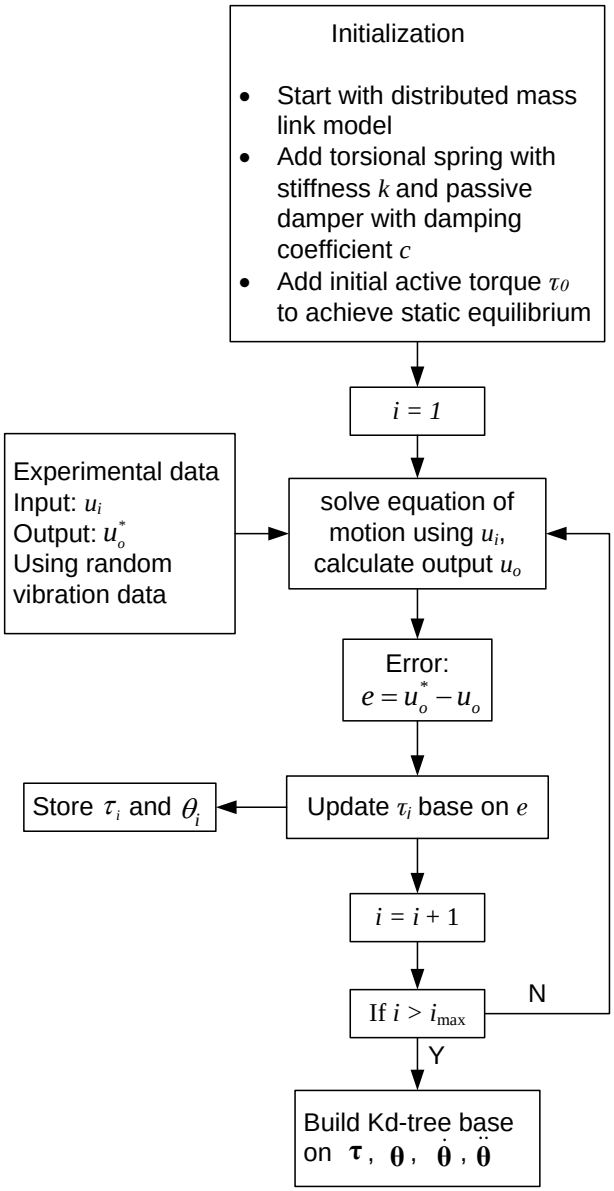

Figure 4.5: Flow chart showing the steps in building the database for the active model

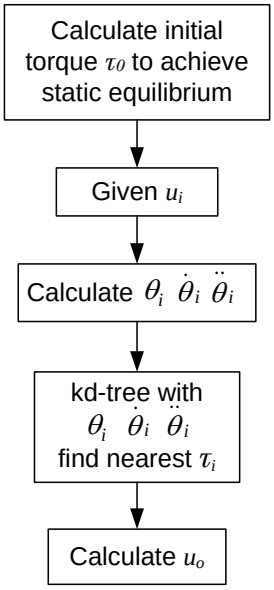

Figure 4.6: Flow chart showing the steps in using the database to predict the output motion of the active mode

the head and neck system. Therefore, l represents the distance between the center of mass of the system and $C7$ (point o). k is the stiffness of the spring, c is the damping coefficient, τ is the active muscle force, θ is the rotation angle, x_0 is the horizontal displacement of $C7$, and x is the horizontal displacement of $C0$.

The head and neck system is a nonlinear system. The linearized model around the initial angle θ_0 is described in the following equation:

$$I_o\Delta\ddot{\theta} + c\Delta\dot{\theta} + (k - mglsin\theta_0)\Delta\theta = mlsin\theta_0\ddot{x}_0 + \Delta\tau \tag{4.2}$$

where $\Delta\theta = \theta - \theta_0$, $\Delta\tau = \tau - \tau_0$. τ_0 is the initial muscle force at the initial static condition. I_o is the moment of inertia around point o, and $I_o = \frac{1}{3}m_1(L-r)^2 +$

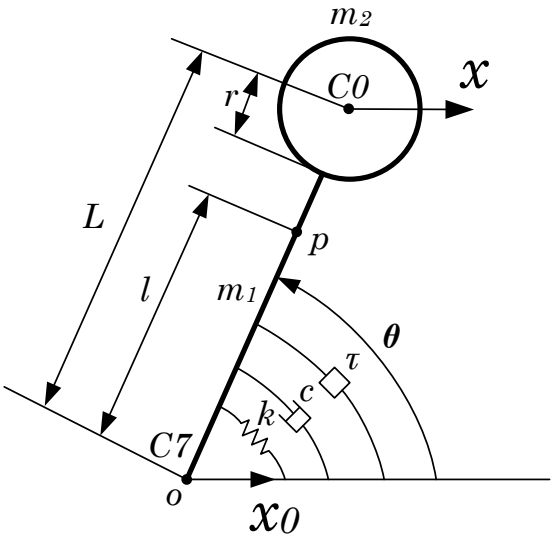

Figure 4.7: One-link head and neck model

$\frac{1}{2}m_2r^2 + m_2L^2$. m is the total mass of the head and neck system, and $m = m_1 + m_2$.

Using the Laplace transform on Equation 4.2, the transfer functions of the linear head and neck model in s domain are obtained. $\Delta\Theta/X_0$ is the transfer function between the changing of the angular displacement $\Delta\Theta$ and the excitation displacement X_0. $\Delta\Theta/\Delta T$ is the transfer function between the changing of the angular displacement $\Delta\Theta$ and the changing of the muscle force ΔT.

$$\frac{\Delta\Theta}{X_0} = \frac{\frac{mlsin\theta_0}{I_o}s^2}{s^2 + \frac{c}{I_o}s + \frac{k - mglsin\theta_0}{I_o}} \tag{4.3}$$

$$\frac{\Delta\Theta}{\Delta T} = \frac{\frac{1}{I_o}}{s^2 + \frac{c}{I_o}s + \frac{k - mglsin\theta_0}{I_o}} \tag{4.4}$$

Passive and active one link systems will be presented in this section for the sake

of comparison and insight. The passive-spring-damper system with constant k and c parameters is characterized based on the flow chart of Figure 4.3. The parameters are optimal coefficients identified from the experimental data using the work of the current Ph.D. student Yang Wang. The mass of the head and the neck in the active model were based on studies by Dempster et al. [77] and Liu et al. [78]. The active system has passive parameters k and c obtained from Moroney's paper [79] and Fard's paper [71]. The database for the active muscle force is constructed and characterized using the algorithm shown in Figure 4.5.

Random input fore-aft vibration files with three different magnitudes($0.46m/s^{-2}$ root-mean-square value (rms) (Mag1), $1.32m/s^{-2}$ rms (Mag2), $1.66m/s^{-2}$ rms (Mag3)) were applied to the shaker table. The passive and the active model parameters were identified based on the vibration signals using magnitudes 1 and magnitude 3. Then, both models were tested using input vibration signals with magnitude 2, which was not used in the system identification process of the passive model or in the database construction of the active model.

Figure 4.8 shows the transmissibility of the experimental data for subject 2 under the three vibration magnitudes. As can be seen, the subject showed softening characteristics with the peak frequencies shifting to the left with increased vibration magnitude.

Similar behaviors were observed on the rest of the subjects with the exception of subject 1, who showed inconsistent behavior, as shown in Figure 4.9.

Figure 4.10 depicts the displacement of the end-effector using the experimental

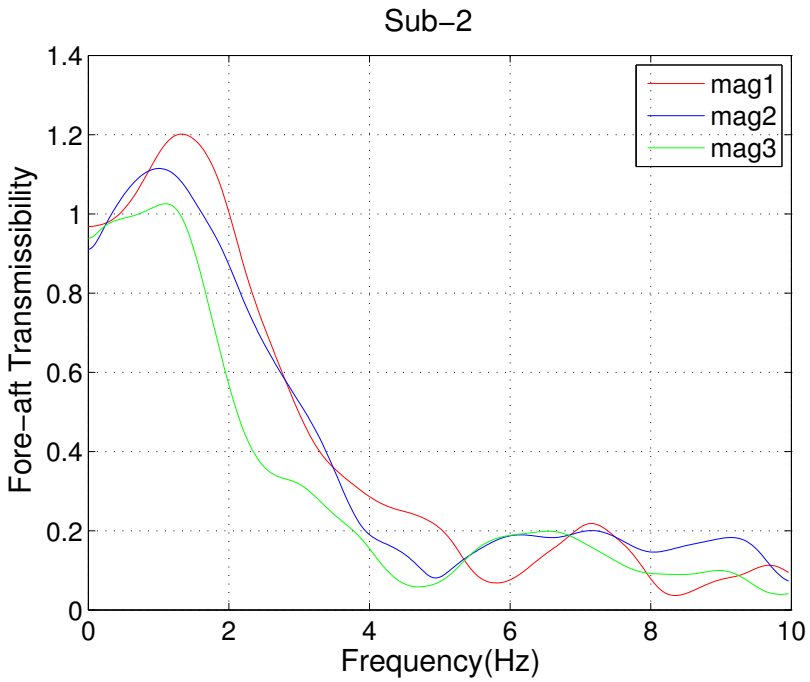

Figure 4.8: Fore-aft Transmissibilty of subject 2 under magnitude 1, 2, and 3

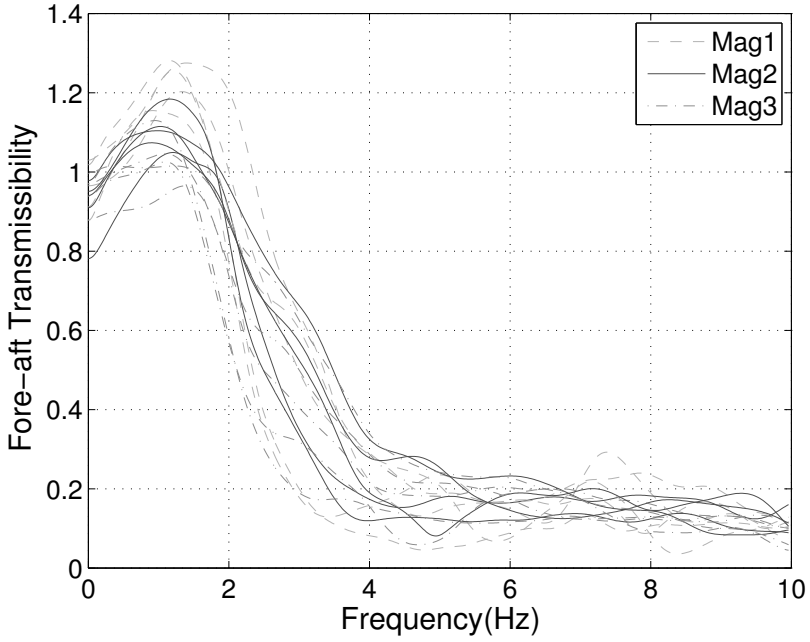

Figure 4.9: Fore-aft Transmissibilty of all subjects under magnitude 1, 2, and 3

measured data, the passive model, and the active model under input vibration of magnitude 2. It should be noted here that the latter signal is new to both the passive and the active systems. As can be seen from the figure, the predicted displacement of the active model followed the experimental data very closely during the 30 seconds ride, with small overshooting taking place at the peaks. The predicted displacement of the passive model followed the trend of the experimental displacement in a coarser fashion.

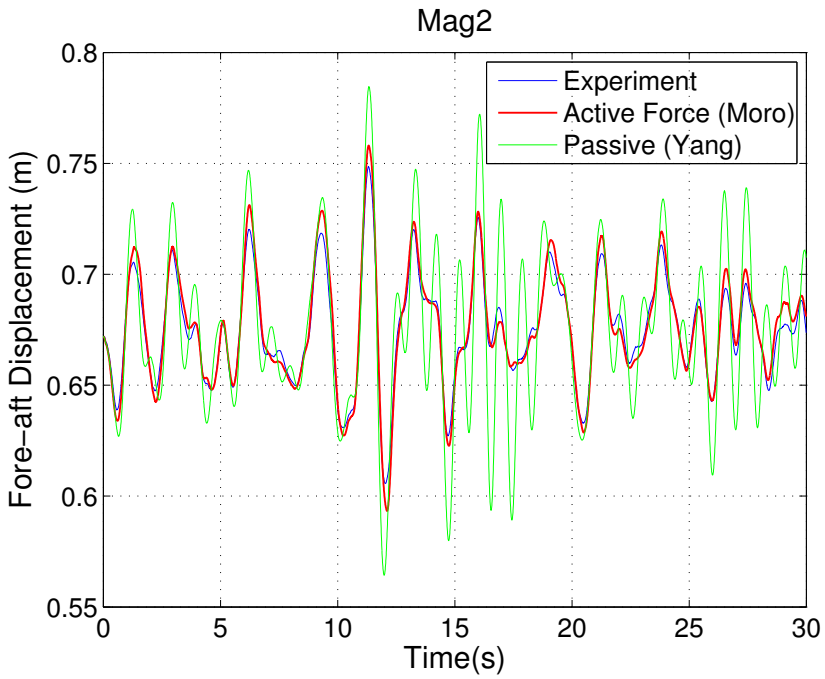

Figure 4.10: Fore-aft Mean displacement of the experimental, passive, and active models under vibration signal of magnitude 2

A comparison between the experimental acceleration of the end-effector and that of the passive and active models are shown in Figure 4.11. As expected, the acceleration of the passive model showed higher magnitude than the experimental data and that of the active model, with the active model still close to the experimental data.

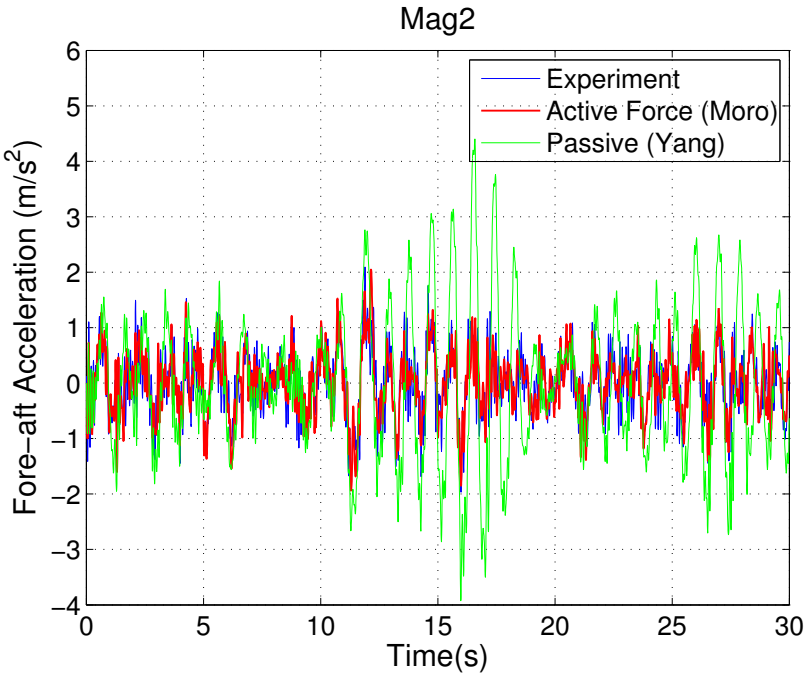

Figure 4.11: Fore-aft Mean acceleration of the experimental, passive, and active models under vibration signal of magnitude 2

To check the characteristics of the end-effector acceleration in the frequency domain, a power spectral analysis of the acceleration is depicted in Figure 4.12. It

appears that the passive model matched to a certain degree the experimental data at low frequencies and then started to deviate after that. On the other hand, the active model shows frequency components with energy that are closer to the experimental data.

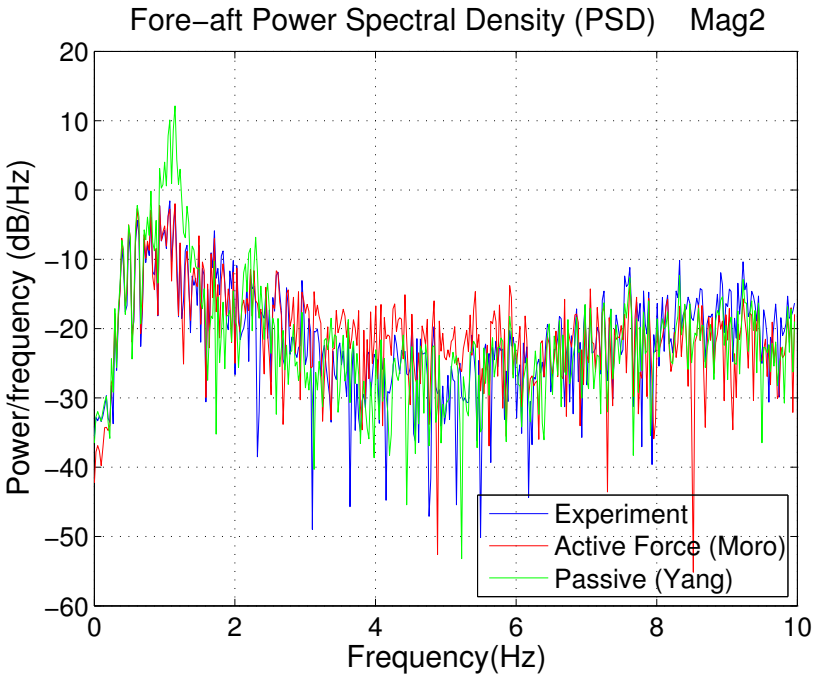

Figure 4.12: Fore-aft Mean power spectrum density of the experimental, passive, and active models under vibration signal of magnitude 2

Figure 4.13 depicts the transmissibility of the five subjects under the vibration signals of magnitude 1 and magnitude 3, which were used in the first place to build the database for the active system and for the system identification of the passive system.

As can be seen, the active model followed the experimental data very closely and was able to capture the softening effect due to the increases in vibration magnitude. The passive system showed deviation in the magnitudes and the location of the peak frequencies under both magnitudes.

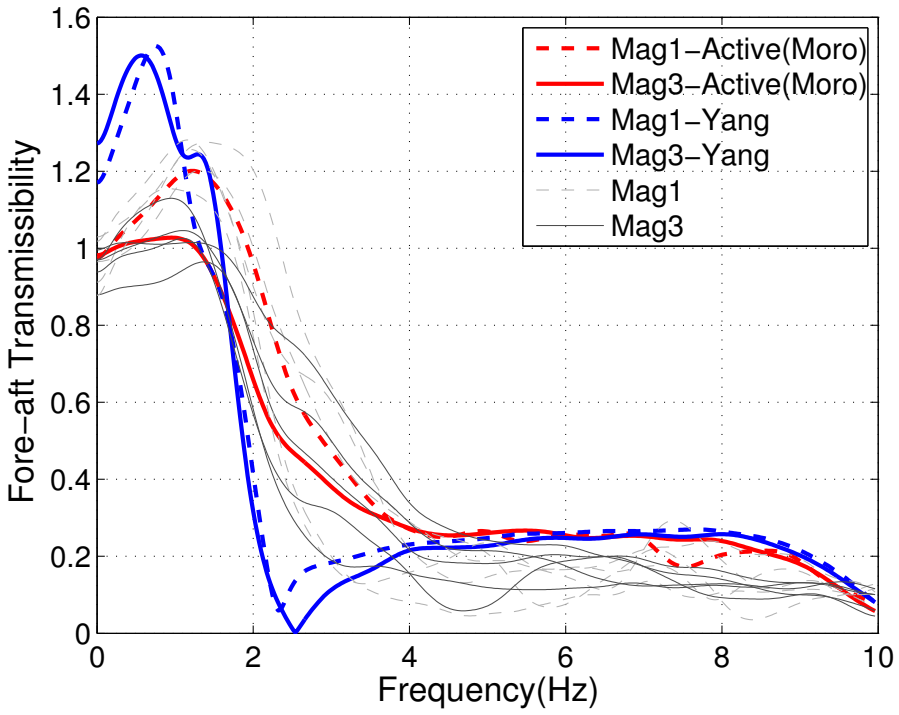

Figure 4.13: Fore-aft Mean Transmissibility of the experimental, passive, and active models under vibration signal of magnitude 1 and magnitudes 3

When tested under vibration signals of magnitude 2, the active system showed closer magnitude to that of the subjects, with the peak frequency slightly shifted to

the left as shown in Figure 4.14.

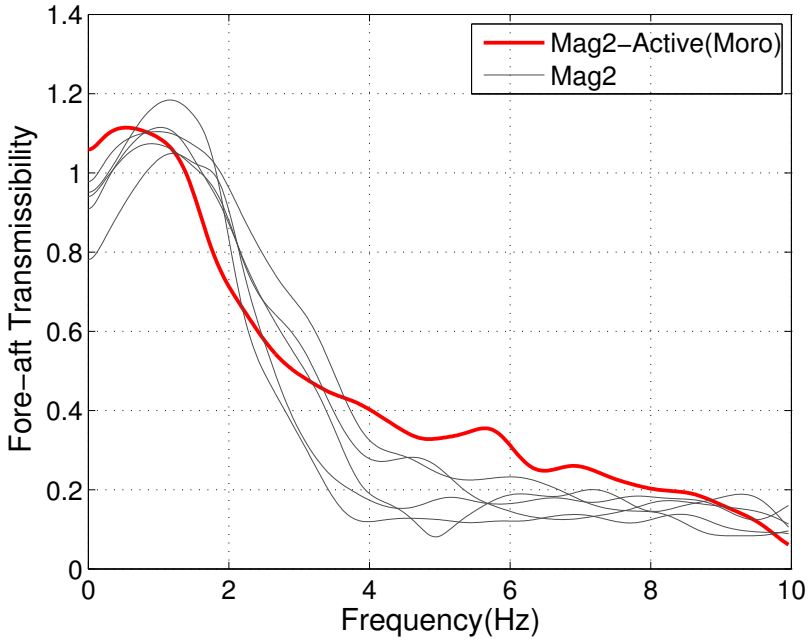

Figure 4.14: Fore-aft Mean Transmissibility for the experimental and active models under vibration signal of magnitude 2

4.7.2 Two-link Head and Neck Model

A two-link head and neck model is shown in Figure 4.15. The links have characteristics similar to those of the one-link model. Link 1 has a mass m_1 and length L_1. Point p_1 is the center of mass of link 1. l_1 is the distance between point p_1 and the first joint at point o ($C7$). k_1 is the spring stiffness of link 1, and c_1 is the damping coefficient of link 1. τ_1 is the active muscle force attached to link 1. Link

2 has a mass m_2 and length L_2. Point p_2 is the center of mass of link 2. l_2 is the distance between point p_2 and the second joint at point $C4$. k_2 is the spring stiffness of link 2, and c_2 is the damping coefficient of link 2. τ_2 is the active muscle force attached to link 2. θ_1 and θ_2 are the rotation angles of links 1 and 2, respectively. x_0, x_1, and x_2 are the horizontal displacements of $C7$, $C4$, and $C0$, respectively.

The mass of the links in the two-link model were based on studies by Dempster et al. [77] and Liu et al. [78]. The constant k in the model was obtained from Moroney's paper [79], and c was obtained from Fard's paper [59].

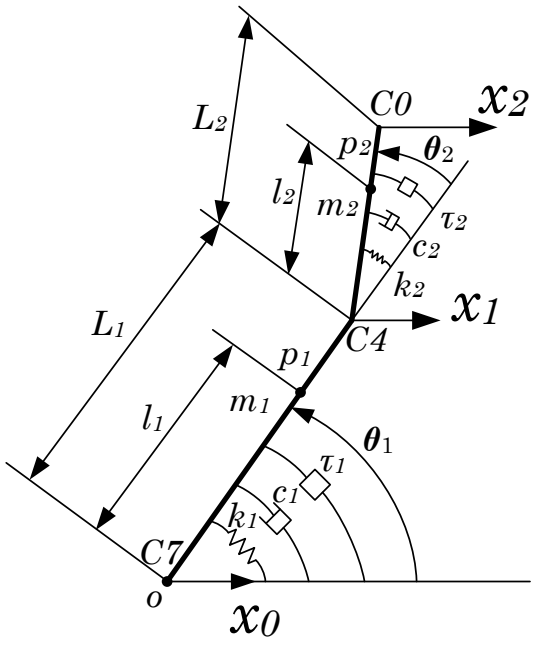

Figure 4.15: Two-link head and neck model

The two-link head and neck system is a nonlinear and coupled system. The linearized model around the initial angle θ_{10} and θ_{20} are listed in the following:

$$\mathbf{M}\Delta\ddot{\boldsymbol{\theta}} + \mathbf{C}\Delta\dot{\boldsymbol{\theta}} + \mathbf{K}\Delta\boldsymbol{\theta} = \mathbf{E}\ddot{x}_0 + \Delta\boldsymbol{\tau} \tag{4.5}$$

where $\Delta\ddot{\boldsymbol{\theta}} = \begin{pmatrix} \Delta\ddot{\theta}_1 \\ \Delta\ddot{\theta}_2 \end{pmatrix}$, $\Delta\dot{\boldsymbol{\theta}} = \begin{pmatrix} \Delta\dot{\theta}_1 \\ \Delta\dot{\theta}_2 \end{pmatrix}$, $\Delta\boldsymbol{\theta} = \begin{pmatrix} \Delta\theta_1 \\ \Delta\theta_2 \end{pmatrix}$, $\Delta\boldsymbol{\tau} = \begin{pmatrix} \Delta\tau_1 \\ \Delta\tau_2 \end{pmatrix}$,

$\Delta\theta_1 = \theta_1 - \theta_{10}$, $\Delta\theta_2 = \theta_2 - \theta_{20}$, $\Delta\tau_1 = \tau_1 - \tau_{10}$, $\Delta\tau_2 = \tau_2 - \tau_{20}$. τ_{10} and τ_{20} are the initial muscle forces of links 1 and 2 at the initial static condition. I_{p_1} and I_{p_2} are the moment of inertia of links 1 and 2, respectively, around their centers of mass.

$$\mathbf{M} = \begin{pmatrix} M_{11} & M_{12} \\ M_{21} & M_{22} \end{pmatrix}, \mathbf{C} = \begin{pmatrix} C_{11} & 0 \\ 0 & C_{22} \end{pmatrix}, \mathbf{K} = \begin{pmatrix} K_{11} & K_{12} \\ K_{21} & K_{22} \end{pmatrix}, \mathbf{E} = \begin{pmatrix} E_1 \\ E_2 \end{pmatrix},$$

$\mathbf{M}_{11} = m_1 l_1^2 + I_{p_1} + m_2 L_1^2 + m_2 l_2^2 + I_{p_2} + 2m_2 L_1 l_2 cos\theta_{20}$,

$\mathbf{M}_{12} = m_2 l_2^2 + I_{p_2} + m_2 L_1 l_2 cos\theta_{20}$,

$\mathbf{M}_{21} = \mathbf{M}_{12}$,

$\mathbf{M}_{22} = m_2 l_2^2 + I_{p_2}$,

$\mathbf{C}_{11} = c_1$,

$\mathbf{C}_{22} = c_2$,

$\mathbf{K}_{11} = k_1 - (m_1 l_1 + m_2 L_1) g sin\theta_{10} - m_2 g l_2 sin(\theta_{10} + \theta_{20})$,

$\mathbf{K}_{12} = -m_2 g l_2 sin(\theta_{10} + \theta_{20})$,

$\mathbf{K}_{21} = \mathbf{K}_{12}$,

$\mathbf{K}_{22} = k_2 - m_2 g l_2 sin(\theta_{10} + \theta_{20})$,

$\mathbf{E}_1 = (m_1 l_1 + m_2 L_1) sin\theta_{10} + m_2 l_2 sin(\theta_{10} + \theta_{20})$,

$\mathbf{E}_2 = m_2 l_2 sin(\theta_{10} + \theta_{20})$,

Set $x_1 = \Delta\theta_1$, $x_2 = \Delta\theta_2$, $x_3 = \Delta\dot{\theta}_1$, and $x_4 = \Delta\dot{\theta}_2$. The differential equations 4.5 is transferred to the state-space equation.

$$\begin{aligned} \dot{\mathbf{x}} &= \mathbf{A}\mathbf{x} + \mathbf{B_1}\mathbf{u} + \mathbf{B_2}\ddot{x}_0 \\ \mathbf{y} &= \mathbf{C}\mathbf{x} \end{aligned} \tag{4.6}$$

where

$$\mathbf{x} = \begin{pmatrix} x_1 \\ x_2 \\ x_3 \\ x_4 \end{pmatrix} = \begin{pmatrix} \Delta\theta_1 \\ \Delta\theta_2 \\ \Delta\dot{\theta}_1 \\ \Delta\dot{\theta}_2 \end{pmatrix}, \mathbf{y} = \begin{pmatrix} \Delta\theta_1 \\ \Delta\theta_2 \end{pmatrix}, \mathbf{u} = \begin{pmatrix} \Delta\tau_1 \\ \Delta\tau_2 \end{pmatrix},$$

$$\mathbf{A} = \begin{pmatrix} \mathbf{0} & \mathbf{I} \\ \mathbf{M}^{-1}\mathbf{K} & \mathbf{M}^{-1}\mathbf{C} \end{pmatrix}, \mathbf{B_1} = \begin{pmatrix} \mathbf{0} \\ -\mathbf{M}^{-1} \end{pmatrix}, \mathbf{B_2} = \begin{pmatrix} \mathbf{0} \\ -\mathbf{M}^{-1}\mathbf{E} \end{pmatrix},$$

$$\mathbf{C} = \begin{pmatrix} 1 & 0 & 0 & 0 \\ 0 & 1 & 0 & 0 \end{pmatrix},$$

$\mathbf{0}$ is zero vectors or matrix, $\mathbf{I}$ is a 2×2 identify matrix. The superscript -1 denotes the inverse of the matrices.

As with the one-link model, the active muscle force databases were built based

on the vibration signals of magnitude 1 and magnitude 3. A vibration signal with magnitude 2 was used to test the capability of the system to predict the motion under unknown vibration signals with different magnitudes than those of the data used to construct the database.

As shown in Figure 4.16, the displacement of the first link at x_1 of the active model showed characteristics very close to that of the experimental data. The end-effector at the end of the second link at x_2 showed a trend similar to that of the experimental displacement but not as good as the case with x_1.

Similar characteristics can be observed for the predicted acceleration (Figure 4.17) and the power spectrum density of Figure 4.18.

4.7.3 Three-link Head and Neck Model

Studies in static and dynamics biomechanics of the cervical spine [75, 76] showed the importance of considering the motion of the individual cervical invertebrate. Still, most studies agreed that the critical regions of interest would be the segments between the joints at C1-C2, C4-C5, and C7-T1. A three-link head and neck model is shown in Figure 4.19. The links are rigid and uniformly distributed-mass straight bar. Link 1 has a mass m_1 and length L_1. Point p_1 is the center of mass of link 1. l_1 is the distance between point p_1 and the first joint (point o $(C7)$). k_1 is the spring stiffness on link 1, and c_1 is the damping coefficient on link 1. τ_1 is the active muscle force on link 1. Link 2 has a mass m_2 and length L_2. Point p_2 is the center of mass of link 2. l_2 is the distance between point p_2 and the second joint

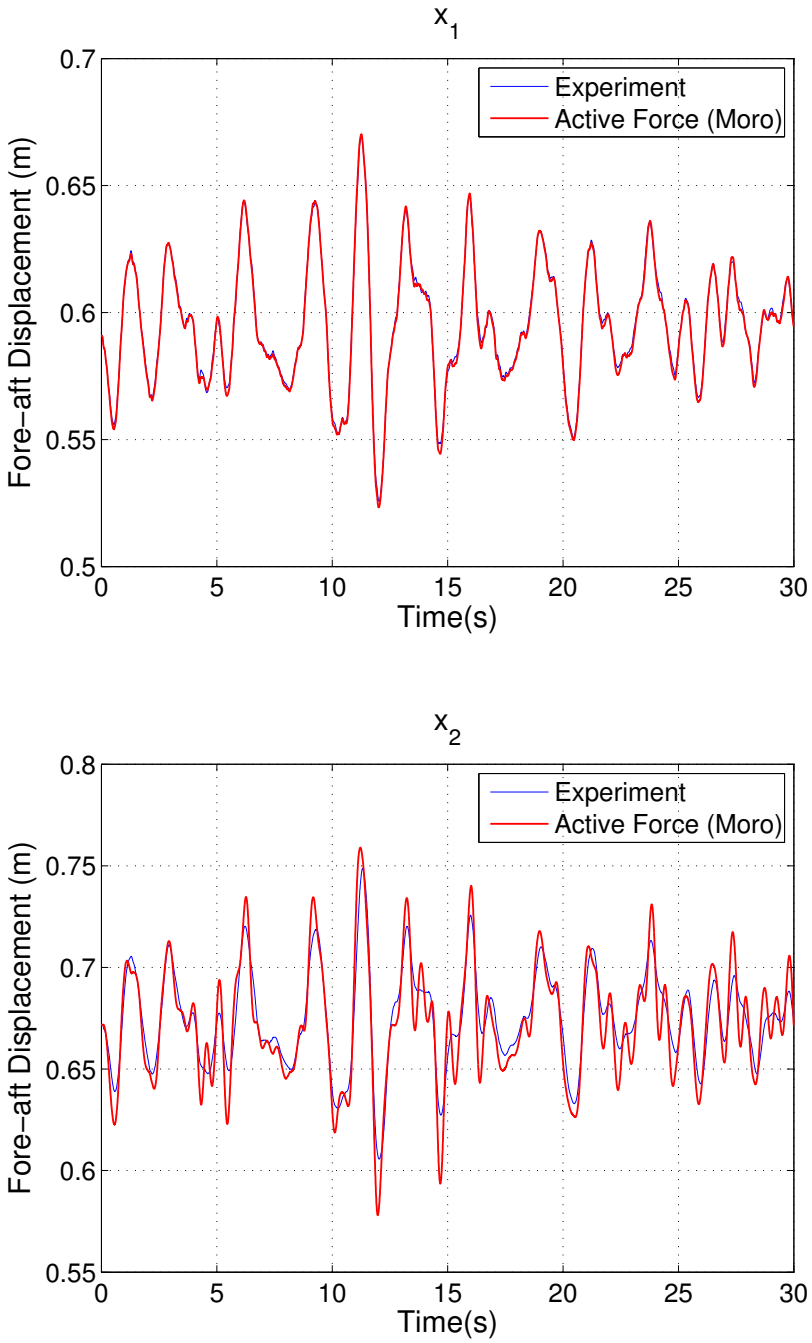

Figure 4.16: Fore-aft Mean displacement of x_1 and x_2 of the experimental and two-link model under vibration signal of magnitude 2

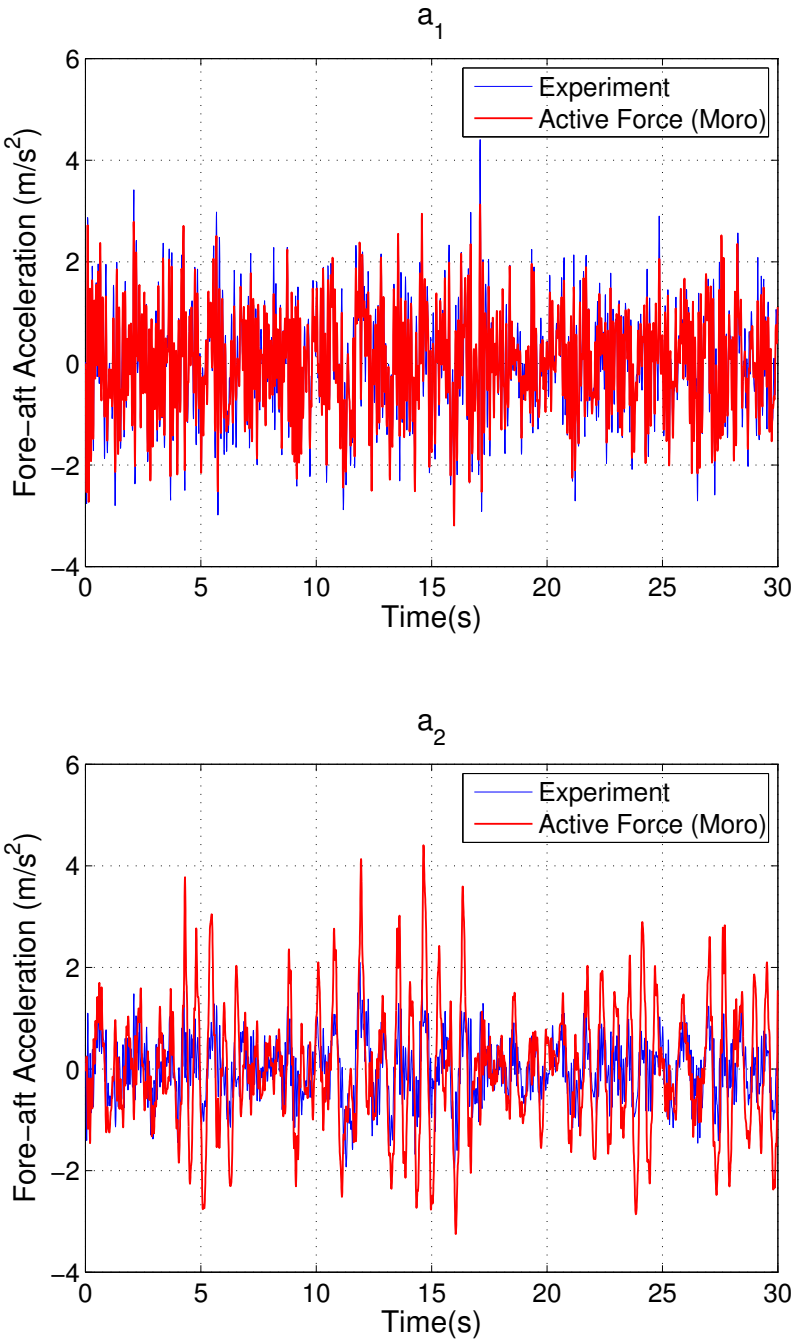

Figure 4.17: Fore-aft Mean acceleration of a_1 and a_2 of the experimental and two-link model under vibration signal of magnitude 2

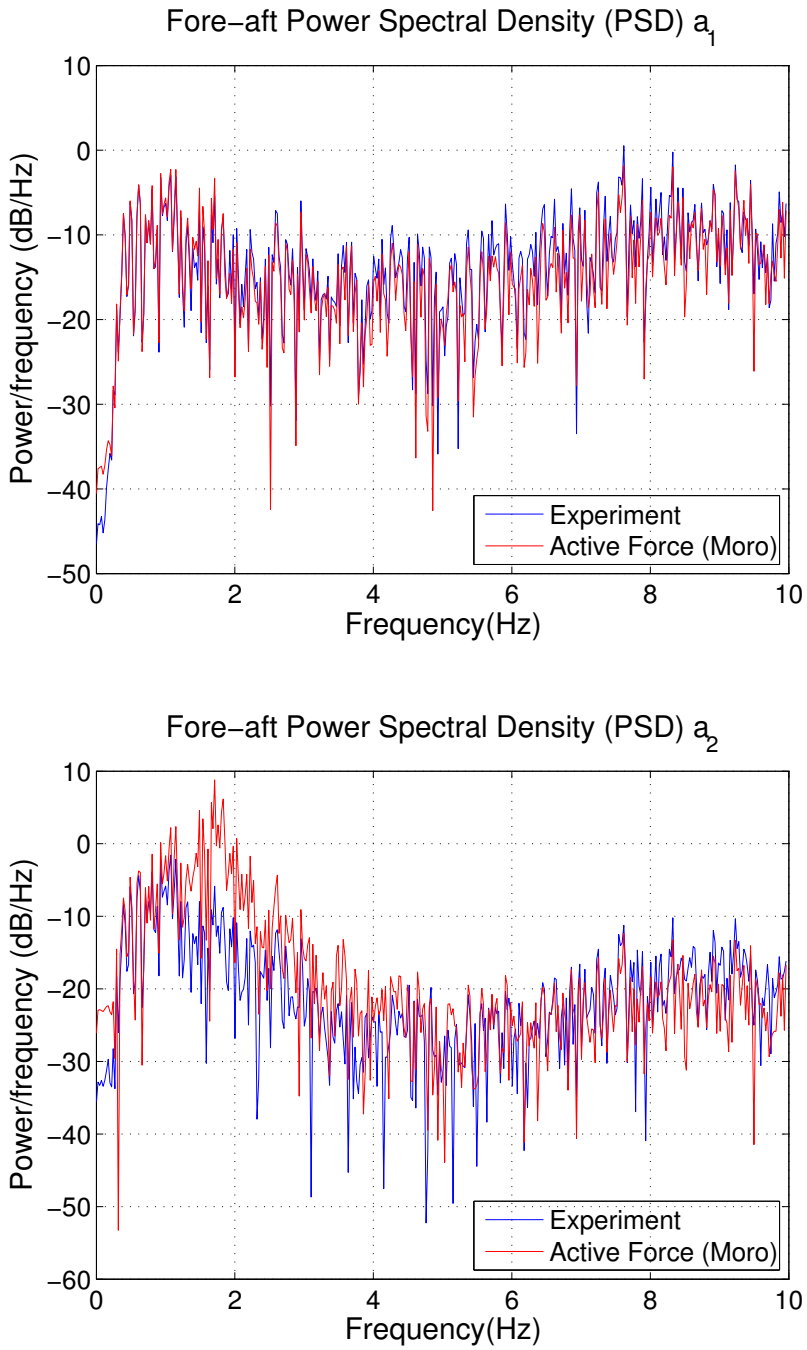

Figure 4.18: Fore-aft Mean power spectrum density of a_1 and a_2 of the experimental and two-link models under vibration signal of magnitude 2

(point $C4$). k_2 is the spring stiffness on link 2, and c_2 is the damping coefficient on link 2. τ_2 is the active muscle force on link 2. Link 3 has a mass m_3 and length L_3. Point p_3 is the center of mass of link 3. l_3 is the distance between point p_3 and the third joint (point $C1$). k_3 is the spring stiffness on the link 3, and c_3 is the damping coefficient on link 3. τ_3 is the active muscle force on link 3. θ_1, θ_2, and θ_3 are the rotation angles of links 1, 2, and 3, respectively. x_0, x_1, x_2, and x_3 are the horizontal displacements of points $C7$, $C4$, $C1$, and $C0$, respectively.

The mass of the links in the three-link model were based on studies by Dempster et al. [77] and Liu et al. [78]. The constant k in the model was obtained from Moroney's paper [79], and c was interpolated from Fard's paper [59].

The three-link head and neck system is a nonlinear and coupled system. The linearized model around the initial angle θ_{10}, θ_{20}, and θ_{30} are listed in the following:

$$\mathbf{M}\Delta\ddot{\boldsymbol{\theta}} + \mathbf{C}\Delta\dot{\boldsymbol{\theta}} + \mathbf{K}\Delta\boldsymbol{\theta} = \mathbf{E}\ddot{x}_0 + \Delta\boldsymbol{\tau} \tag{4.7}$$

where $\Delta\ddot{\boldsymbol{\theta}} = \begin{pmatrix} \Delta\ddot{\theta}_1 \\ \Delta\ddot{\theta}_2 \\ \Delta\ddot{\theta}_3 \end{pmatrix}$, $\Delta\dot{\boldsymbol{\theta}} = \begin{pmatrix} \Delta\dot{\theta}_1 \\ \Delta\dot{\theta}_2 \\ \Delta\dot{\theta}_3 \end{pmatrix}$, $\Delta\boldsymbol{\theta} = \begin{pmatrix} \Delta\theta_1 \\ \Delta\theta_2 \\ \Delta\theta_3 \end{pmatrix}$, $\Delta\boldsymbol{\tau} = \begin{pmatrix} \Delta\tau_1 \\ \Delta\tau_2 \\ \Delta\tau_3 \end{pmatrix}$,

$\Delta\theta_1 = \theta_1 - \theta_{10}$, $\Delta\theta_2 = \theta_2 - \theta_{20}$, $\Delta\theta_3 = \theta_3 - \theta_{30}$, $\Delta\tau_1 = \tau_1 - \tau_{10}$, $\Delta\tau_2 = \tau_2 - \tau_{20}$, $\Delta\tau_3 = \tau_3 - \tau_{30}$. τ_{10}, τ_{20}, and τ_{30} are the initial muscle forces of links 1, 2, and 3 at the initial static condition. I_{p_1}, I_{p_2}, and I_{p_3} are the moment of inertia of links 1, 2, and 3 around their centers of mass, respectively.

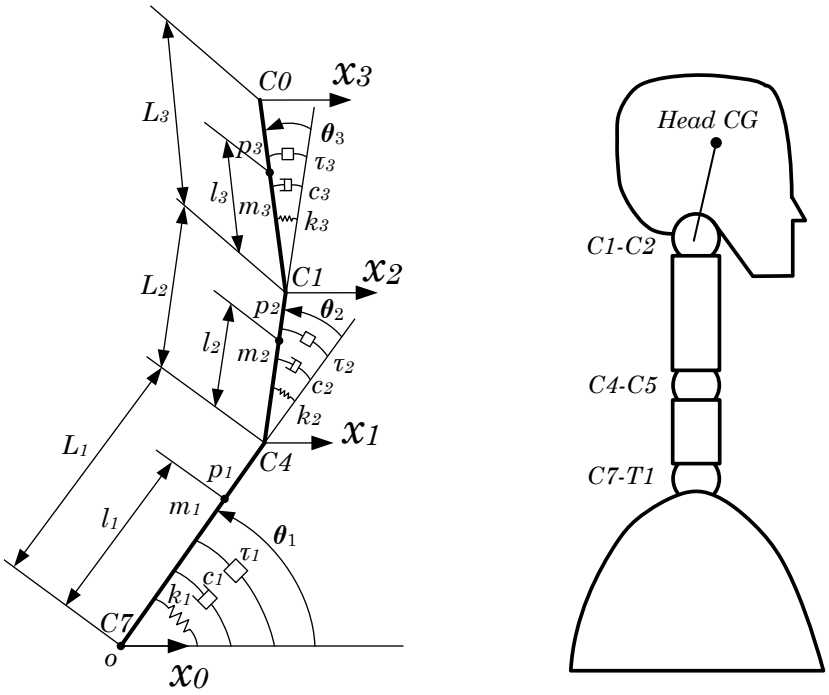

(a) Three-link head and neck model (b) Head and neck

Figure 4.19: Three-link head and neck model

$$\mathbf{M} = \begin{pmatrix} M_{11} & M_{12} & M_{13} \\ M_{21} & M_{22} & M_{23} \\ M_{31} & M_{32} & M_{33} \end{pmatrix}, \mathbf{C} = \begin{pmatrix} C_{11} & 0 & 0 \\ 0 & C_{22} & 0 \\ 0 & 0 & C_{33} \end{pmatrix}, \mathbf{K} = \begin{pmatrix} K_{11} & K_{12} & K_{13} \\ K_{21} & K_{22} & K_{23} \\ K_{31} & K_{32} & K_{33} \end{pmatrix},$$

$$\mathbf{E} = \begin{pmatrix} E_1 \\ E_2 \\ E_3 \end{pmatrix},$$

$$\mathbf{M}_{11} = m_1 l_1^2 + I_{p_1} + m_2 L_1^2 + m_2 l_2^2 + I_{p_2} + m_3 L_1^2 + m_3 L_2^2 + m_3 l_3^2 + I_{p_3}$$
$$+ (2m_2 L_1 l_2 + 2m_3 L_1 L_2) cos\theta_{20} + 2m_3 L_1 l_3 cos(\theta_{20} + \theta_{30}) + 2m_3 L_2 l_3 cos\theta_{30}$$

$$\mathbf{M}_{12} = m_2 l_2^2 + I_{p_2} + m_3 L_2^2 + m_3 l_3^2 + I_{p_3} + (m_2 L_1 l_2 + m_3 L_1 L_2) cos\theta_{20}$$
$$+ m_3 L_1 l_3 cos(\theta_{20} + \theta_{30}) + 2m_3 L_2 l_3 cos\theta_{30}$$

$$\mathbf{M}_{13} = m_3 l_3^2 + I_{p_3} + m_3 L_1 l_3 cos(\theta_{20} + \theta_{30}) + m_3 L_2 l_3 cos\theta_{30},$$

$$\mathbf{M}_{21} = \mathbf{M}_{12},$$

$$\mathbf{M}_{22} = m_2 l_2^2 + I_{p_2} + m_3 L_2^2 + m_3 l_3^2 + I_{p_3} + 2m_3 L_2 l_3 cos\theta_{30},$$

$$\mathbf{M}_{23} = m_3 l_3^2 + I_{p_3} + m_3 L_2 l_3 cos\theta_{30},$$

$$\mathbf{M}_{31} = \mathbf{M}_{13},$$

$$\mathbf{M}_{32} = \mathbf{M}_{23},$$

$$\mathbf{M}_{33} = m_3 l_3^2 + I_{p_3},$$

$$\mathbf{C}_{11} = c_1,$$

$$\mathbf{C}_{22} = c_2,$$

$\mathbf{C}_{33} = c_3,$

$\mathbf{K}_{11} = k_1 - (m_2 l_2 + m_3 L_2) g sin(\theta_{10} + \theta_{20}) - m_3 g l_3 sin(\theta_{10} + \theta_{20} + \theta_{30}),$

$\mathbf{K}_{12} = -(m_2 l_2 + m_3 L_2) g sin(\theta_{10} + \theta_{20}) - m_3 g l_3 sin(\theta_{10} + \theta_{20} + \theta_{30}),$

$\mathbf{K}_{13} = -m_3 g l_3 sin(\theta_{10} + \theta_{20} + \theta_{30}),$

$\mathbf{K}_{21} = \mathbf{K}_{12},$

$\mathbf{K}_{22} = k_2 - (m_2 l_2 + m_3 L_2) g sin(\theta_{10} + \theta_{20}) - m_3 g l_3 sin(\theta_{10} + \theta_{20} + \theta_{30}),$

$\mathbf{K}_{23} = -m_3 g l_3 sin(\theta_{10} + \theta_{20} + \theta_{30}),$

$\mathbf{K}_{31} = \mathbf{K}_{13},$

$\mathbf{K}_{32} = \mathbf{K}_{23},$

$\mathbf{K}_{33} = k_3 - m_3 g l_3 sin(\theta_{10} + \theta_{20} + \theta_{30}),$

$\mathbf{E}_1 = (m_1 l_1 + m_2 L_1 + m_3 L_1) sin\theta_{10} + (m_2 l_2 + m_3 L_2) sin(\theta_{10} + \theta_{20}) + m_3 l_3 sin(\theta_{10} + \theta_{20} + \theta_{30}),$

$\mathbf{E}_2 = (m_2 l_2 + m_3 L_2) sin(\theta_{10} + \theta_{20}) + m_3 l_3 sin(\theta_{10} + \theta_{20} + \theta_{30}),$

$\mathbf{E}_3 = m_3 l_3 sin(\theta_{10} + \theta_{20} + \theta_{30}),$

Set $x_1 = \Delta\theta_1$, $x_2 = \Delta\theta_2$, $x_3 = \Delta\theta_3$, $x_4 = \Delta\dot{\theta}_1$, $x_5 = \Delta\dot{\theta}_2$, and $x_6 = \Delta\dot{\theta}_3$, the differential equations 4.7 is transferred to the state-space equation.

$$\begin{aligned} \dot{\mathbf{x}} &= \mathbf{A}\mathbf{x} + \mathbf{B_1}\mathbf{u} + \mathbf{B_2}\ddot{x}_0 \\ \mathbf{y} &= \mathbf{C}\mathbf{x} \end{aligned} \tag{4.8}$$

where

$$\mathbf{x} = \begin{pmatrix} x_1 \\ x_2 \\ x_3 \\ x_4 \\ x_5 \\ x_6 \end{pmatrix} = \begin{pmatrix} \Delta\theta_1 \\ \Delta\theta_2 \\ \Delta\theta_3 \\ \Delta\dot{\theta}_1 \\ \Delta\dot{\theta}_2 \\ \Delta\dot{\theta}_3 \end{pmatrix}, \mathbf{y} = \begin{pmatrix} \Delta\theta_1 \\ \Delta\theta_2 \\ \Delta\theta_3 \end{pmatrix}, \mathbf{u} = \begin{pmatrix} \Delta\tau_1 \\ \Delta\tau_2 \\ \Delta\tau_3 \end{pmatrix},$$

$$\mathbf{A} = \begin{pmatrix} \mathbf{0} & \mathbf{I} \\ \mathbf{M}^{-1}\mathbf{K} & \mathbf{M}^{-1}\mathbf{C} \end{pmatrix}, \mathbf{B_1} = \begin{pmatrix} \mathbf{0} \\ -\mathbf{M}^{-1} \end{pmatrix}, \mathbf{B_2} = \begin{pmatrix} \mathbf{0} \\ -\mathbf{M}^{-1}\mathbf{E} \end{pmatrix},$$

$$\mathbf{C} = \begin{pmatrix} 1 & 0 & 0 & 0 & 0 & 0 \\ 0 & 1 & 0 & 0 & 0 & 0 \\ 0 & 0 & 1 & 0 & 0 & 0 \end{pmatrix},$$

$\mathbf{0}$ is zero vectors or matrix, and $\mathbf{I}$ is a 3×3 identify matrix. The superscript -1 denotes the inverse of the matrices.

As with the one-link and two-link models, the active joint torque databases were built based on the vibration signals of magnitude 1 and magnitude 3. A vibration signal with magnitude 2 was used to test the capability of the system to predict the motion under unknown vibration signals with different magnitudes.

As shown in Figure 4.20, the displacement of the first link at x_1 showed characteristics very close to that of the experimental data. The displacement at the end of the second link at x_2 showed a trend similar to that of the experimental displacement

with relatively good agreement. The displacement at the end-effector of the third link at x_3 showed a trend similar to that of the experimental displacement but not as good as the situation with x_1 and x_2.

The acceleration and the power spectral density of the points at the end of link 1 and link 2 showed good correlation with the experimental data but relatively less correlation at the end-effector of link 3 (Figure 4.21 and 4.22).

4.8 Discussion

The current international standards ISO 2631-5 (2004) assume the dynamic response of the body as linear in the x and y directions; however, the literatures and the current study have demonstrated that this is clearly not the case. Then, if it is assumed that the potential for injury is related to the biomechanics of the body, the nonlinearities should be included in predictive models of the spine and the cervical spine for injury risk determination as the nonlinearities occur at frequencies that have been linked with spinal injury. The nonlinearity in the biodynamic response of the spine and the cervical spine also has implications on the design of vibration-suppression systems, especially those in off-road vehicle seats. Therefore, future development of models designed to predict the severity of vibration environments should ensure that nonlinear elements are adequately represented.

While the literatures attributed to the cause of nonlinearity on the soft-tissue to the ischial tuberosity and/or the bending-buckling characteristics of the spine region of the human body [14], this explanation may be applied to the spinal area but

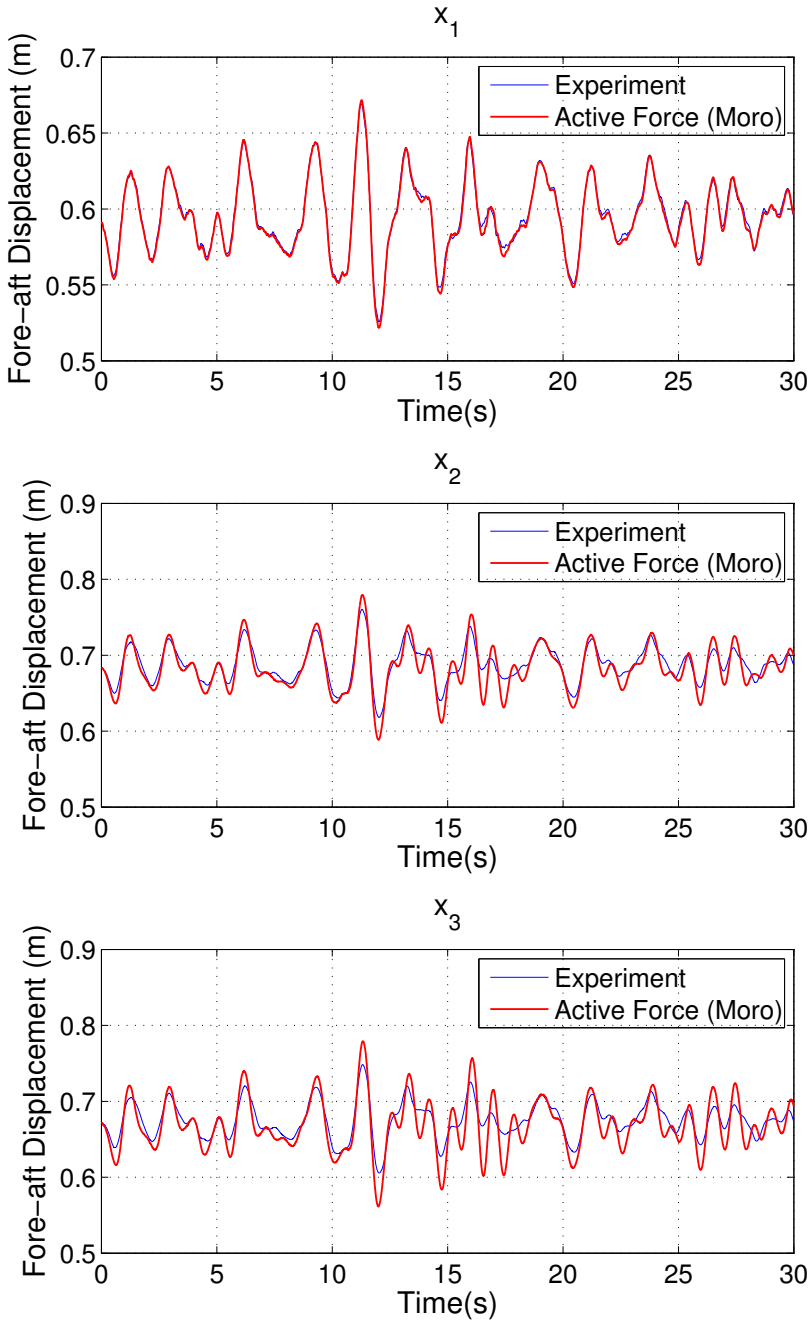

Figure 4.20: Fore-aft Mean displacement of x_1, x_2, and x_3 of the experimental and three-link model under vibration signal of magnitude 2

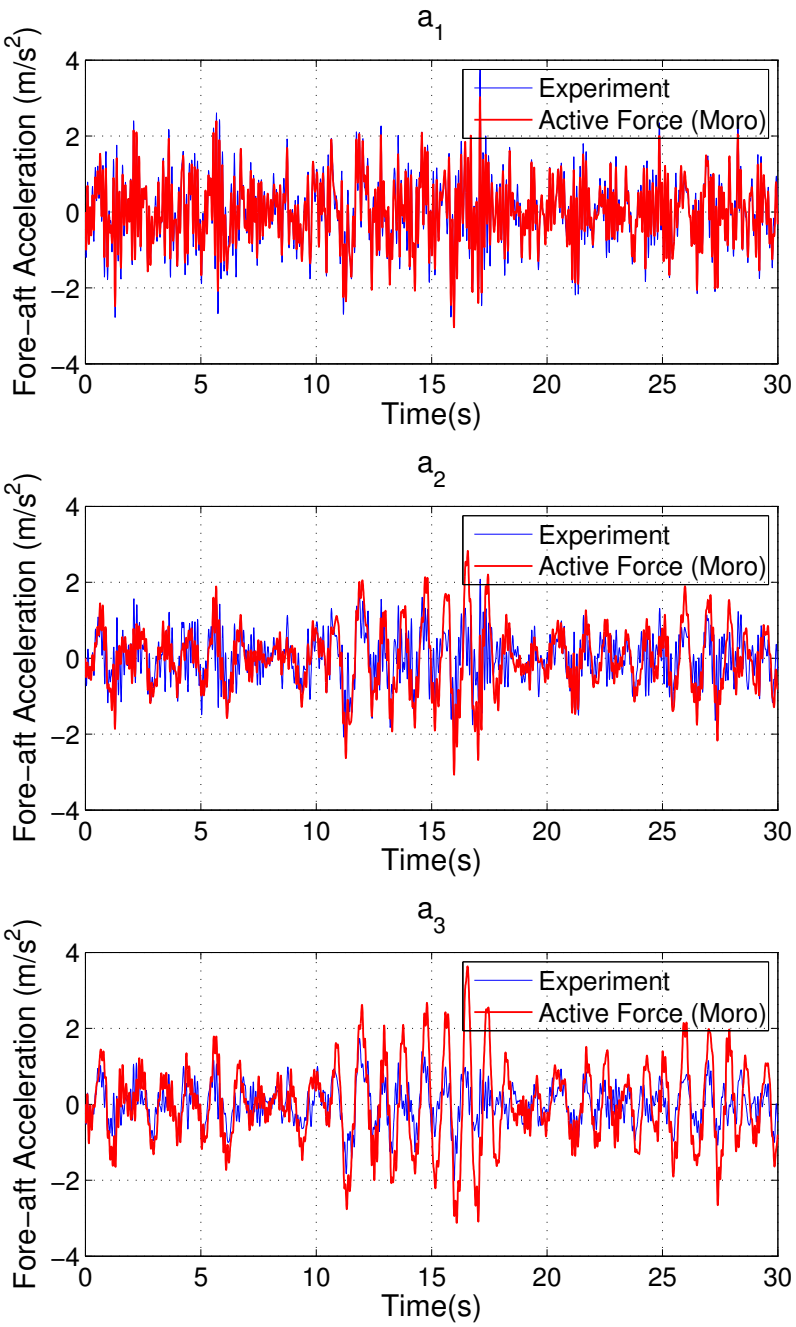

Figure 4.21: Fore-aft Mean acceleration of a_1, a_2, and a_3 of the experimental and three-link model under vibration signal of magnitude 2

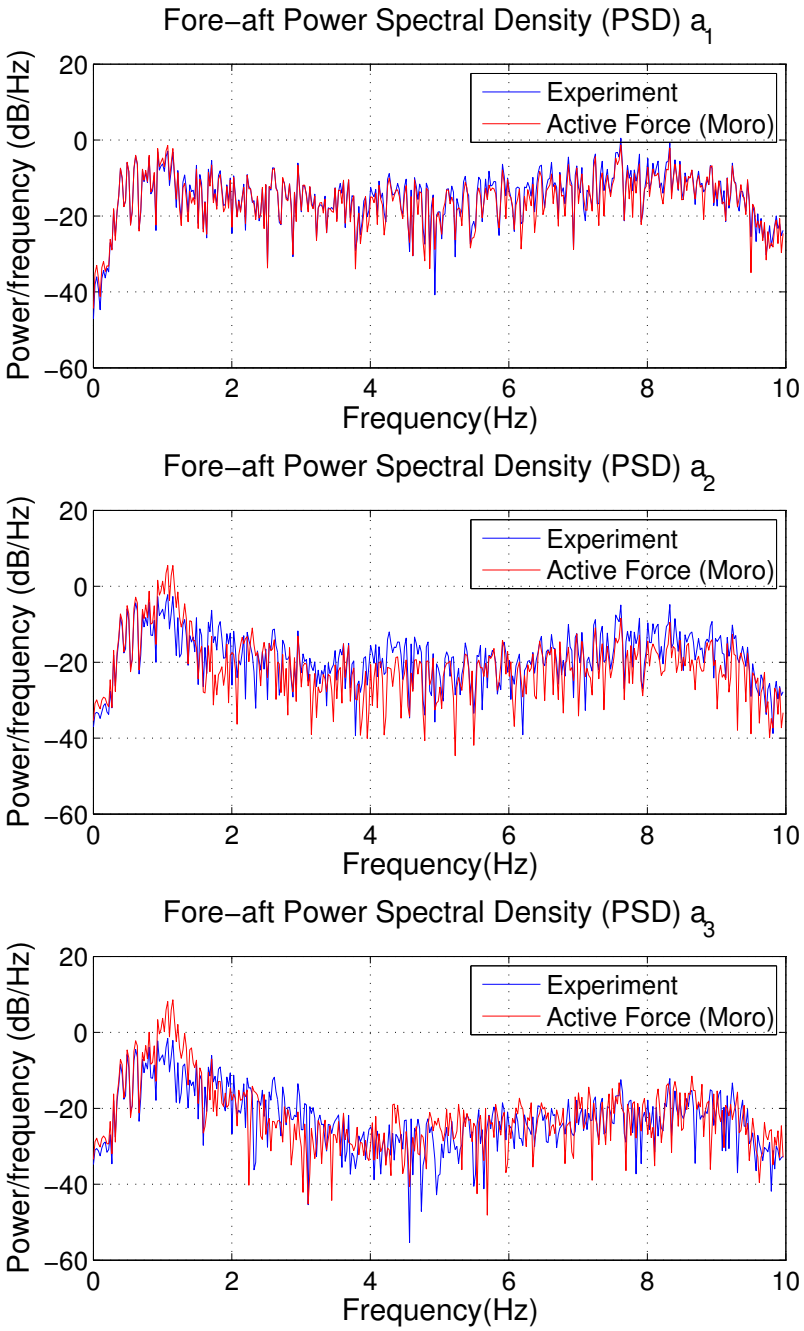

Figure 4.22: Fore-aft Mean power spectrum density of a_1, a_2, and a_3 of the experimental and three-link model under vibration signal of magnitude 2

would not be adequate for the head-neck region. The head-neck model was built based on the input data on C7 and output data on the head and therefore should not be affected by motion at the seat level. Thus, there could be something else causing the softening of the head-neck region that could be related to the muscle relaxation; this could be a question for further investigation in future studies.

The results showed that the proposed active head-neck models were very effective in reproducing the experimental data for different magnitudes as shown in Figure 4.13. Additionally, they reasonably predict the displacements and accelerations of the end-effector under vibration files with frequencies and magnitudes that were not considered in building the database. Nevertheless, the models demonstrate some errors depending on the complexity of the motion and the number of links used in constructing the models.

The source of error in the predicted motion at the end-effector could be linked to the sampling rates of the collected data and the resolution of the database. One way to build a database with more entities is to collect data at high sampling rates with vibration files that cover wide magnitudes and frequency spectrum.

The joint torque is obtained from the database at certain conditions by searching the database using the kd-tree search algorithm. If the kd-tree fails to find a joint torque value at the expected location, then it will use the nearest joint torque value and applied that to the system. Of course, that would generate some error in the magnitude of the applied torque on the system. Now if the difference between the nearest torque and the exact torque is relatively large, which could happen when the

database has coarse resolution, then that would create a relatively large error in the predicted motion.

The error in the predicting motion would increase as the number of links increases due to the accumulated error in calculating the displacement. For example, the displacement of the second link (x_2) will be affected by the error at θ_1 + the error at θ_2 and so forth. This would explain why the one-link model showed very good results when compared to the two-link and three-link systems. The two-link model showed good results for x_1 but fairly results for x_2. Similarly, the three-link model showed good results for x_1, moderate results for x_2, but less accurate results for x_3.

Because the acceleration magnitudes are derived from the displacement using the finite difference method, then it is expected to see larger artificial error due to this process as shown in Figure 4.11; of course that would be magnifies in the transmissibility results as shown in Figure 4.14.

Current head-neck model for WBV are designed to predict the displacement or acceleration of the end-effector with some accuracy, but they still have difficulties predicting the motion of the intermediate joints of the human body. This imposes restriction on the benefit of these models for medical applications where it is necessary to study the motion at a certain joint of the human neck for investigating musculoskeletal pathologies, for example. The proposed head-neck model will provide a good solution to these situations where it is possible to build the model with several links and possibly more links for more detailed models in the future. Simple forms of the model, like the one-link model, would be very useful and effective in ergonomic

studies to investigate the injury risk and discomfort of the head-neck region and for the development of better seats.

The comparison between the predictive capability of the proposed active head-neck model and a passive head-neck model that represents the current state-of-the-art have shown considerable advantages for the active model in terms of matching the magnitude and the frequency content of the experimental data.

4.9 Future Work

- Extend the multiple-link head-neck model to include the spine. This would help in investigating the motion of the lower back and help in building effective seats.
- More subjects will be tested to minimize the effect of intersubject variability.
- Collect data with higher sampling rates and a wider range of frequency and magnitudes. This would help in building databases with high resolution.

APPENDIX

University of Iowa IRB Approval Form

Human Subjects Office/
Institutional Review Board (IRB)
105 Hardin Library for the Health Sciences
600 Newton Road
Iowa City, Iowa 52242-1098
319-335-6564 *Fax* 319-335-7310
irb@uiowa.edu
http://research.uiowa.edu/hso

IRB ID #: 200811705

To: Salam Rahmatalla

From: IRB-02 Univ of Iowa, DHHS Registration # IRB00000100, DHHS Federalwide Assurance # FWA00003007

Re: Comfort Weighting Curve for Seated Machine Operators

Approval Date: 06/24/11

Next IRB Approval Due Before: 09/18/11

Type of Application:	**Type of Application Review:**	**Approved for Populations:**
☐ New Project	☐ Full Board:	☐ Children
☐ Continuing Review	Meeting Date:	☐ Prisoners
☒ Modification	☒ Expedited	☐ Pregnant Women, Fetuses, Neonates
	☐ Exempt	

Source of Support:

This approval has been electronically signed by IRB Chair:
Janet Karen Williams, PHD
06/24/11 1443

OFFICE OF THE VICE PRESIDENT FOR RESEARCH

University of Iowa IRB Consent Document

INFORMED CONSENT DOCUMENT

Project Title: Comfort Weighting Curve for Seated Machine Operators

Principal Investigator: Salam Rahmatalla

Research Team Contact: Salam Rahmatalla, 1 319 335-5614

John Meusch
Jonathan DeShaw

This consent form describes the research study to help you decide if you want to participate. This form provides important information about what you will be asked to do during the study, about the risks and benefits of the study, and about your rights as a research subject.

- If you have any questions about or do not understand something in this form, you should ask the research team for more information.
- You should discuss your participation with anyone you choose such as family or friends.
- Do not agree to participate in this study unless the research team has answered your questions and you decide that you want to be part of this study.

WHAT IS THE PURPOSE OF THIS STUDY?

This is a research study. We are inviting you to participate in this research study because you are a healthy, adult who does not have a history of muscle or bone disease or injury.

The purpose of this research study is to determine a proper shape of the comfort weighting curve for seated machine operators. This comfort curve will serve seat manufacturer in understanding the impact of machine changes on human comfort in single and multiple directions and therefore, help them in designing better and safer seats.
The study may also investigate the motion of people in supine position during emergency transportation with the goal of achieving better litter designs.

HOW MANY PEOPLE WILL PARTICIPATE?

Approximately 50 people will take part in this study at the University of Iowa.

HOW LONG WILL I BE IN THIS STUDY?

If you agree to take part in this study, your involvement will last for 3-6 hours in a single visit with no follow-up. If there are technical problems, you may be scheduled for second visit to complete the study procedures.

WHAT WILL HAPPEN DURING THIS STUDY?

If you agree to participate, you will be scheduled to return to the Engineering Research Facility, 330 South Madison Street, Iowa City, Iowa the morning of the test day. Inside the facility, you will change in to shorts and a tank-top so that the motion measurements can be obtained. The clothing will be supplied to you at the test site.

Preparation and Set-Up

Marker placement and calibration: Your body motion will be monitored using infrared cameras (VICON). Up to 90 reflective markers will be attached to your body. Each marker is about a half inch sphere attached to a soft rubber base of about 1 ½ inch x 1 ½ inch. The rubber base will be attached to your body using non-allergenic, double-sided tape. The markers on your head will be attached to an adjustable head band which you will wear on your head. Markers will be attached to your skin over bony landmarks, such as the elbow, the knee, the collar bone, or back bone. If you have considerable body hair, we will shave the small area of skin under each marker to minimize pain with removal of the markers. Markers may also be attached using athletic pre-wrap instead of adhesive tape. In some parts of the experiment, you may be dressed in a motion capture suit (a black cloth suit to which markers will be attached); in this case, the markers will be directly stuck to the suit instead of your skin.

Inertial sensors: Inertial sensors are devices that can measure acceleration in three and six directions. Inertial sensors are small devices that can sense movement. Inertial sensors will also be attached to your body at the same time the above markers are attached. Inertial sensors will be placed on you on up to 8 locations. The Inertial sensors will be attached to your skin using medical-grade, double-sided adhesive tapes, after cleaning your skin with rubbing alcohol.

The placement of the markers and inertial sensors will take about one to two hours.

In addition to the recordings for motion tracking, we will videotape the study procedure.

Testing

After this preparation stage, you will be instructed to sit on a chair or lay on a litter similar to those used in patient's transportation that is attached to a table that vibrates, called a shaker table. During the experiments, you will experience the physical conditions of a heavy construction machinery operator who is performing tasks in the real world or a person on a litter in an emergency transport vehicle.

Motion Capture Calibration: The first step in the motion capture process is to calibrate the system and ensure that the cameras see only the reflected markers (no artifact). The second step involves calibrating you by having you stand still for 30 seconds. The motion capture system will use this information to obtain your measurements, such as the length of your legs and arms.

Task Simulation: In order for you to keep your attention focused, we may provide a task for you to work on. The task consists of a video-game like simulation of the operation of a piece of heavy equipment. You will control the piece of equipment using the arm-rest controls you will be holding during the testing.

Experimental Protocol:
You will be tested under one of the following conditions:

Condition A) You will be asked to sit in the shaker table chair. The experiments to be conducted will include using a shaker table to provide vibration typical of operation of common heavy equipment.

You may be tested under the following scenarios:

1. Back on seatback and hands on armrests
2. Back on seatback and hands on lap
3. Back on seatback and hands on steering wheel
4. Back off seatback and hands on lap, and looking back (twisted posture)
5. Back off seatback and hands on armrests, and looking back (twisted posture)
6. Back off seatback and hands on lap
7. Back off seatback and hands on steering wheel
8. Back off seatback and hands on armrests
9. In some of the above cases, you may be asked to sit on a seat with your trunk constrain to the seatback using a life-Vest jacket; however, your arms will be freely to move. The reason for these cases is to isolate your head-neck motion from your trunk motion. By doing this, we will be able to more accurately analyzing the contribution of your head-motion to your discomfort level.

In all above cases, your feet will remain on the ground/pedals.

Condition B) You will be asked to take a supine position on a litter with a backboard similar to those in patient's transportation.
The following procedure will be used as recommended by the Local EMS provider (Johnson County):

1. Apply an appropriate, effective and properly fitted/sized cervical collar.
2. Position participant on the long spine board and center.
3. Place straps in an x-pattern over the shoulders and under the armpits to secure the upper chest.
4. Additional straps are placed across the iliac crest and above the knees to prevent movement.
5. Normal Anatomical Alignment of the spine should be maintained.
6. Immobilize the head in the normal anatomical position. 1-1.5 inches of non-compressive occipital padding may be used.
7. Towel rolls or other bulky, lightweight material may be placed around the head to stabilize.
8. Place a wide strip of adhesive tape across the forehead to form an “X” securing the head.
9. Secure the feet with tape to prevent leg motion.

The following cases will be considered:

i. Using traditional backboard.
ii. Using traditional backboard with cushions.

We will conduct a series of tests to collect information about your body’s responses to the movement of the shaker table seat and to test whether or not we are tracking the markers attached to you. You will experience up to 200 bouts of typical ride vibration on the shaker table each lasting up to 60 seconds

with total of up to 100 minutes. The test will be repeated for each of the above twoconditions.. The "rides" will consist of vibration in one or multiple directions. Normally, up to 100 minutes (for each of the two above mentioned conditions) of that time will consist of exposure to typical "ride" vibration. If up to half of the tests need to be repeated, you could be exposed to up to 150 minutes of "ride" vibration.

In the event a test is stopped before all the data are collected or data are lost due to computer failure, the test will be repeated, up to a maximum of half of the possible tests. It is unlikely that more than one or two tests will actually require repetition, but all estimates of total daily vibration and shock exposure have included these additional tests. In the event data recording systems fail to acquire data during a test, the test will be repeated. This may take an additional six hours during a separate visit.

As mentioned above, it is possible that some tests may need to be further repeated in the event results are not stored properly (data lost due to computer error, etc.). The duration of the testing procedures should require no longer than 6 hours (with breaks). The expected total duration of exposure to the vibration is 100 minutes, but could be as high as 150 minutes in the event half of the tests require repeating.

During the tests, you will be asked by the investigators to rate your discomfort level either using verbal forms or paper based forms.

You may be asked to complete more visits if additional testing is required.

Audio/Video Recording or Photographs

One aspect of this study involves taking some pictures and video movies during the testing procedures. The motion capture cameras can only "see" infrared light reflected from markers. In addition to the motion capture camera images, we will take photographs and video of you using traditional still and video cameras to know where the markers are located on your body. The pictures and video movies will help us in identifying the location of the markers on the body during the experiments; otherwise, it would be very difficult to recognize the real markers' locations on the body by just looking to the motion capture data. In the event these materials are used in reports or publications, the images will be altered so that no personally-identifiable information will appear.

These recordings and photographs will be used to document the test protocol. These recordings will not be erased or destroyed as they will provide valuable documentation of the study.

WHAT ARE THE RISKS OF THIS STUDY?

You may experience one or more of the risks indicated below from being in this study. In addition to these, there may be other unknown risks, or risks that we did not anticipate, associated with being in this study.

You may feel some irritation from the preparation for, the use of, and the removal of the reflective markers, and accelerometers. We will try to minimize this risk by using only medical-grade tape meant for use on human skin and shaving any areas that have substantial hair. We will try to make the time that the devices are attached as short as possible consistent with the data to be gathered. We will monitor you carefully by sight and by asking questions about how you feel. We will ask you if you are allergic to adhesive tape before placing the markers and accelerometers on your skin.

You may be at risk for developing dizziness. You will have a switch that will immediately stop the ride in the event you feel you need to stop. You can also take breaks as needed throughout the test protocol. We will monitor you carefully by sight and by asking questions about how you feel. If you are prone to motion sickness, have a history of vestibular (inner ear) problems, or do not tolerate simulation rides at Amusement Parks, you should not enroll in this study.

The vibration involved in this study may pose a risk for muscle or back pain with extended exposures. However, one day of testing is unlikely to result in any chronic vibration or shock injuries. The front to back vibrations you will experience should be no worse than those felt while riding a tractor on a rough field or operating typical heavy construction equipment for a period of time. We have analyzed the vibration for the conditions you will experience using international standards to be sure that the total exposure is within acceptable levels. If you have a history of neck or back pain, you should tell the researchers before enrolling in the study.

There is a risk that you could faint during the test. Sitting for extended periods of time, coupled with the simulated ride, could result in feeling like you could faint. Before fainting, people have reported experiencing weakness, lightheadedness, nausea, sweating, hyperventilation, blurred vision and/or impaired hearing. Sitting or lying down can reverse the symptoms. To minimize the risk of fainting, regular rest intervals are planned, where you will be asked to get up out of the seat and stand and move your arms and legs. Further you will be monitored closely for any signs of intolerance listed above, by sight and by asking questions about how you feel throughout the test. If you have any history of fainting or have a cardiac condition you should not enroll in this study.

If you have a history of neck or back pain, heart problems, neurological problems, balance problems or dizziness, motion sickness, or are taking over-the-counter drugs, prescribed drugs, or have consumed alcohol or recreational drugs within 24 hours of the study, you should not enroll in this study.

There is a risk that you may experience a fear of falling or being unable to maintain your balance in the seat. We will minimize this situation by monitoring you carefully by sight and by asking questions about how you feel. If you have any history of fear, then you should not enroll in this study.

WHAT ARE THE BENEFITS OF THIS STUDY?

You will not benefit from being in this study. However, we hope that, in the future, other people might benefit from this study because the result of this study may help seat and machine designers to develop more comfortable seats for heavy machinery operators.

WILL IT COST ME ANYTHING TO BE IN THIS STUDY?

You will not have any cost for being in this research study.

WILL I BE PAID FOR PARTICIPATING?

You will be paid for being in this research study. You will need to provide your social security number (SSN) in order for us to pay you. You may choose to participate without being paid if you do not wish to provide your social security number (SSN) for this purpose. You may also need to provide your address if a check will be mailed to you. If your social security number is obtained for payment purposes only, it will not be retained for research purposes.
You will be paid at a rate of $12 per hour of a total of up to $72. The average amount per visit is $48.

DO THE RESEARCHERS HAVE PERSONAL FINANCIAL INTEREST IN THIS STUDY?

No.

WHO IS FUNDING THIS STUDY?
Departmental Funding from the University of Iowa, Center for computer aided design.

WHAT IF I AM INJURED AS A RESULT OF THIS STUDY?

- If you are injured or become ill from taking part in this study, medical treatment is available at the University of Iowa Hospitals and Clinics.
- No compensation for treatment of research-related illness or injury is available from the University of Iowa unless it is proven to be the direct result of negligence by a University employee.
- If you experience a research-related illness or injury, you and/or your medical or hospital insurance carrier will be responsible for the cost of treatment.

WHAT ABOUT CONFIDENTIALITY?

We will keep your participation in this research study confidential to the extent permitted by law. However, it is possible that other people such as those indicated below may become aware of your participation in this study and may inspect and copy records pertaining to this research. Some of these records could contain information that personally identifies you.

- federal government regulatory agencies,
- auditing departments of the University of Iowa, and
- the University of Iowa Institutional Review Board (a committee that reviews and approves research studies)

To help protect your confidentiality, we will assign you an identification number that does not include any personally identifiable information. All data will be stored on password-protected computer files using this number and not your name. Your name and personal information will be linked to your study identification number in a separate document and kept by the principal investigator in electronic and hard-copy formats separately from the rest of the data. All data will be kept in a locked lab or office or in password protected computer files, with appropriate backup. The motion data will be available to other researchers for future model development; however no personal identification of any kind will be linked to the data sets.

If we write a report or article about this study or share the study data set with others, we will do so in such a way that you cannot be directly identified.

IS BEING IN THIS STUDY VOLUNTARY?

Taking part in this research study is completely voluntary. You may choose not to take part at all. If you decide to be in this study, you may stop participating at any time. If you decide not to be in this study, or if you stop participating at any time, you won't be penalized or lose any benefits for which you otherwise qualify.

Will I Receive New Information About the Study while Participating?
If we obtain any new information during this study that might affect your willingness to continue participating in the study, we'll promptly provide you with that information.

Can Someone Else End my Participation in this Study?
Under certain circumstances, the researchers might decide to end your participation in this research study earlier than planned. This might happen because in our judgment it would not be safe for you to continue or because the funding for the research study has ended.

WHAT IF I HAVE QUESTIONS?

We encourage you to ask questions. If you have any questions about the research study itself, please contact: Salam Rahmatalla at (319) 335-5614 or salam-rahmatalla@uiowa.edu. If you experience a research-related injury, please contact Salam Rahmatalla at (319) 335-5614 or salam-rahmatalla@uiowa.edu. If you have questions, concerns, or complaints about your rights as a research subject or about research related injury, please contact the Human Subjects Office, 105 Hardin Library for the Health Sciences, 600 Newton Road, University of Iowa, Iowa City, IA 52242-1098, (319) 335-6564, or e-mail irb@uiowa.edu. General information about being a research subject can be found by clicking "Info for Public" on the Human Subjects Office web site, http://research.uiowa.edu/hso. To offer input about your experiences as a research subject or to speak to someone other than the research staff, call the Human Subjects Office at the number above.

This Informed Consent Document is not a contract. It is a written explanation of what will happen during the study if you decide to participate. You are not waiving any legal rights by signing this Informed Consent Document. Your signature indicates that this research study has been explained to you, that your questions have been answered, and that you agree to take part in this study. You will receive a copy of this form.

Subject's Name (printed): _____

Do not sign this form if today's date is on or after EXPIRATION DATE: 09/18/11 .

_____ _____
(Signature of Subject) (Date)

Statement of Person Who Obtained Consent

I have discussed the above points with the subject or, where appropriate, with the subject's legally authorized representative. It is my opinion that the subject understands the risks, benefits, and procedures involved with participation in this research study.

_____ _____
(Signature of Person who Obtained Consent) (Date)

REFERENCES

[1] D. Hrovat. Survey of advanced suspension developments and related optimal control applications. *Automatica*, 33(10):1781–1817, 1997.

[2] Z. Q. Lang, X. J. Jing, S. A. Billings, G. R. Tomlinson, and Z. K. Peng. Theoretical study of the effects of nonlinear viscous damping on vibration isolation of sdof systems. *Journal of Sound and Vibration*, 323(1-2):352–365, 2009.

[3] S. B. Choi, J. H. Choi, Y. S. Lee, and M. S. Han. Vibration control of an ER seat suspension for a commercial vehicle. *Journal of Dynamic Systems Measurement and Control-Transactions of the Asme*, 125(1):60–68, 2003.

[4] D. Karnopp. Active and semiactive vibration isolation. *Journal of Mechanical Design*, 117:177–185, 1995.

[5] Singiresu S. Rao. *Mechanical Vibrations*. Pearson Prenrice Hall, New Jersey, fourth edition, 2004.

[6] J. P. Den Hartog. *Mechanical Vibrations*. McGraw-Hill Book Company, New York, fourth edition, 1956.

[7] T.C. Jordan and M.T. Shaw. Electrorheology. *Electrical Insulation, IEEE Transactions on*, 24(5):849–878, 1989.

[8] BF Spencer, SJ Dyke, MK Sain, and JD Carlson. Phenomenological model for magnetorheological dampers. *Journal of Engineering Mechanics-asce*, 123(3):230–238, 1997.

[9] C. M. A. Vasques and J. Dias Rodrigues. Active vibration control of a smart beam through piezoelectric actuation and laser vibrometer sensing: simulation, design and experimental implementation. *Smart Materials and Structures*, 16(2):305–316, 2007.

[10] D. G. Wilder, B. B. Woodworth, J. W. Frymoyer, and M. H. Pope. Vibration and the human spine. *Spine*, 7(3):243–254, 1982.

[11] E. Johanning, D. G. Wilder, P. J. Landrigan, and M. H. Pope. Whole-body vibration exposure in subway cars and review of adverse health-effects. *Journal of Occupational and Environmental Medicine*, 33(5):605–612, 1991.

[12] D. G. Wilder. The biomechanics of vibration and low-back-pain. *American Journal of Industrial Medicine*, 23(4):577–588, 1993.

[13] M. H. Pope, M. Magnusson, and D. G. Wilder. Low back pain and whole body vibration. *Clinical Orthopaedics and Related Research*, 354:241–248, 1998.

[14] Neil J. Mansfield and Michael J. Griffin. Non-linearities in apparent mass and transmissibility during exposure to whole-body vertical vibration. *Journal of Biomechanics*, 33(8):933–941, 2000.

[15] S. Rakheja, R. G. Dong, S. Patra, P. E. Boileau, P. Marcotte, and C. Warren. Biodynamics of the human body under whole-body vibration: Synthesis of the reported data. *International Journal of Industrial Ergonomics*, 40(6):710–732, 2010.

[16] S. D. Smith, J. A. Smith, and D. R. Bowden. Transmission characteristics of suspension seats in multi-axis vibration environments. *International Journal of Industrial Ergonomics*, 38(5-6):434–446, 2008.

[17] B. Hinz, R. Bluthner, G. Menzel, S. Rutzel, H. Seidel, and H. P. Wolfel. Apparent mass of seated men - determination with single- and multi-axis excitations at different magnitudes. *Journal of Sound and Vibration*, 298(3):788–809, 2006.

[18] M. J. Griffin, C. H. Lewis, K. C. Parsons, and E. M. Whitham. Biodynamic response of the human-body and its application to standards. *Journal of Sound and Vibration*, 67(4):583–583, 1979.

[19] W. P. Wang, B. Bazrgari, A. Shirazi-Adl, S. Rakheja, and P. E. Boileau. Biodynamic response and spinal load estimation of seated body in vibration using finite element modeling. *Industrial Health*, 48(5):557–564, 2010.

[20] C Rekik, M Djemel, and N Derbel. A discussion on the optimal control of a robot manipulator by a hybrid genetic-fuzzy controller. *International Journal of Robotics & Automation*, 23(3):150–150–159, 2008.

[21] Stefan Fenik and Ladislav Starek. Optimal PI controller with position feedback for vibration suppression. *Journal of Vibration and Control*, 16(13):2023–2034, 2010.

[22] Wen Li and Yoichi Hori. Vibration suppression using single neuron-based PI fuzzy controller and fractional-order disturbance observer. *IEEE Transactions On Industrial Electronics*, 54(1):117–126, 2007.

[23] Ning Wang and Jian Tu. Self-adaptive neural network intelligent control. *Infomation and Control*, 21(4):235–239, 1992.

[24] Yongji Wang, Jie Chen, Guiying Xu, and Jian Tu. The adaptive neural control of hydraulic turbine set speed regulating system. *Acta Automatica Sinica*, 20(1):117–120, 1994.

[25] Yongji Wang, M. Schinkel, Tilmann Schmitt-Hartmann, and Ken J. Hunt. PID and PID-Like controller design by pole assignment within d-stable regions. *Asian Journal of Control*, 4(4):423–432, 2002.

[26] F. M. L. Amirouche. Modeling of human reactions to whole-body vibration. *Journal of Biomechanical Engineering-transactions of the Asme*, 109(3):210–217, 1987.

[27] M. Fritz. Three-dimensional biomechanical model for simulating the response of the human body to vibration stress. *Medical & Biological Engineering & Computing*, 36(6):686–692, 1998.

[28] Steffen Pankoke, Jrg Hofmann, and Horst P. Wlfel. Determination of vibration-related spinal loads by numerical simulation. *Clinical Biomechanics*, 16(Supplement 1):S45–S56, 2001.

[29] F. E. Zajac. Muscle coordination of movement - a perspective. *Journal of Biomechanics*, 26:109–124, 1993.

[30] S Bennett. A brief history of automatic control. *IEEE Control Systems Magazine*, 16(3):17–25, 1996.

[31] Nicolas Minorsky. Directional stability of automatically steered bodies. *Journal of the American Society of Naval Engineers*, 34(2):280–309, 1922.

[32] Katsuhiko Ogata. *Modern Control Engineering*. Prentice Hall, New Jersey, fifth edition, 2009.

[33] Jeffrey B. Burl. *Linear optimal control: H_2 and H_∞ methods*. Addison Wesley Longman, Menlo Park, California, 1999.

[34] Frank L. Lewis. *Applied Optimal Control and Estimation: Digital Design and Implementation*. Prentice Hall, Englewood Cliffs, New Jersey, 1992.

[35] Donald Olding Hebb. *The Organization of Behavior: A Neuropsychological Theory*. John Wiley and Sons, New York, 1949.

[36] Philip E. Gill, Walter Murray, and Michael A. Saunders. *Users Guide for SNOPT Version 7: Software for Large-Scale Nonlinear Programming*, February 2006.

[37] Sunil Ayra and David M. Mount. *Computational Geometry: Proximity and Location*, pages 63–14–63–17. Chapman and Hall/CRC Press, San Jose, CA, 2005.

[38] http://www.mathworks.com/matlabcentral/fileexchange/7030-kd-tree-nearest-neighbor-and-range-search.

[39] http://www.vibrationdata.com/elcentro.htm.

[40] http://peer.berkeley.edu/smcat/index.html.

[41] K. A. Tahboub. Intelligent control for manipulators with moving bases. *Journal of Intelligent Manufacturing*, 9(1):1–7, 1998.

[42] TP Bucklaew and CS Liu. Pitchfork-type bifurcations in a parametrically excited, pd-controlled pendulum or manipulator. *Journal of Sound and Vibration*, 247(4):655–672, 2001.

[43] Q Wu, N Sepehri, P Sekhavat, and S Peles. On design of continuous lyapunov's feedback control. *Journal of The Franklin Institute-engineering and Applied Mathematics*, 342(6):702–723, 2005.

[44] Richard P. Paul. *Robot Manipulators: Mathematics, Programming, and Control*. MIT Press, 1981.

[45] Franks L. Lewis, Darren M. Dawson, and Chaouki T. Abdallah. *Robot Manipulator Control: Theory and Practice*. CRC Press, New York, second edition, 2003.

[46] T. Belytschko, L. Schwer, and A. Schultz. A model for analytic investigation of three-dimensional head-spine dynamics. Technical report, Illinois University At Chicago Circle Department Of Materials Engineering, 1976.

[47] E.K. Franke, H.E. von. Gieeke, H.L. Oestreicher, H.O. Parrack, and W.W. von. Wittern. Physics of vibrations in living tissues. Technical Report 6367, Aero Medical Laboratory, Wright-Patterson Air Force Base, Ohio, 1951.

[48] E.K. Franke, H.E. von. Gieeke, H.L. Oestreicher, and W.W. von. Wittern. The propagation of surface waves over the human body. Technical Report 6464, Aero Medical Laboratory, Wright-Patterson Air Force Base, Ohio, 1951.

[49] H. Seidel and M. J. Griffin. Modelling the response of the spinal system to whole-body vibration and repeated shock. *Clinical Biomechanics*, 16:S3–S7, 2001.

[50] Z. P. Luo and W. Goldsmith. Reaction of a human head neck torso system to shock. *Journal of Biomechanics*, 24(7):499–510, 1991.

[51] B. Hinz, G. Menzel, R. Bluthner, and H. Seidel. Seat-to-head transfer function of seated men -determination with single and three axis excitations at different magnitudes. *Industrial Health*, 48(5):565–583, 2010.

[52] S. D. Smith. Dynamic characteristics and human perception of vibration aboard a military propeller aircraft. *International Journal of Industrial Ergonomics*, 38(9-10):868–879, 2008.

[53] W. Qassem, M. O. Othman, and S. Abdulmajeed. The effects of vertical and horizontal vibrations on the human-body. *Medical Engineering & Physics*, 16(2):151–161, 1994.

[54] M. G. R. Toward and M. J. Griffin. A variable parameter single degree-of-freedom model for predicting the effects of sitting posture and vibration magnitude on the vertical apparent mass of the human body. *Industrial Health*, 48(5):654–662, 2010.

[55] J. L. Williams and T. B. Belytschko. A 3-dimensional model of the human cervical-spine for impact simulation. *Journal of Biomechanical Engineering-transactions of the Asme*, 105(4):321–331, 1983.

[56] T. Belytschko, L. Schwer, and E. Privitzer. Theory and application of a 3-dimensional model of human spine. *Aviation Space and Environmental Medicine*, 49(1):158–165, 1978.

[57] F.M.L. Amirouche and S.K. Ider. Simulation and analysis of a biodynamic human model subjected to low accelerations–a correlation study. *Journal of Sound and Vibration*, 123(2):281–292, 1988.

[58] S. B. Roberts, C. C. Ward, and A. M. Nahum. Head trauma - a parametric dynamic study. *Journal of Biomechanics*, 2:397–415, 1969.

[59] M. A. Fard, T. Ishihara, and H. Inooka. Dynamics of the head-neck complex in response to the trunk horizontal vibration: Modeling and identification. *Journal of Biomechanical Engineering-transactions of the Asme*, 125(4):533–539, Aug 2003.

[60] F. M. L. Amirouche, M. Xie, and A. Patwardhan. Optimization of the contact damping and stiffness coefficients to minimize human-body vibration. *Journal of Biomechanical Engineering-transactions of the Asme*, 116(4):413–420, 1994.

[61] W. Bajon and M. Nader. The analysis of locomotive drivers reaction on certain dynamic loads. In *CISM Italy*, Udine, Italy, 1986.

[62] R. R. Coermann, G. H. Ziegenruecker, A. L. Wittwer, and H. E. Von Gierke. The passive dynamic mechanical properties of the human thorax-abdomen system and of the whole body system. *Aerosp Med*, 31:443–55, 1960.

[63] Vongierk.He. Response of body to mechanical forces - an overview. *Annals of the New York Academy of Sciences*, 152:172–&, 1968.

[64] Ints Kaleps, von Gierke, Henning E., and E. B. Weis. A five-degree-of-freedom mathematical model of the body. Technical Report AMRL-TR-71-29-Paper-8, Aero Medical Laboratory, Wright-Patterson Air Force Base, Ohio, 1971.

[65] R. Muksian and C. D. Nash. Model for response of seated humans to sinusoidal displacements of seat. *Journal of Biomechanics*, 7(3):209–215, 1974.

[66] M. K. Patil, M. S. Palanichamy, and D. N. Ghista. Man-tractor system dynamics - towards a better suspension system for human ride comfort. *Journal of Biomechanics*, 11(8-9):397–406, 1978.

[67] R. Toth. Multiple degree-of-freedom nonlinear spinal model. In *Proceedings of the 19th Annual Conference on Engineering in Medicine and Biology*, page 102, San Fransisco, 1966.

[68] M. Dietrich, K. Kedzior, and T. Zagrajek. A biomechanical model of the human spinal system. *Proc Inst Mech Eng H*, 205(1):19–26, 1991.

[69] Dietrich M, Kedzior K, and Zagrajek T. Biomechanical modelling of human spine system, 1992. Lecture Notes of the ICB Seminars Biomechanics.

[70] S. Pankoke, B. Buck, and H. P. Woelfel. Dynamic FE model of sitting man adjustable to body height, body mass and posture used for calculating internal forces in the lumbar vertebral disks. *Journal of Sound and Vibration*, 215(4):827–839, 1998.

[71] MA Fard, T Ishihara, and H Inooka. Identification of the head-neck complex in response to trunk horizontal vibration. *Biological Cybernetics*, 90(6):418–426, 2004.

[72] Ya Huang and Michael J. Griffin. Nonlinearity in apparent mass and transmissibility of the supine human body during vertical whole-body vibration. *Journal of Sound and Vibration*, 324(1-2):429–452, 2009.

[73] C. D. Robertson and M. J. Griffin. Laboratory studies of the electromyographic response to whole-body vibration. Technical Report ISVR 184, University of Southampton, Southampton, UK, 1989.

[74] S. Rahmatalla and J. DeShaw. Predictive discomfort of non-neutral head-neck postures in fore-aft whole-body vibration. *Ergonomics*, 54(3):263–272, 2011.

[75] Augustus A. White and Manohar M. Panjabi. *Clinical Biomechanics of the spine*. Lippincott Williams & Wilkins, second edition, 1990.

[76] A. I. King. Fundamentals of impact biomechanics: Part i - biomechanics of the head, neck, and thorax. *Annual Review of Biomedical Engineering*, 2:55–81, 2000.

[77] Wilfrid Taylor Dempster and George R. L. Gaughran. Properties of body segments based on size and weight. *American Journal of Anatomy*, 120(1):33–54, 1967.

[78] Yk Liu, Jm Laborde, and Vanbuski.Wc. Inertial properties of a segmented cadaver trunk - their implications in acceleration injuries. *Aerospace Medicine*, 42(6):650–657, 1971.

[79] Sean P. Moroney, Albert B. Schultz, James A.A. Miller, and Gunnar B.J. Andersson. Load-displacement properties of lower cervical spine motion segments. *Journal of Biomechanics*, 21(9):769–779, 1988.